Università degli Studi di Firenze

Scuola di Ingegneria

DIEF - Department of Industrial Engineering of Florence

PhD School: *Energetica e Tecnologie Industrali ed Ambientali Innovative*

Scientific Area: ING-IND/08 - *Macchine a Fluido*

Numerical Investigation of Fluid-Dynamic Losses in Power Gearboxes For Aero-Engine Applications

PhD Candidate: Ing. Tommaso Fondelli

Tutor: Prof. Ing. Bruno Facchini

Academic Supervisor: Dr. Ing. Antonio Andreini

Industrial Supervisor: Dr. Ing. Daniele Coutandin

PhD School Coordinator: Prof. Ing. Maurizio De Lucia

XXVIII PhD School Cycle - 2012-2015

Università degli Studi di Firenze
Scuola di Ingegneria
DIEF - Department of Industrial Engineering of Florence

PhD School: *Energetica e Tecnologie Industrali ed Ambientali Innovative*
Scientific Area: ING-IND/08 - *Macchine a Fluido*

Numerical Investigation of Fluid-Dynamic Losses in Power Gearboxes For Aero-Engine Applications

PhD Candidate: Ing. Tommaso Fondelli

Tutor: Prof. Ing. Bruno Facchini

Academic Supervisor: Dr. Ing. Antonio Andreini

Industrial Supervisor: Dr. Ing. Daniele Coutandin

PhD School Coordinator: Prof. Ing. Maurizio De Lucia

XXVIII PhD School Cycle - 2012-2015

Dedicato a coloro che mi hanno sostenuto
e che hanno creduto in me.
Grazie di cuore.

Ringraziamenti

Giunto alla fine di questo percorso desidero ringraziare tutte le persone che mi sono state vicine e che ho avuto il piacere di conoscere in questi anni.

Innanzitutto desidero ringraziare il Prof. Bruno Facchini per avermi dato la possibilità di intraprendere questo percorso di crescita personale e professionale. Grazie per la cordialità e la grande disponibilità dimostrata. Un grazie altrettanto sentito all'Ing. Antonio Andreini, una guida in questi anni di dottorato, lo ringrazio per tutto ciò che mi ha trasmesso. Desidero poi ringraziare il Prof. Carlo Carcasci, i congressi passati insieme li ricordo con il sorriso. Un grazie doveroso agli Ergon-guys, in particolare all'Ing. Lorenzo Tarchi per avermi guidato e cosigliato nell'attività sperimentale condotta in questi anni.

Desidero inoltre ringraziare la società GE Avio S.r.l., in particolare gli Ingegneri Lorenzo Cipolla, Daniele Coutandin, Federico Leonardi e Stefano Zecchi che mi hanno seguito in questo lavoro, grazie per tutti i consigli e l'esperienza messa a disposizione.

Un grazie sincero a tutti i miei colleghi e compagni di avventura, è stato un piacere lavorare e crescere insieme, grazie per tutte le risate ed i momenti trascorsi insieme, li ricordo con estremo piacere.

Desidero ringraziare di cuore la mia famiglia per l'affetto e la fiducia

riposta in me, il vostro esempio vale più di mille parole, è ciò che porto sempre con me. Infine, un grazie speciale a Daniela per essermi accanto e per avermi supportato e sopportato durante la stesura di questo lavoro.

What we know is a drop,
what we don't know is an ocean.
Isaac Newton

Abstract

The Geared Turbofan (GTF) technology is one of the most promising engine configurations to sensibly reduce the specific fuel consumption (SFC) by increasing the engine bypass ratio. In this architecture, a power epicyclic gearbox is interposed between the fan and the low-pressure spool, resulting in advantages both at engine and component level.

The SFC is directly affected by the transmission efficiency of the gearbox and indirectly by the weight and the size of the cooling system. Therefore the gearbox performance becomes a key technology to achieve the benefits introduced by the GTF architecture. Although the transmission efficiency is usually higher than 99 %, power losses are important in high power application such as the one under consideration.

A performance enhancement can be achieved developing a physical understanding of the losses within the transmission system. These are classified into load-dependent and load-independent groups. The former are primarily related to a mechanical power loss due to friction at the gear contact, while the latter are related to fluid-dynamic effects. Whilst there has been a large body of work dealing with load-dependent power losses, and suitable models for the prediction are already available, the fluid-dynamic losses still need to be studied and properly modelled.

This research study is aimed at defining CFD methodologies to be used in the comprehension of fluid-dynamic losses in gearbox systems for aero-engine applications, to develop predictive tools to be used in industrial design process. A complete simulation of the multiphase flow within the epicyclic gear train would be too expensive and not useful in

the understanding of the various loss mechanisms, so that each one has to be studied individually. Therefore the power losses related to the windage phenomena and to the oil-jet lubrication method were investigated.

The windage losses of a spur gear in free and enclosed configuration have been analysed by means of RANS simulations, defining a reliable numerical setup. The results have been validated by comparison with experimental data. A greater insight into the phenomenon was achieved, which allowed to modify and improve a correlative approach available in literature for calculating the windage power loss, by introducing the effect of the fluid volume enclosed in the gearbox.

Concerning the losses due to the oil-jet lubrication, numerical studies were performed using the Volume of Fluid (VOF) method, within the context of transient RANS calculations. These simulations were aimed at improving the description of the complex physical phenomena characterizing the oil-jet lubrication in high speed gearing systems. However VOF approach requires a very fine mesh in the liquid region, leading to considerable computational efforts. In this respect, a strategy for automatic grid adaptation was developed, reducing heavily the numerical effort. VOF simulations were performed varying the oil injection angle and the injection velocity, to assess how these parameters affect the power losses as well as the lubrication performance. As main results, a simplified formulation for the prediction of the power losses due to the oil-jet lubrication has been developed, then an optimum configuration for such a system was defined. The presented VOF study is one of the first in literature which provides detailed insight on the physic of the oil-jet lubrication.

Finally, the methodologies developed in this work have been partially validated by comparisons with preliminary experimental measurements performed on the High-Speed Test Rig, set up at the University of Florence, which was designed with input from the present research work.

Contents

List of Figures

List of Tables

Nomenclature

CF	Coverage factor	$[-]$
C_m	Momentum coefficient	$[-]$
C_t	Windage power loss coefficient	$[-]$
C_v	Volume correction parameter	$[-]$
D	Diameter	$[m]$
F	Force	$[N]$
Fr	Froude number	$[-]$
H	Height	$[m]$
k	Turbulence kinetic energy	$[m^2\ s^{-2}]$
L	Length	$[-]$
M	Moment of a force	$[N\ m^{-1}]$
$\dot{m}$	Mass flow rate	$[kgs^{-1}]$
p	Pressure	$[Pa]$
P	Power	$[W]$
PF	Penetration factor	$[-]$
q	Liquid to gas momentum ratio	$[-]$
R	Radius	$[m]$
R^2	Coefficient of determination	$[m]$
Re_j	Jet Reynold number	$[-]$
$Re_{\dot{\phi}}$	Rotational Reynold number	$[-]$
T	Torque	$[N\ m]$
U	Mean Velocity	$[m\ s^{-1}]$
UR	Velocity coefficient	$[m\ s^{-1}]$
We_{cf}	Crossflow Weber number	$[-]$
We_j	Jet Weber number	$[-]$
X_A	Profile shift coefficient	$[-]$
x_b	Liquid column breakup distance	$[m]$
y_b	Liquid column breakup height	$[m]$

Z	Number of gear teeth	[−]

Acronyms

BPR	Bypass Ratio
CFD	Computational Fluid Dynamics
CLSVOF	Coupled Level Set and Volume of Fluid
DIEF	Department of Industrial Engineering of Florence
DNS	Direct Numerical Simulation
GTF	Geared Turbofan
HP	High Pressure
HPT	High Pressure Turbine
ID	Identification number
LAI	Liquid-Air Interface
LES	Large Eddy Simulation
LOR	Level of refinement
LP	Low Pressure
LPT	Low Pressure Turbine
LS	Level Set
NASA	National Aeronautics and Space Administration
NWR	Near wall region
PLIC	Piecewise Linear Interface Calculation
PS	Pressure Side
RANS	Reynolds Averaged Navier Stokes
RNG	Renormalization Group
SFC	Specific Fuel Consumption
SLIC	Simple Line Interface Calculation
SS	Suction Side
SST	Shear Stress Transport
URANS	Unsteady Reynolds Averaged Navier Stokes
VOF	Volume of Fluid

Greeks

α	Normalised oil jet inclination angle	[−]
δ	Spacing	[−]
ϵ	Turbulence eddy dissipation	$[m^2\ s^{-3}]$
ζ	Pressure angle	[°]
κ	Surface curvature	[−]

μ	Dynamic viscosity	$[Pa\ s]$
ν	Kinematic viscosity	$[m^2\ s^{-1}]$
ρ	Density	$[kg\ m^{-3}]$
σ	Surface tension	$[N\ m^{-1}]$
ϕ	Volume fraction	$[-]$
χ	Dimensionless axial coordinate	$[-]$
ω	Angular velocity	$[rad\ s^{-1}]$

Subscripts

a	Tooth top land
air	Air property
ave	Average property
axial	Axial property
c	Casing property
f	Tooth face
g	Axial Gap
imp	Impact
j	Jet property
l	Liquid property
max	Maximum value
n	Normalised property
p	Pitch property
radial	Radial property
root	Tooth root
s	Shaft property
t	Tangential value
0	Zero value

Superscripts

$*$	Critical property
$'$	Fluctuating property

Introduction

To reduce the environmental and climate impact from air traffic, the aero-engine industry and research community have been striving towards alternative engine configurations, aimed at a significant reduction in emissions, noise and fuel consumption [1].

An improvement of the specific fuel consumption (SFC) can be achieved by increasing the thermodynamic and propulsion efficiencies [2]. For a conventional gas turbine cycle the thermal efficiency is mainly function of the overall pressure ratio and the turbine entry temperature. However, the potential for improving the thermodynamic efficiency is limited because it has already achieved a very high level [3]. The turbine entry temperature in fact is today in the range of 1900 - 2000 K, then a further increase is strongly depend on future advancements in material and cooling technology [4]. Increasing the cycle pressure ratio above 40 will yield only a small fuel consumption benefit [3]. Therefore one way to significantly improve the fuel efficiency of aircraft engines is to increase the propulsive efficiency.

Today's modern aircraft are mainly powered by turbofan engines. In this architecture, shown schematically in Figure 1, a large fan at the front of the engine accelerates the air between the front and the end of the engine. The main components of the engine are: the fan, which is a large diameter propeller, the low and high pressure compressor, which increases step by step the pressure of the air, the combustion chamber, the high and low pressure turbine, which extract energy from the hot gas, and finally the exhaust nozzle. Modern turbofans use generally a

two spool engine arrangement in which the fan is connected with the low pressure compressor and turbine by the Low Pressure (LP) spool, while a second concentric shaft, the High Pressure (HP) spool, connects the HP compressor and HP turbine. In turbofan engine the large amount of the air accelerated by the ducted fan is split into two flows: the by-pass flow, which passes through the fan and the bypass duct, and the core flow that goes through the core of the engine. The bypass ratio (BPR) is the ratio between the bypass flow and core flow; current conventional turbofans have a BPR in the 6-8 range [2].

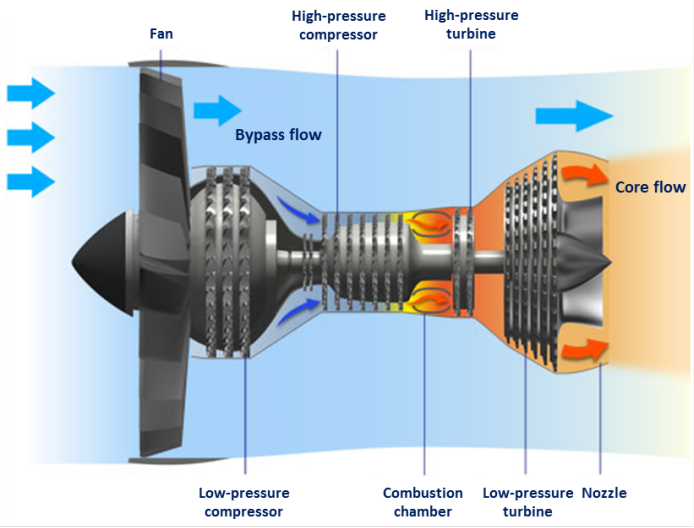

Figure 1: Turbofan engine layout (Figure adapted from [5]).

It is widely acknowledged that a significant improvement of propulsion efficiency can be achieved by enhancing the engine bypass ratio, which allows a sensibly reduction of specific fuel consumption as well as noise and emissions [2].

In conventional turbofan engines, an higher BPR is achieved by increasing the fan diameter which results in a reduction in LP spool speed. This in turn increases the number of stages for the low spool compressor

and turbine in order to retain satisfactory efficiencies and pressure ratios for these components. In addition, reduced low spool speed imposes higher torque requirement of the LP shaft which results in bigger shaft diameters and hence increases the core size. On the other hand, the Low Pressure Turbine (LPT) diameter and its number of stages also increase, in order to run a bigger diameter Fan [1]. Therefore, for conventional turbofan engines, the maximum gain in propulsive efficiency is limited, since the engine would need an excessive number of stages in the low pressure system if BPR increases above 10 [3].

A solution can be found by introducing a reduction gearbox between the fan and the low pressure system.

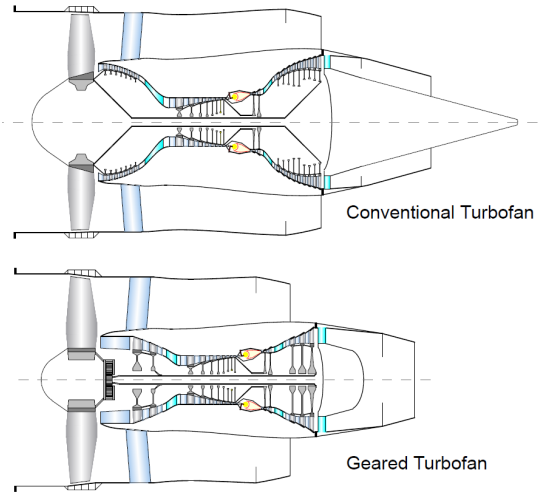

Figure 2: Common core conventional and geared turbofan with BPR = 10 [3].

The Geared Turbofan (GTF) technology is one of the most promising engine configurations to sensibly increase the engine bypass ratio. In this architecture, a power epicyclical gearbox is interposed between the fan and the low-pressure spool. The gearbox allows both fan and low pressure system to run at their optimum speeds. The fan speed can be selected as

low as required to achieve maximum efficiency and minimum fan noise. The LP shaft speed can be sensibly increased, allowing a considerable reduction in number of stages of low pressure compressor and turbine [6].

Kurzke [3] compared a conventional turbofan engine with a geared configuration for equal bypass ratio (BPR = 10), thrust and SFC; the layout of such engines is shown in Figure 2. As shown in the picture, the geared turbofan has clearly a lower number of parts than the conventional engine. However, Kurzke pointed out how it was difficult to know which of the two engines is the lighter one, because of the weight of the gearbox and the additional oil cooler which must be considered [3]. Therefore, the real added-value of the geared turbofan concept is the capability to increase significantly the BPR, well above of the values achievable with the conventional turbofan layout.

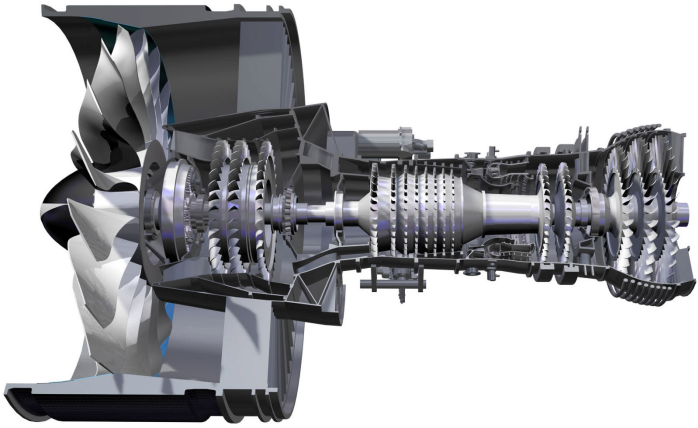

Figure 3: Pratt & Whitney PW1000G engine cross section [7].

Pratt & Whitney has developed a GTF engine called as Pure Power PW1000G, which develops thrust in the range of 10000-40000 lbf (44.5 - 177.9 kN) [7]. A cross section of the engine is reported in Figure 3. The engine (model PW1524G) for the Bombardier CSeries aircraft completed its first flight test program, logging 25 flights with 115 flight hours in

September 2011 [7]. For this engine, which has a bypass ratio equal to 12 and a nominal thrust of 24000 lbf (107 kN), is claimed an improvement in fuel burn by 16 % versus current best engines as well as a significant reduction in noise at up to 20 decibels below today's most stringent standard [8].

The reduction gearbox is a planetary gear system, shown in Figure 4, which envisions a 3-to-1 gear ratio accomplished in a single stage [9]. The low pressure shaft driving a sun gear, and five planetary gears enmeshed between the sun gear and a ring gear non-rotating relative to the engine nacelle. A carrier cage, holding the planetary gears, drives the fan.

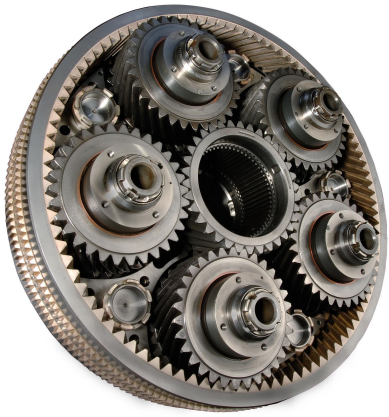

Figure 4: Pratt & Whitney planetary gear system [9].

The gearbox affects directly the engine SFC by the transmission efficiency and indirectly by the weight and the size of the cooling system. Therefore the gearbox performance becomes a key factor to achieve the benefits introduced by the GTF architecture. Although the efficiency of such systems is higher than 99 %, power losses are very important in high power applications. These losses are a source of heat that has to be removed and managed by the engine thermal system, composed by oil circuits and air-oil heat exchangers, which are sources of weight and parasite drag. This actually limits the use of the geared turbofan

configuration only to low thrust engines: it should be noted in fact that the maximum thrust developed by PW1000G engines is about 178 kN. Therefore, the development of geared turbofan for high thrust engine class (350-450 kN) is strictly depending on the gearbox performance improvement.

An efficiency enhancement can be achieved developing a physical understanding of the losses within the transmission system. Generally, the sources of power losses in such systems are classified into two main groups [10]:

- load-dependent;
- load-independent.

The former are primarily related to a mechanical power loss due to friction at the gear contact and in the bearings races, whereas the load independent power losses are associated with fluid-dynamic effects, which can be in turn affected by the lubrication method. If the losses of these two groups are often comparable under high-load and low-speed conditions, the fluid dynamic losses are dominant in high-speed, heavily-loaded mechanisms, such as the power transmission gearing equipment used with gas turbine engines [10]. While there has been a large body of work dealing with load dependent power losses and suitable models for the prediction are already available, the fluid-dynamics losses still need to be studied and properly modelled [11].

There are many sources of fluid-dynamics losses, the primary ones being windage losses, that are present as a result of oil/air drag on the periphery and faces of the gears, lubrication losses, pocketing/squeezing of lubricant from the cavities of the gear mesh, and viscous dissipation of bearings. These losses are a source of heat that are adding to the significant amount of heat generated by the friction of the mating gear teeth, and which has to be removed by the oil system. The primary purposes of such a system are to cool the gear teeth, preventing excessive tooth temperatures, and to lubricate the mating gear teeth for reducing surface wear due to metal-to-metal contact.

Several methods for gear cooling are adopted, depending on the pitch line velocity. In very high-speed and high power conditions, typical of aero-engine power-trains, the cooling is normally provided using nozzles to create small oil jets that feed oil into the meshing zone (see Figure 5). As oil is sprayed on the gears, it builds up an oil film layer on the teeth that is used to reduce meshing frictional losses. Lubrication has to be continuously applied because centrifugal forces fling the oil off the gear shortly after its application [12]. The system thus consists of a multiphase flow, where dispersed oil droplets, resulting by both the spray system and fling-off mechanism, and continuous oil jets, coexist.

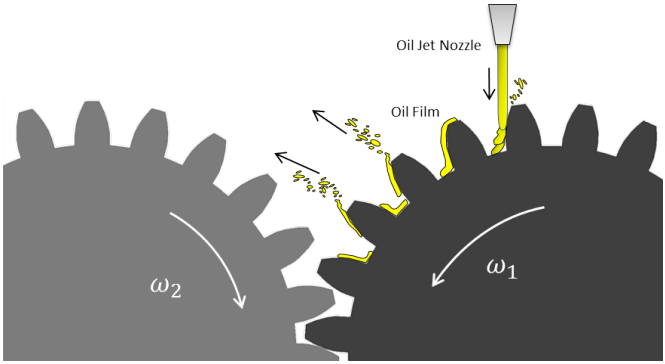

Figure 5: Oil jet cooling: evolution of the oil on the gear teeth.

A global study of the multiphase flow within the epicyclic gear train would be too complex and not useful in the understanding of the various loss mechanisms, therefore each one should be studied individually, by referring to simpler geometries.

Research context

In this framework, the Department of Industrial Engineering of the University of Florence (DIEF) launched a research project aimed at analysing, both experimentally and numerically, the fluid-dynamic losses in

high-speed gearboxes. Such a research work was developed in cooperation with GE Avio S.r.l, global leader in designing and manufacturing of power gearboxes for aero-engine applications.

A High Speed Test Rig was designed and manufactured. The test bench allows to reproduce the fluid-dynamic phenomena affecting a spur gears pair, with wheels having characteristic dimensions typical of those ones adopted in a planetary gear for power applications. In order to analyse every fluid dynamic loss individually, the test bench was designed to operate also with a single gear installed, by removing the driven shaft of the gearing. The main objectives related to this experimental activity are: gain a deeper knowledge of fluid-dynamic power losses in gearing systems, detect and analyse the sources of losses correlating them with gear parameters, and validate the CFD models developed during the research activity, both in terms of fluid dynamic losses and flow field reproduction.

Although the design of the test rig forms a significant part of the research activity, it will not be discussed in this thesis.

Aim of the work

This research study is aimed at defining CFD methodologies to be used in the comprehension of fluid-dynamic losses in gearbox systems for aero-engine applications, to develop predictive tools to be used in industrial design process. Because of this, the computational effort is an important aspect to be considered and therefore numerical approaches able to guarantee a good compromise between computational cost and reliability of the representation of the physical phenomena have to be selected. The power losses related to the windage phenomena and to the oil jet lubrication method were investigated, in a simplified configuration consisting of a single high speed spur gear.

A comprehensive numerical study about the windage losses of a single spur gear rotating in air has been performed by means of ANSYS FLUENT; the experiment of Diab et al. [13] has been computationally replicated.

Steady state RANS calculations in the rotating frame of reference have been performed with conventional eddy viscosity models. The numerical results have been compared with experimental data, defining a numerical setup to be used for the prediction during design phases. After that, the model has been adopted to simulate a single gear enclosed within an cylindrical casing, to assess the effect of the boundary walls on the power losses. Thanks to the improvement on the physical understanding of such a loss mechanism, a correlative approach available in literature has been modified, introducing the effect of the casing dimensions on the windage power loss calculation. The improved formulation has been tested with the experimental data.

Concerning the losses due to the oil jet lubrication, a comprehensive numerical study of an oil jet impinging on a high-speed spur gear has been carried out using the Volume of Fluid method available in ANSYS FLUENT. These simulations are aimed at improving the description of the complex physical phenomena characterizing the oil jet lubrication and the resulting liquid film formation in high speed gearing systems, within the context of transient RANS calculations. However VOF approach requires a very fine mesh in the liquid region, leading to very high computational efforts. In this respect, a strategy for local grid refinement and coarsening has been developed to confine the adaptation to selected domain regions, reducing heavily the numerical effort. Finally, VOF simulations were performed varying the oil injection angle and injection velocity, to assess how these parameters affect the power losses as well as the lubrication performance. As main result, a simplified formulation for the prediction of the power losses due to the oil jet lubrication has been developed, coming to the definition of an optimum configuration for such a system. It is important to underline that the VOF study of the oil jet lubrication presented in this work is one of the first in literature which provides detailed insight on the physic of the such lubrication method.

Finally, the methodologies developed in this work has been compared with the preliminary experimental data achieved by the High Speed Test Rig.

Thesis Outline

During this research activity the aspects related to windage and oil jet lubrication losses in a high speed spur gear were analysed, from both numerical and correlative points of view. The main achievements are related to the definition of numerical models aimed at improving the description of the physical phenomena characterizing such losses. However, since many efforts have been spent in order to deepen the knowledge of fluid-dynamic losses in high speed gearing, a comprehensive description of such losses is provided. The dissertation will be organized as it follows:

Chapter 1. In the first part of the chapter, the fluid dynamic losses in gearing systems are presented, with special emphasis on the windage and oil jet lubrication losses. In the second part, a brief introduction to computational methods for multiphase flows is reported, by focusing on the Volume of Fluid approach used in this work.

Chapter 2. This part is devoted to the numerical simulation of windage losses of a single spur gear rotating in air. The experiment of Diab et al. [13] was discussed and used to validate the CFD model. Finally, the correlative approach developed in this research is discussed.

Chapter 3. In this chapter the VOF studies about the oil injection losses are reported, detailing the physical phenomena that characterize such lubrication method. The resulting numerical model was adopted to perform several simulations by varying both oil jet inclination and injection velocity, evaluating how these parameters affect the resistant torque and the lubrication performance.

Chapter 4. This chapter deals with the preliminary comparisons between the numerical results and the experimental data achieved by the High speed test rig.

In the last chapter, a summary of the main achievements of this research is given together with conclusions.

Chapter 1

Technical background

This research activity is aimed at defining CFD methodologies for investigating fluid dynamic losses in gearbox systems for aero-engine applications. In the first part of this chapter the main fluid dynamic losses in gearing systems are presented in detail, reviewing the main experimental and numerical works available in the open literature. Special attention has been paid to windage and oil-jet lubrication losses. In the second part, a brief introduction to computational methods for multiphase flows is reported, focusing on Volume of Fluid approach used in this work.

1.1 Fluid-dynamic losses in high speed gears

Gearboxes are high-performance systems for mechanical power transmission. Although the efficiency is usually higher than 99 %, power losses are significant in high power application. Further improvement of efficiency can be achieved developing a physical understanding of losses within the transmission system.

Sources of power losses in a gearbox can be classified into two groups [10]:

- load-dependent;
- load-independent.

The former are primarily related to a mechanical power loss due to friction at the gear contact and between the rolling elements and the races of the bearings, whereas the load independent power losses are associated with fluid-dynamic effects and they are directly related to the lubrication method. If the losses of these two groups are often comparable under high-load and low-speed conditions, the fluid dynamic losses are dominant in high-speed, heavily-loaded mechanisms, such as the power transmission gearing equipment used with gas turbine engines [10].

While there has been a large amount of work dealing with load dependent power losses and suitable models for the prediction are already available, the fluid-dynamics losses still need to be studied and properly modelled [11].

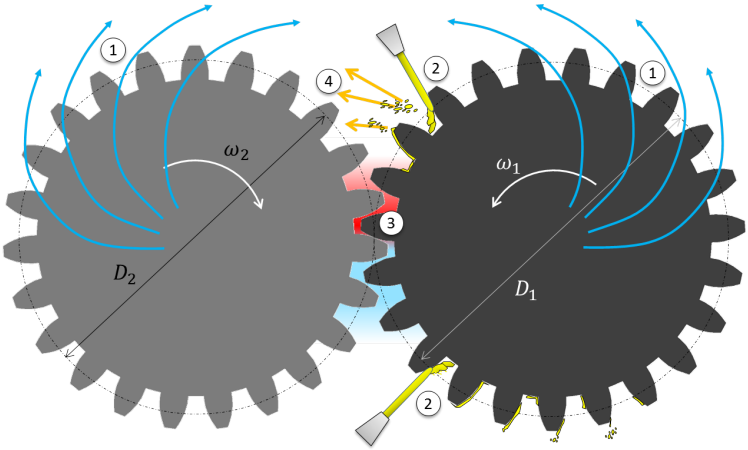

Figure 1.1: Representation of the fluid dynamic losses in a gear pair.

There are several sources of fluid-dynamics losses within gearbox systems. By referring to a spur gears pair, represented in Figure 1.1, that operates at very high speed conditions consistent with aero-engine applications, the primary sources of fluid dynamic losses are:

1. Windage losses;

2. Oil injection losses;

3. Meshing losses;

4. Oil recirculation losses;

5. Viscous dissipation of bearings

It is essential to point out that the relative magnitude of these mechanisms varies depending on the applications, and the operating conditions.

In the present chapter each loss mechanism will be treated individually, whereas the losses due to viscous dissipation of bearings as well as the oil recirculation losses will not be considered.

1.1.1 Windage losses

Windage losses refer to the power losses associated with the aerodynamic forces (pressure and viscous) experienced by the gear when it is running in air or an air-oil mist [11].

The available open literature on gear windage is not very extensive, on the contrary, numerous studies have been conducted on rotating disks. Many authors studied the flow above a flat disk which rotates about a vertical axis perpendicular to its plane with a uniform angular velocity (ω), in a fluid initially at rest. The torque opposing the rotation, due to the surface friction of the fluid, was calculated originally by Von Kármán [14], both for laminar and turbulent flow. The motion of a fluid is turbulent if Re_ϕ is greater than about 10^5 [15], where Re_ϕ is the rotational Reynolds number based on the disk radius (R) and tip velocity, given by Equation 1.1.

$$Re_\phi = \frac{R^2\omega}{\nu} \tag{1.1}$$

By applying the boundary conditions for a laminar flow over a rotating disk to the Navier-Stokes equations, after some approximation, Von Kármán found that the moment for both sides of the disc, neglecting edge effect, was:

$$2M = 1.84R^4\rho\nu^{1/2}\omega^{3/2} \tag{1.2}$$

where M is the moment due to one side of the disk. By approximating the boundary layer velocity profile using a 1/7th power law model, Von Karman found that the torque for turbulent case was given by Equation 1.3.

$$2M = 0.0728R^5\omega^2\rho\left(\frac{\nu}{R^2}\omega\right)^{1/5} \tag{1.3}$$

Both the equations can be described in terms of the moment coefficient, C_m, given by Equation 1.4, obtaining the Equations 1.5 and 1.6, for laminar e turbulent flows, respectively.

$$C_m = \frac{2M}{\frac{1}{2}\rho\omega^2R^5} \tag{1.4}$$

$$C_m = 3.68Re_\phi^{-1/2} \tag{1.5}$$

$$C_m = 0.146Re_\phi^{-1/5} \tag{1.6}$$

In 1935 Goldstein dealt with the turbulent boundary layer on a rotating disk [15]. He assumed a logarithmic profile for the boundary layer velocity, to better reproduce a particular set of experimental data. He achieved a moment coefficient of the form

$$C_m^{-1/2} = 1.97\log\left(Re_\phi C_m^{1/2}\right) + 0.03 \tag{1.7}$$

Dorfman [16] investigated the turbulent flow due to rotating disks with smooth and rough surfaces. Assuming a logarithmic velocity profile, he obtained, for a smooth surface, the momentum coefficient given by Equation 1.8, while for rough surfaces the C_m reported in Equation 1.9 was derived; in the latter a fully turbulent boundary layer was assumed.

$$C_m = 0.982\left(\log Re_\phi\right)^{-2.58} \tag{1.8}$$

$$C_m = 0.108\left(\frac{k_s}{Re_\phi}\right)^{0.272} \tag{1.9}$$

To summarise, the moment experienced by a rotating disk is totally due to shear forces; every author found that torque, related to both sides of the disk, depends linearly by the fluid density, in a quadratic way

by the angular velocity and by a fifth power of the disk radius. Their formulations differ in the value of moment coefficient, which is in all relation a decreasing function of the rotational Reynolds number.

Various experimental studies of gearbox windage are available in the open literature. Townsend [17] identifies a series of factors that influence windage losses, identifying the pitch line velocity as critical parameter; windage effects become important when the pitch line velocity exceeds 50 m/s. Townsend developed an approximated empirical formula for windage estimation derived by empirical studies on smooth rotating bodies in air. However, as commented by Townsend, this method is not able to predict actual losses, but it is mostly used in establishing when the windage effects become an issue for designers.

Anderson and Loewenthal [18], [19] presented an analytical method for calculating all of the losses in a gear train, developing a formula for a pinion-gear pair in mesh:

$$P = C_1 \left(1 + 2.3\frac{t}{R_p}\right) n^{2.8} {R_p}^{4.6} \left(0.028 * \mu + C_2\right)^{0.2} \tag{1.10}$$

where the power loss is expressed in kW, C_1 and C_2 are constants equal to $2.87 \cdot 10^{-7}$ and 0.019, t is the gear face width (meters), R_p is the pitch radius (meters), n is rotation rate in revolutions per minute, and ρ and μ are the fluid density (kg/m^3) and viscosity (centipoise),respectively. However, that study involved relatively low-speed gearing, with pitch-line velocities up to 40 m/s.

In 1984, Dawson [20] performed interesting studies of windage loss for single spur gears in air, evaluating how the losses are affected by speed, size, gear geometry, and shrouding. The gears were operated in a spin-down test rig, where the wheel was initially accelerated to a maximum rotation speed (root-line velocities up to around 90 m/s), then the supply was disconnected allowing the free deceleration of the gear. Windage power loss was calculated by measuring the rate of deceleration. Dawson concluded that the main source of gear windage losses was the tooth. By means of smoke, it was observed that the gear teeth act similarly to

blades of a centrifugal fan: the air is drawn in axially from both ends of the teeth and ejected out radially. Dawson also examined the effect of the gear case. A series of configurations of axial and radial shrouds of various shapes and sizes were tested; a percentage reduction in windage was recorded compared to the same gear rotating in free air. An empirical equation to predict the windage power loss (in kW) of a single gear was deduced by the measurements. It is expressed by Equation 1.11

$$P = n^{2.9}\left(0.16{D_r}^{3.9} + {D_r}^{2.9}F^{0.75}M^{1.15}\right)\cdot 10^{-20}\Phi\lambda \tag{1.11}$$

where D_r is the root diameter of the gear, F and M are is the tooth face width and module, respectively; all the lengths are expressed in mm. Φ is 1 for an oil free atmosphere, λ is equal to 0.6-0.7 in the case with gear in large casings, whereas is about 0.5-0.6 in 'fitting' ones or 1 for gears operating in free air.

Following the work of Dawson, Diab et al. [13] conducted experiments on a single high-speed spur gear rotating in a free oil environment without enclosures. Different spur gears were tested in a spin-down test rig, reaching pitch-line velocities up to 100 m/s. Two formulas were derived for windage power losses, one from dimensional analysis and the second based a simplified fluid flow analysis. The experimental results were also exploited for assessing the windage calculation expressions of Anderson and Loewenthal [18], Dawson [20], and those developed by Diab et al. The formulas developed by Diab showed improved results with respect to the older studies. In addition, it was shown that geometric changes of the flow field close to the gear teeth using shrouds and/or baffles can significantly reduce windage losses. The formulation presented by Diab et al. reports the power loss in Watt as a function of fluid density ρ (kg/m^3), rotation rate ω (rad/s), pitch radius R_p (m) and a total windage loss coefficient C_t:

$$P = \frac{1}{2}C_t\rho\omega^3{R_p}^5 \tag{1.12}$$

Two different formulations were provided for the C_t calculation; more insights about this will be provided in a later chapter.

To summarise, in Figures 1.2, 1.3 and 1.4 the windage power loss predicted by the formulas of Anderson and Loewenthal, Dawson and Diab are compared. A sample spur gear having 4 mm module and a pressure angle 20° was considered. All of the experimental studies conducted on single spur gears show a nearly cubic relationship between rotational speed and power loss, as visible in Figure 1.2, a dependency with the pitch radius expressed as a power law having the exponent that varies between 3 and 5 (see Figure 1.3), whereas windage is a nearly linear function of the gear face width, how it can be observer by Figure 1.4.

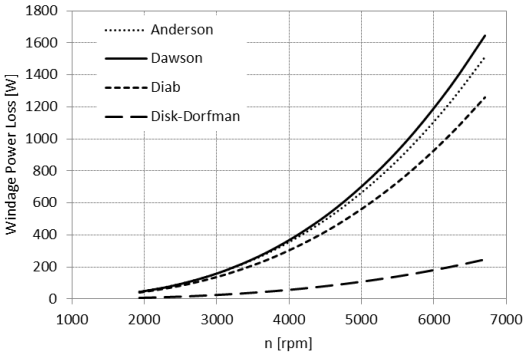

Figure 1.2: Windage power loss for a spur gear having a 288 mm pitch diameter, a 30 mm face width, 4 mm module, by varying the rotating speed: comparison between the results obtained by the formulas of Anderson and Loewenthal, Dawson, Diab and Dorfman (Rotating disk).

In Figure 1.2, the power losses predicted by the Dorfman's correlation (Equation 1.8) resulting by the two sides of a rotating disk was reported. As concluded by Dawson the key source of gear windage losses are the teeth; in fact, the prediction of the Dorfman's formula is significantly lower than all the other correlations developed for gearing.

The understanding of flows around gears is of primary importance to design specific deflectors for reducing fluid-dynamic losses. These informations cannot be provided by a correlative approach, while it may

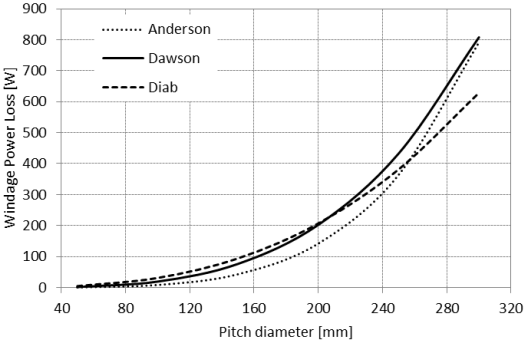

Figure 1.3: Windage power loss for a spur gear having a 30 mm face width, 4 mm module, by varying the pitch diameter: comparison between the results obtained by the formulas of Anderson and Loewenthal, Dawson and Diab, at a rotating speed of 5000 rpm.

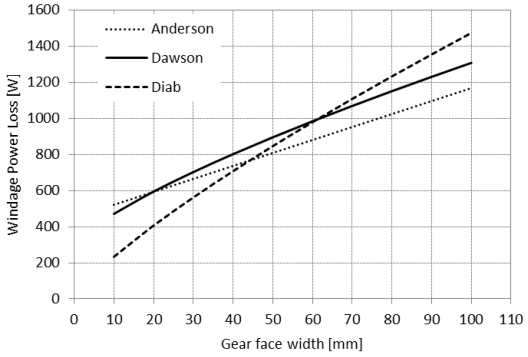

Figure 1.4: Windage power loss for a spur gear having a 288 mm pitch diameter, 4 mm module, by varying the face width: comparison between the results obtained by the formulas of Anderson and Loewenthal, Dawson and Diab, at a rotating speed of 5000 rpm.

be accomplished by means of computational fluid dynamic analysis (CFD), which allows to separate the losses due to viscous and pressure effects, as

well as to understand the effects of tooth geometry.

Farrall et al. [21] performed steady-state, single phase simulations for a shrouded bevel gear using the commercial code ANSYS FLUENT. The results were in contrast to the significant reduction in the windage loss found in some previous experimental studies [22]. The discrepancy was attributed to the fact that Farrall did not study the same gear or shroud design as in the experiments.

Al-Shibl et al. [23] performed two-dimensional (2D) simulations of a spur gear using ANSYS FLUENT; the model domain was consisted of a sector of a spur gear comprising two teeth. The 2D model allows to calculate the flow over the teeth assuming they are of infinite thickness. In order to take account for three-dimensional (3D) effects, an expression for the side power loss, taken from Townsend [17], was exploited. Computations were compared against data from experiments but the predicted results tended to underestimate the loss of about 40 %.

Similarly to Al-Shibl et al., Marchesse et al. [24] carried out CFD simulation using the commercial code ANSYS CFX to study the windage power loss of a single spur gear; 2D and 3D modelling, different turbulence and boundary conditions were tested. The numerical results were compared to experimental data from a specific test rig in order to validate the most appropriate modelling. He found that the 3D model provided a significantly improved calculations of gear windage losses, reporting a good agreement with experimental data.

Hill et al. [25] implemented a 3D unstructured moving mesh method and applied it to study windage losses for isolated spur gears in air and validated their predictions against data from Diab et al. [13]. Subsequently, Hill et al. [26] adopted their CFD model to investigate the aerodynamics of single gear in various shrouding configurations. Comparisons were made with experimental data from the NASA Glenn Research Center Gear Windage Test Facility. They observed a reduction of windage losses in shrouded configurations, pointing out that windage losses are mainly caused by pressure forces acting on the tooth surface instead of shear effects, and this applies both to free gear and shrouded configurations.

1.1.2 Oil injection losses

The temperature of the gear tooth surfaces is a crucial parameter for the working performance of high speed and heavy load gears, having effect on phenomena of failure such as scoring and scuffing, which frequently occur in such transmissions [27]. Therefore, it is essential that the gear teeth are properly lubricated and that enough oil gets into the tooth spaces for sufficient cooling, to prevent gearbox failure.

There are several methods adopted for gear cooling and lubrication, depending on the pitch line velocity. For gears operating at low speeds and low loads the lubrication method is not critical, since little heat is generated [28]. At such conditions, splash lubrication is generally adopted, with the gears partly submerged in the lubricant. With splash lubrication, power losses increase considerably with the tangential velocity [29], and gears have to be lubricated by pressure fed systems. For very high-speed (pitch velocity above 100 m/s) and high power conditions, typical of aero-engine transmissions, the main part of the lubricant must be used for cooling the teeth. The lubrication is provided using nozzles to create small oil jets directed toward the gear tooth surfaces, so that the oil is supplied to each tooth once per revolution. This method provides high cooling performance as well as adequate lubrication; it is an attractive technique because of the relatively high heat transfer rates for a given mass flow rate [30].

The power losses are resulting from the momentum transfer between the gear tooth and the impinging oil jet. A good understanding of the oil-jet behaviour inside gearbox is desirable, to minimize lubrication losses and reduce the oil volume involved.

For gearbox designers is very important to understand how oil penetrates into the gear tooth space under dynamic conditions, to determine how much of the impinging oil is involved in the cooling and lubrication processes. The oil jet impingement depth is the point where the lubricant jet collides with the gear tooth, whereas the penetration depth is the maximum depth of lubricant penetration after impingement; the penetration depth is usually larger than the impingement depth [31].

Akin et al. [31] conducted significant experimental tests about spur gear oil jet lubrication, varying both gear and oil-jet velocity. The gear had a 88.9 mm pitch diameter, a tooth hight of 7.62 mm and a pressure angle of 20 degree, while the speeds were 2560 and 4290 rpm, which correspond to gear pitch line velocities of 12 and 23 m/s. The nozzle adopted in their tests had 80° spray angle and 1.1 mm diameter orifice. The oil jet pressure was varied for each speed of rotation, to achieve various oil jet speeds, as well as impingement depths into the gear tooth space. The authors indicated that in all the test conditions the oil jet was either a continuous stream or large droplets. Pictures of oil jet lubrication were taken with a high speed motion camera, illuminating the lubricant with a xenon lamp. The lubricant was added approximatively 10 % by volume of white lithopone pigment to highlight the oil when it was illuminated. The more interesting findings are summarised below.

In Figure 1.5 the oil jet penetration into the tooth space at 4920 rpm ($10.5 \cdot 10^4$ Pa nozzle pressure) is shown. In picture 1.5-a the beginning of oil jet penetration into the tooth space is visualised: the effects of windage on the oil jet stream can be seen, in fact the jet is bending to the right in the direction of rotation, moreover, a droplets formation as a result of an aerodynamic interaction is evident. Figure 1.5-b shows the oil jet at impingement with the gear tooth. It is visible how the jet is broken up by the impact.

In Figure 1.6 the total penetration of the oil particles before and after tooth impingement is illustrated for both rotating speeds; the pressure of the oil system was about the same in both speeds. Hence, by comparing the picture a and b the windage effect on the oil jet behaviour can be assessed. It can be observed how the oil stream is heavily warped as the speed of rotation increases, due to a higher velocity of the air. Furthermore, Akin et al. pointed out that the particles after the impingement are much smaller than before, highlighting how a large percentage of these particles are carried out of the tooth space without further contact with the teeth thereby providing some lubrication but very little cooling [31].

Figure 1.7 the oil jet phenomenon was analysed at 2560 rpm, with an

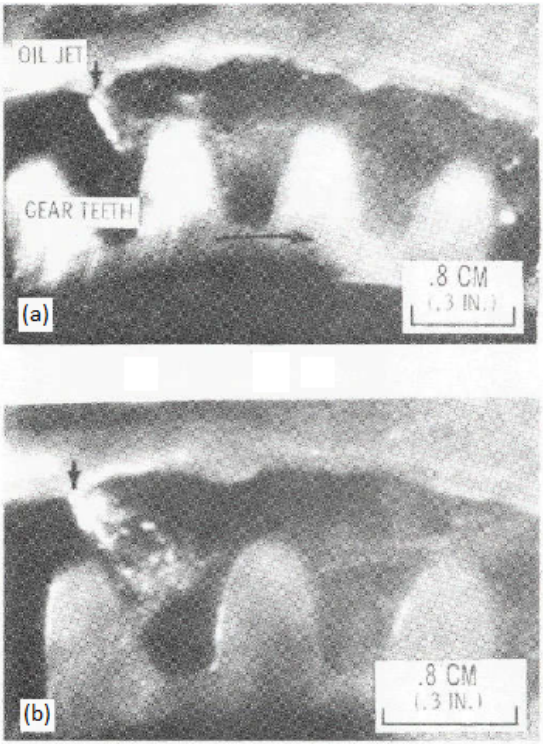

Figure 1.5: Oil jet penetrating tooth space and impinging tooth; speed, 4920 rpm; oil pressure, $10.5 \cdot 10^4$ *Pa [31].*

injection pressure of $9 \cdot 10^4$ Pa, hence in this test the oil jet velocity is reduced with respect to that one reported in Figure 1.6-b. The picture shows the oil jet penetrating into tooth space before the impingement: a reduction of windage effects on the liquid-jet is clear. The decrease of aerodynamics forces also reflects on the oil jet interaction with the tooth, in fact, the oil stream is more compact during the impingement. In Figure 1.6-b it can be observed how the jet breaks up in small particles, bouncing off by the tooth surface.

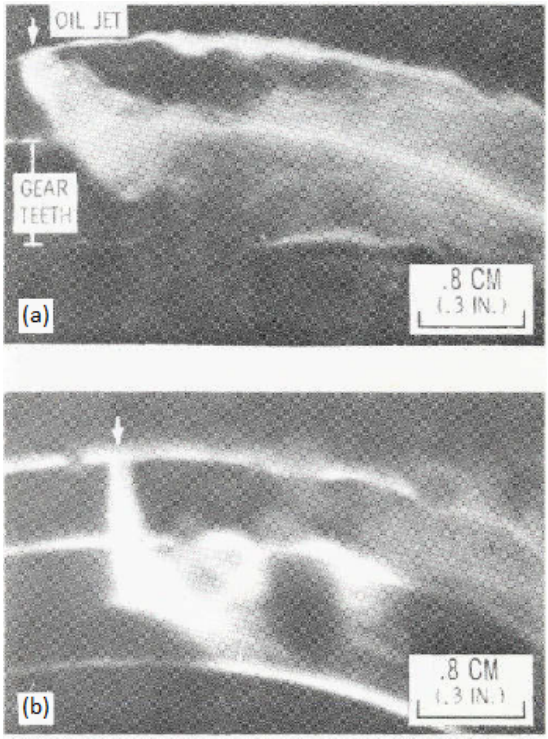

Figure 1.6: Oil jet impingement and subsequent penetration into the tooth space; (a) 4920 rpm and oil pressure of $14 \cdot 10^4$ *Pa; (b) 2560 rpm and oil pressure of* $13 \cdot 10^4$ *Pa [31].*

In the same work, Akin et al. developed an analytical model to calculate the impingement depth, taking into account windage effects. By modelling the oil jet as a continuous stream of large droplets, its fundamental equation of motion was derived, resolving the lubricant trajectory. For every test, the individual frames were achieved, to determine the depth of oil jet penetration into the gear tooth space. A good agreement between the analytical model and the experimental outcomes was proved.

In summary, the study reported how an optimal oil penetration depth

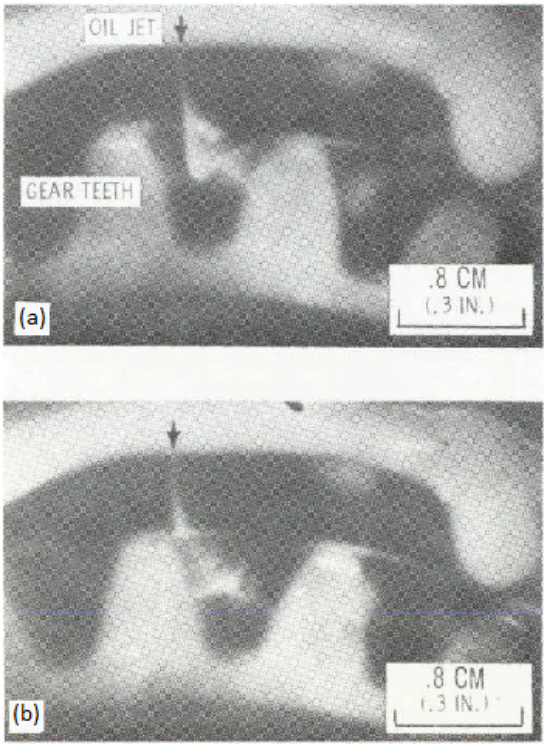

Figure 1.7: Oil jet penetrating tooth space and impinging tooth; speed, 2560 rpm; oil pressure, $9 \cdot 10^4$ *Pa [31].*

is provided when the jet was not atomized, showing how small droplets were affected by aerodynamic flow field. No data was collected about the resisting torque due to the oil-gear interaction, as well as the associated power losses.

When the oil reaches the gear tooth surfaces, it is subjected to centrifugal forces which fling off the oil from the gear teeth. Dewinter and Blok [32] presented a theory aimed at investigate the cooling capability of the fling-off process, in fact, during the oil motion on the tooth surface,

the lubricant progressively absorbs heat from the tooth face with which it is in thermal contact. By hypothesising that the oil jet reaches the tooth without the occurrence of deformation and break up phenomena, they indicated that the oil jet after the impingement splits up into two streams, one of which moves down towards the tooth root, as sketched in Figure 1.8. In their theory, the radially inward stream may well reach the tooth root, then cross the bottom of the adjoining tooth space so as to reach, climbing, and thereby cover also the opposite tooth face. If this were true, then adequate cooling could have been obtained with lower oil jet mass flow rate [31].

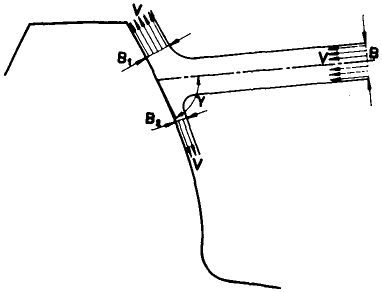

Figure 1.8: Branching of sheet-shaped impinging jet [32].

Later, El-Bayoumy et al. [33] analysed the hydrodynamic forces acting on a fluid particle near the tooth surface above and below the point of impingement. Considering a non inertial frame of reference integral with the gear, and rotating with constant angular velocity, the acceleration of the fluid particle is given by Equation 1.13:

$$\vec{a} = \vec{\omega} \wedge \vec{\omega} \wedge \vec{r} - 2\vec{\omega} \wedge \vec{V} \tag{1.13}$$

where $\vec{r}$ is the radius vector to the particle, and $\vec{V}$ is the relative velocity of jet impingement. The two terms appearing on the right hand side of equation are the centrifugal and Coriolis acceleration components. In supporting the explanation, in Figure 1.9 a sketch of the acceleration

components related to the oil film on the toot surface is shown.

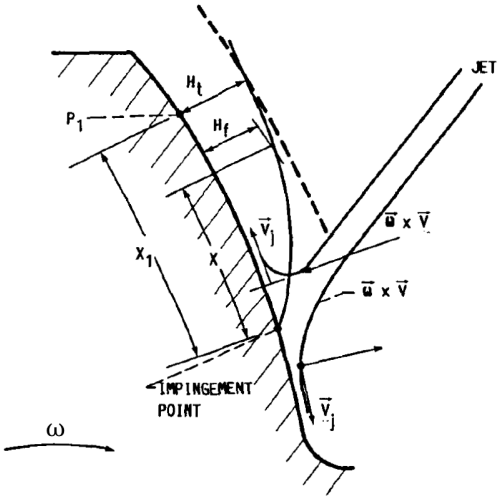

Figure 1.9: Centrifugal and Coriolis accelerations above and below impingement on gear tooth [33].

The magnitude of the former is $\omega^2 r$ and tends to strip off the oil layer from the surface of the tooth, which is expelled in radial direction. It is worth noting that, as the oil moves toward the tooth top land, the centrifugal actions increase. The magnitude of the Coriolis acceleration is $2\omega V_j$ where V_j is the jet velocity relative to the gear. Since V_j is of the same order of magnitude as the gear pitch velocity, the Coriolis component cannot be neglected. As illustrated in Figure 1.9, for points on the tooth profile below impingement, the direction of the Coriolis acceleration is normal to the tooth surface pointing outward. Conversely, for points above impingement the Coriolis acceleration points inward, establishing a "pseudo-gravitational" field [33].

The main subject of the described work was the heat-transfer phenomena analysis on the gear tooth surface due to the oil jet cooling system, hence no data was reported about the power losses. However this work

provides useful insight about the oil film behaviour over the tooth surface.

More recently, Johnson et al. [34] presented an experimental study of the torque associated with a spiral bevel high-speed gear in shrouded configuration, analysing the effect of various lubricant mass flow rates and shroud layouts. The measured data reported a linear increase in average torque with the oil mass flow rate, in addition, a good agreement between the average torque, derived by a simple calculation based on the oil's momentum variation, and the experimental torque was shown. Visualization through a transparent shroud showed that the oil was trapped under the shroud, leading to oil recirculation losses. Johnson observed that the air and oil phases remained separate, indicating that analysis based on average fluid density may not be physical. Furthermore, this study highlighted how the resistant torque in shrouded gear can be considered as the sum of three main loss terms: single air windage, oil acceleration and oil recirculation.

CFD simulations could provide a more in-depth understanding of the interaction phases between oil jet and gears. However the simulation of such a system is very challenging, because involving transient multiphase flows, moving boundaries, and large three-dimensional domains which lead to high computational costs. For these reasons, numerical studies on this issue which provide detailed insight on the physic of the oil jet lubrication are not available in the open literature; on the contrary, some works concerning splash lubrication are present.

Li et al. [35] applied Volume of Fluid (VOF) and dynamic meshing methods to investigate the multiphase flow within a gearbox, consisting of a gear pair subjected to splash lubrication. The effects of speed, immersion depth and oil viscosity on the flow field were assessed. The commercial CFD code ANSYS Fluent was used, performing two-dimensional calculations. The predicted flow fields were compared with high-speed visualizations performed on a dedicated test rig, proving a qualitative good agreement between predictions and experiments. No information about the churning losses were provided. Arisawa et al. [36] carried out an experimental and numerical study of the windage and oil churning

losses within a prototype bevel gearbox. Lubrication oil was supplied to the gear meshing zone using many jet nozzles. The power fluid dynamics losses were derived by evaluating the difference between the oil discharge and supply temperature. The Volume of Fluid (VOF) and porous body methods were applied to model the two-phase flow and the gear meshing, respectively. A good agreement between CFD results, in terms of average power losses, and experiments was found. The global power losses were evaluated, while no data were reported about the contribution of the individual loss sources to the total loss.

1.1.3 Gear meshing losses

'Meshing Losses' means the power losses related to the compression and the subsequent expansion of the the fluid volume trapped between the meshing teeth. Concerning such a loss only a few works are available in literature.

From an analytical point of view, Rosen [37] has determined the airflow velocity in spur gears using an incompressible flow theory and, for a particular gear set, has found that sonic conditions can be reached in accordance with the experimentally observed rise in noise [38].

Wittbrodt [39] performed one-dimensional analysis of the fluid pumping action resulting from the meshing of spur gears. Two separate analyses were conducted, one using incompressible and the other using compressible flow theory. The former correspond to heavily lubricated gears whereas the latter are representative of lightly lubricated gearing system. The analysis demonstrated that the velocity of the discharged fluid reached high velocities for both cases. In fact, during a high speed mesh, the time duration of the arc of approach and recession can take in e very short time, so that the air-oil mixture is compressed and pumped out at high speeds between the teeth. If the air velocity between the teeth should reach sonic levels, a shock wave can form which emanates noise [39]. Furthermore, pressure and temperature rises inside the meshing region were found, thus that energy generated is dissipated in the air-oil mix and the other portion is absorbed by the gear teeth, which results in

a superficial temperature increase.

Houjoh et al. investigated velocity and pressure fields within a tooth space for meshing spur [40] and helical gears [41]. In particular, transient pressure signal was measured by a pressure transducer placed at the bottom of the tooth cavity.

Later, Diab et al. [38] developed a hydrodynamic model able to predict the compression-expansion process by the meshing teeth, comparing their results with the experiments performed by Houjoh et al. It was shown that pumping phenomenon may give rise to significant power losses, especially for high-speed applications.

Al et al. studied the flow field within the cavity created by meshing spur gears by means of CFD using a re-meshing technique available in ANSYS FLUENT. The experiment carried out by Houjoh et al. was computationally replicated; only eight teeth of each gear were simulated, in order to reduce the computational effort. That approach was proved difficult to use and remained computationally expensive.

Recently, Gorla et al. [42] performed an experimental and numerical investigation of the rotational speed effect on the fluid-dynamic total resistant torque in a completely oil filled gearbox. They exploited the Dynamic Mesh numerical approach available in ANSYS FLUENT, achieving a good agreement with experimental data.

1.2 Computational Methods for Multiphase Flow

By reference to Figure 1.1 in very high-speed gearing systems the lubrication is normally provided using nozzles to create small oil jets that feed lubricant into the meshing zone. As oil is sprayed on the gears, it builds up a lubricant film layer on the teeth that is used to reduce meshing frictional losses. Lubrication has to be continuously applied because centrifugal forces fling the oil off the gear shortly after its application [12]. The system thus consists of a multiphase flow, where dispersed oil droplets, resulting by both the spray system and fling-off mechanism, and continuous oil jets, coexist.

The term multiphase flow is used to refer to any fluid flow consisting of more than one phase or component which have separation at a scale well above the molecular level [43]. A phase is a thermodynamic definition for the state of the matter, which can be either solid, liquid or gas. In a multiphase flow several phases flow together. These ones may consist of one chemical component, e.g. flow of water vapour (steam), or of several chemical components, e.g. flow of oil and water [44]. It is clear that multiphase flows may appear under various forms, depending on the nature and amount of the fluids in the system. Multiphase flows can be classified accordingly to the geometry of the interfaces into three main classes, namely, dispersed flow, separated flows and transitional flows [45], as shown in Figure 1.10. The former consist of a dispersed phase

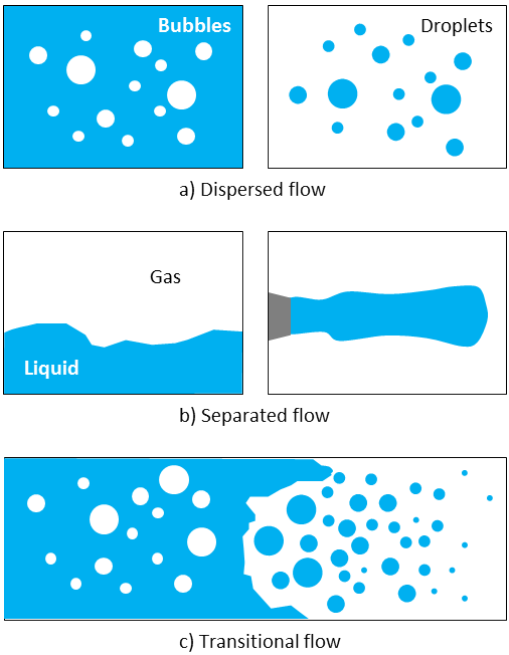

Figure 1.10: Classification of multiphase flows.

formed by particles, distributed in the continuous phase that may be gaseous or liquid. The dispersed particles may by solid, liquid gaseous; fluid particles formed by a gas phase are denoted as bubbles, while the liquid ones as droplets. On the other hand, the separated flows consist of two or more continuous and immiscible fluid which are separated by a distinct, large-scale interface. The change of interfacial structures usually occurs gradually, thus the third class is characterized by the presence of both separated and dispersed flow.

In a laboratory, it may be difficult to set up a multiphase flow experiment with the necessary degree of control: the breakup of a drop in a turbulent flow or a precise characterization of the bubble or drop size distribution may be examples of such issues. In this situation, numerical simulation becomes an essential tool for the investigation of multiphase flows [46]. Depending on the multiphase flow morphology, different CFD modelling approaches are suggested. Within the gearbox, the fluid environment consists of a two-phase two-components flow, i.e. the lubricant and air, in both dispersed and separated configuration. However, it should be recalled that one of the main objectives of this thesis is to investigate the power losses relating to a high speed spur gear subject to oil-jet lubrication, while the oil recirculation losses are not considered. Therefore only the numerical approaches suggested for separated flow modelling will be presented, whereas those ones for the dispersed and transitional flows will not be treated. In supporting the discussion, a diagram summarizing the main computational methods for the separated flows modelling is shown in Figure 1.11.

As mentioned above, the separated flows refer to two-phase or multiphase fluid flow problems that involve two or more immiscible fluids separated by sharp interfaces which evolve in time. Typically, when the fluid on one side of the interface is a gas the latter is referred to as a free surface. Many computational methods for the treatment of the free surface are described in literature, often classified by the method for the interface treatment (see Tryggvason et al. [47] for an extensive review). The existing computational approaches to solving interfacial flows can be

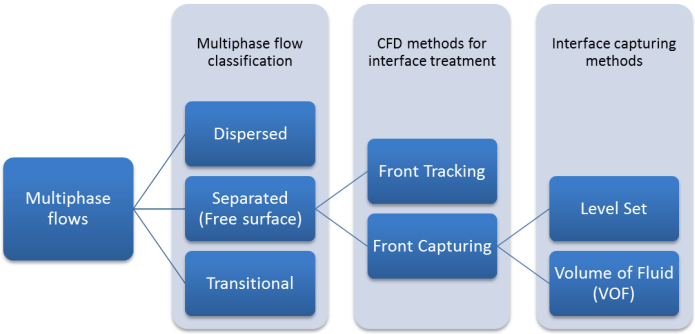

Figure 1.11: Diagram summarizing the main computational methods for the separated flows modelling.

classified into two groups: front tracking and front capturing. The former refers to methods that explicitly parametrize the interface and follow the points on the surface precisely in time. In front tracking, markers are tracked on an interface in a Lagrangian sense as the interface evolves, although the underlying flow field may be solved on a fixed Eulerian grid. This approach is not treated in the present work; for a detailed overview of the various methods available see Tryggvason et al. [48].

The other approach deals such problems by capturing the interface via an implicit representation. Basically, an interface capturing method follows an Eulerian description of fluid motion and has a fixed Cartesian grid covering the whole fluid domain; in such a method the sharp interface between two fluids is identified by an indicator function. Using the fluid velocities, the interface motion across the mesh is modelled by advecting the indicator function with the flowing fluid. The Level Set (LS) method (Sussman et al. [49]) and the Volume of Fluid (VOF) method (Hirt and Nichols, [50]) are the most famous and successful ones in the interface capturing family. In LS methods the interface is defined as a zero level set of a smooth distance function from the interface. This function is a scalar property and is advected with the local fluid velocity. The level-set approach, however, suffers from loss of mass in flow fields with appreciable

vorticity or in cases where the interface is significantly deformed [49]. In the VOF method, the volume fraction of one fluid phase in each computational cell is adopted as the color function to distinguish different fluids. A typical procedure in the VOF method contains a geometrical reconstruction and advection of the interface using the volume fraction [51]. The VOF method has good properties of volume conservation, but it is less accurate than LS method in the reconstruction of the interface curvature, therefore this affects on the calculation of surface tension forces [52]. Besides some improvements made individually to the VOF and LS methods, a coupled Level Set and Volume of Fluid (CLSVOF) method has been proposed to combine their advantages by Sussman and Puckett [53].

In this work the VOF approach has been adopted to investigate the oil-jet lubrication method, furthermore such a formulation will be presented in the hereafter section.

1.2.1 Volume of Fluid Method

Today's VOF methods are built on nearly four decades of research in this field, started by DeBar [54], Noh and Woodward [55] and Hirt and Nichols [50]. The VOF approach is a "one fluid" formulation which allows to compute the flow using methods developed for single phase flows. The various phases are treated as one fluid with variable material properties that change abruptly at the interface. Therefore, only one set of governing equations is exploited for the whole flow domain occupied by the various phases, consequently the resulting velocity and pressure field is shared among the phases. The derivation of the "one-fluid" equations is exactly the same as single phase flow except that it necessary to add the surface tension as a body force to the momentum equation [47]. Therefore the "one-fluid" version of the Navier-Stokes equation for incompressible, Newtonian flows with sharp interfaces are [47]:

$$\frac{\partial u_i}{\partial x_i} = 0 \tag{1.14}$$

$$\rho\frac{\partial u_i}{\partial t}+\rho\frac{\partial u_i u_j}{\partial x_j}=-\frac{\partial p}{\partial x_i}+\frac{\partial}{\partial x_j}(2\mu s_{ij})+\mathbf{f}+\mathbf{f}_\sigma\delta_S \tag{1.15}$$

where s_{ij} is the strain-rate tensor, given by Equation 1.16, $\mathbf{f}$ is the force per unit volume, frequently only the gravitational force $\rho\mathbf{g}$, and $\mathbf{f}_\sigma$ is the surface force per unit area.

$$s_{ik}=\frac{1}{2}\left(\frac{\partial u_i}{\partial x_j}+\frac{\partial u_j}{\partial x_i}\right) \tag{1.16}$$

The Equation 1.15 holds for the whole flow field, even if the density field ρ and the viscosity field μ change discontinuously. For constant surface tension, the surface force is

$$\mathbf{f}_\sigma\delta_S=\sigma\kappa\mathbf{n}\delta_S \tag{1.17}$$

with σ being the surface tension, κ the curvature of the front, $\mathbf{n}$ is the surface normal and δ_S is the Dirac delta function marking the interface.

The volume fraction of each fluid is tracked through every cell in the computational grid. The value of the volume fraction (also referred to as colour function or marker function) is between 0 and 1 in cells cut by the interface and equal to 0 or 1 away from it. The normal direction of the fluid interface is found where the value of indicator function changes abruptly. An example of a color function corresponding to a circle arc is shown in Figure 1.12. The evolution of the k-th fluid in a multiphase system of n fluids is governed by the transport equation for advecting the phase-indicator function $\phi(x;t)_k$:

$$\frac{\partial\phi_k}{\partial t}+\frac{\partial}{\partial x_j}(\phi_k u_i)=0 \tag{1.18}$$

The Equation 1.18 is not solved for the primary phase, in fact the volume fraction is computed based on the following constraint

$$\sum_{k=1}^{n}\phi_k=1 \tag{1.19}$$

The material properties depend locally on the indicator function. For each

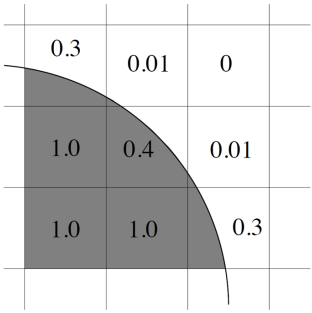

Figure 1.12: The exact color function for a smooth circular arc over a square grid [52].

cell, properties such as density ρ and dynamic viscosity μ are accounted for by a volume fraction average of all fluids in the cell:

$$\rho = \sum_{k=1}^{n} \rho_k \phi_k \tag{1.20}$$

$$\mu = \sum_{k=1}^{n} \mu_k \phi_k \tag{1.21}$$

In the case of a gas-liquid flow, e.g. the oil-jet within a gearbox system, the Equations 1.18, 1.19, 1.20 and 1.21 take the following form:

$$\frac{\partial \phi}{\partial t} + \frac{\partial}{\partial x_j}(\phi u_i) = 0 \tag{1.22}$$

$$\phi + \phi_g = 1 \tag{1.23}$$

$$\rho = \rho_l \phi + (1 - \rho_g \phi) \tag{1.24}$$

$$\mu = \mu_l \phi + (1 - \mu_g \phi) \tag{1.25}$$

where ϕ is the liquid volume fraction.

As the fluids move and the interface between the different fluids changes location, the volume fraction distribution must be updated. Doing this accurately is both critical for the success of simulations of free-surface

flows and also complex. The data ϕ are given at the beginning of a computational cycle but no approximation of the interface position is known. An algorithm for interface advection and reconstruction is needed [56]. Algorithms for volume tracking have been designed to solve the Equation 1.22 in a way that keeps interfaces sharp. Regular advection techniques (even those using flux-corrected transport) rapidly smear the interface over at least three or four mesh cells [57]. The solution is advected by a high-order scheme whenever a cell is completely filled with one phase or another, but around the discontinuity the solution is carefully modified. A detailed review of the various methods for the colour function advection is given by Tryggvason et al. [47] and Rudman [57]; the hereafter description is based on such works.

The Simple Line Interface Calculation method (SLIC), proposed by Noh and Woodward [55], was the first technique presented for the advection of colour function in two-dimensional flows. In this approach the marker function is firstly advected in one coordinate direction, secondly in the orthogonal direction. For advection in the horizontal direction, the cell containing the interface is divided into a full part and an empty part by a vertical line, by deciding which side is empty and which one is full depending on the volume fraction of the neighbouring cells. In three-dimensions this methodology has to be repeated for the third coordinate direction. A few years later, a different procedure was proposed by Hirt and Nichols [50] in which the interface was approximated by straight lines, as introduced by Noh and Woodward [55], but the same orientation was adopted for the advection in the different directions. Once the normal to the interface was calculated, by processing values of ϕ in the neighbouring cells, the interface orientation was chosen according to whether the normal was more closely aligned with the horizontal or vertical direction. The most important idea introduced by Hirt and Nichols in their method, also referred as donor-acceptor approach, was in the concept of reconstructing the interface in each computational cell based on the values assumed by the marker function in the neighbouring cells. In the Piecewise Linear Interface Calculation (PLIC) method proposed by DeBar [54] and Youngs

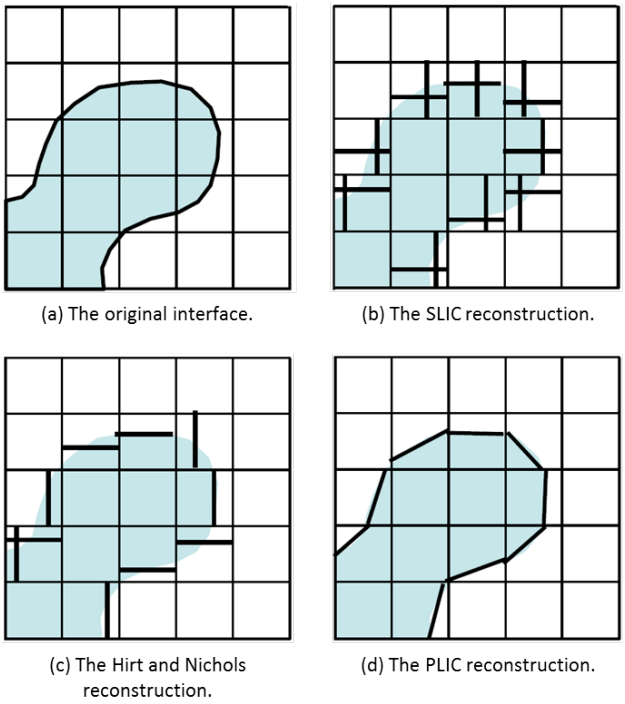

Figure 1.13: VOF reconstruction of the solution for advection in two-dimensions [47].

[58], the interface is always approximated by a straight line segment in each cell, but the line can have an arbitrary orientation. The orientation of the line is a function of the normal to the interface, which is achieved by considering the average value of ϕ in both the cell under consideration and in the neighboring cells. The success of the interface advection depends both on the accuracy of the interface reconstruction as well as by the determination of the normal to the interface. Several methods have been proposed to performed this task, which generally exploit ϕ distribution in the computational domain.

Figure 1.13, shows the main difference between the interface reconstruction using SLIC, the Hirt and Nichols VOF method, and PLIC. The latter method has several advantages: fluid properties can be allocated more accurately, and so can the interface area, enabling a more realistic implementation of surface tension and interfacial transfer models. In the meantime, new reconstruction algorithms have appeared recently using splines and quadratics [59].

In ANSYS Fluent several reconstruction based schemes are available, which are based on the Donor-Acceptor and Geo-Reconstruct methods. The latter represents the interface between fluids using a piecewise-linear approach (PLIC).

The surface tension force introduced by Equation 1.17 is not yet addressed. Surface tension arises as a result of attractive forces between molecules in a fluid. A liquid molecule is surrounded by many other ones and away from the interface the forces which act on it are uniform in all directions. However, a molecule on the interface experiences only half of these forces, producing a resultant force pulling inward. This force opposes any increase in the area of the interface [60]. In order to produce such an increase, a certain amount of work, proportional to the area increase, needs to be done. The surface tension coefficient σ is defined as the amount of work necessary to create a unit area of free surface. It always exists for any pair of fluids, and its magnitude is determined by the nature of the fluids. An important aspect of surface tension is that it creates a pressure jump ΔP across a curved surface [60]. This produces the equilibrium which has been referred to during the derivation of the momentum equation. The Young-Laplace equation relates the ΔP between the two phase and the curvature of the surface:

$$\Delta P = \sigma \left(\frac{1}{R_1} + \frac{1}{R_2} \right) = \sigma \kappa \tag{1.26}$$

where R_1 and R_2 are the principal radii of curvature; ΔP is also called Laplace pressure [61].

The surface tension force can be modelled using the Continuum Surface

Force (CSF) model, proposed by Brackbill et al. [62], which considers in VOF calculations the surface tension such as a source term in the momentum equation. The gradient of ϕ gives the vector normal to each of these layers:

$$\mathbf{n} = \nabla\phi \tag{1.27}$$

Thus, $\nabla\phi$ is a continuous function which is zero everywhere in the flow domain except at the interface. The curvature of such a front may therefore be expressed in terms of the divergence of the unit normal vector to the interface, as follows:

$$\kappa = \nabla \cdot \left(\frac{\nabla\phi}{|\nabla\phi|} \right) \tag{1.28}$$

Therefore, the surface tension force, given by Equation 1.17, can be expressed as a function of only σ and ϕ:

$$f_\sigma = \sigma \left[\nabla \cdot \left(\frac{\nabla\phi}{|\nabla\phi|} \right) \right] \nabla\phi \tag{1.29}$$

It should be highlighted that the CSF method has the propensity to generate "spurious currents" near the interface in the case of surface tension-dominant flows.

The most frequent fluid flow scenario is the turbulent one, which is irregular in space and time and is characterized by a high level of fluctuating vorticity. Two major approaches exist for studying the turbulent flows. In the first, the modelling approach, the flow is described via statistical averaging using the "Reynolds or Favre averaging concept", leading to the Reynolds Averaged Navier-Stokes equations (RANS). The other approach refers to turbulence simulation, in which most or all of the flow structures are resolved "directly". Direct Numerical Simulation (DNS) and Large Eddy Simulation (LES) permit to clearly distinguish the influence of eddies of different scales. While DNS calculates the entire hierarchy of turbulent scales, in LES only a large part of the scale spectrum is directly computed, as in DNS, whereas the sub-scales are modelled [63].

In this work the turbulence has been treated exploiting the RANS

approach. In turbulent flows, the field properties become random functions of space and time. Hence, the field variables u_i, and p must be expressed as the sum of mean and fluctuating parts as

$$u_i = U_i + {u_i}', \quad p = P + p' \tag{1.30}$$

where the main and fluctuating parts satisfy

$$\overline{u_i} = U_i, \quad \overline{u_i'} = 0 \tag{1.31}$$

$$\overline{p} = P, \quad \overline{p'} = 0 \tag{1.32}$$

where the over-bar denotes the time average. By inserting the turbulent variable, Equation 1.30, into Equations 1.14 and 1.15, and taking the time average, the Reynolds Averaged Navier-Stokes equations are obtained:

$$\frac{\partial U_i}{\partial x_i} = 0 \tag{1.33}$$

$$\rho\frac{\partial U_i}{\partial t} + \rho\frac{\partial U_i U_j}{\partial x_j} = -\frac{\partial P}{\partial x_i} + \frac{\partial}{\partial x_j}(2\mu S_{ij} - \rho\overline{u_i' u_j'}) + \mathbf{f} + \mathbf{f}_\sigma \delta_S \tag{1.34}$$

where S_{ij} is the mean strain-rate tensor

$$S_{ij} = \frac{1}{2}\left(\frac{\partial U_i}{\partial x_j} + \frac{\partial U_j}{\partial x_i}\right) \tag{1.35}$$

The quantity $\tau_{ij} = \overline{u_i' u_j'}$ is known as the Reynolds stress tensor, which has to be appropriately modelled.

As regard to the indicator function equation, it has to transport the volume fraction in the domain avoiding its diffusion, therefore the instantaneous value of volume fraction is replaced by the mean value Φ without the introduction of a fluctuating term. Consequently, the RANS equation for the volume fraction is given by

$$\frac{\partial \Phi}{\partial t} + \frac{\partial}{\partial x_j}(\Phi U_i) = 0 \tag{1.36}$$

In "one-fluid" formulation, as for velocity and pressure field, the turbulent variables, e.g. k and ϵ or the Reynolds stresses, are shared

by the phases throughout the field, therefore a single set of transport equations is solved. The turbulence model adopted in the VOF simulations performed in this thesis were the the conventional eddy viscosity models. See the books by Wilcox [64], Pope [65], Versteeg and Malalasekera [66] for an extensive review on the turbulence simulation and modelling.

Chapter 2

Numerical investigation of windage losses

In this chapter, a comprehensive numerical study about the windage losses of a single spur gear rotating in air has been performed by means of ANSYS FLUENT, in order to improve the physical understanding of such loss, defining a numerical setup to be used for the prediction during design phases.

The experiment of Diab et al. [13] has been computationally replicated. Steady state RANS calculations in the rotating frame of reference have been performed with conventional eddy viscosity models. The numerical results have been compared with experimental data from the open literature. The resulting numerical setup has been adopted to simulate a single gear enclosed within cylindrical casings, to assess the effect of the boundary walls on the power losses.

Finally, in the light of the relationship between the windage power losses and the volume of fluid within the system, that has been observed in the enclosed geometries, the Diab's correlation has been revised by introducing an appropriate parameter for include the effects of a casing on windage power losses.

2.1 Test case description

The test rig used by Diab et al. [13], shown in Fig. 1, consists of an electric motor which drives a shaft on two high-precision preloaded ceramic ball bearings via a friction wheel. The test gear is mounted

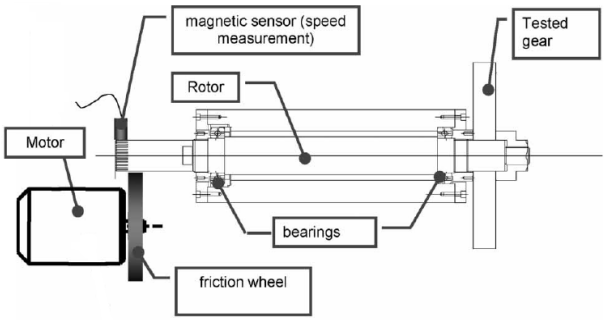

Figure 2.1: Diab test rig [13].

at one free-end of the shaft, and the other free-end is used for speed measurements by means of axial slots. Once maximum speed is reached, the gear system is disconnected from the power supply using a pneumatic jack which removes the motor-friction wheel assembly. Speed is measured by a magnetic probe which counts the impulses generated by the rotation of the slots. In order to isolate the windage net contributions, the power loss with no gear was subtracted from the total system loss [13].

	Pitch diameter $[mm]$	Tooth width $[mm]$	Module $[mm]$	Teeth
Gear 1	288	30	4	72
Gear 2	144	30	4	36
Gear 3	144	60	4	36
Gear 4	300	60	6	24

Table 2.1: Diab experiment: spur gear data

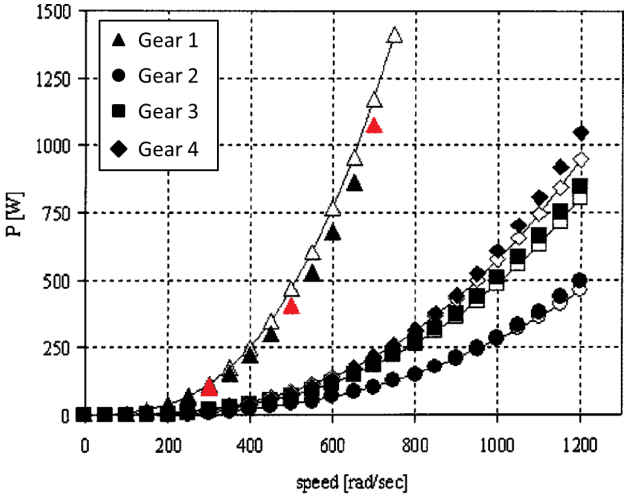

Figure 2.2: Diab test rig results [13].

Four different spur gears and one disk were tested. The gears varied in diameter, width, and module, as summarized in Table 2.1. In Figure 2.2 the experimental measures for the 4 gears are reported.

In this work the Gear 1 has been numerically reproduced, comparing the simulation results with the experimental measurements at 3 speed of rotations: 300, 500 and 700 rad/s (coloured in red in Figure 2.2). This gear was selected because it was tested up to a pitch line velocity of 100 m/s.

2.1.1 Diab Correlations

The formula presented by Diab et al. [13] calculated power loss in Watt as a function of fluid density ρ (kg/m^3), rotation rate ω (rad/s), pitch radius R (m) and a total windage loss coefficient C_t:

$$P = \frac{1}{2} C_t \rho \omega^3 R^5 \tag{2.1}$$

where two different formulas were provided to calculate C_t.

The first formula was based on a dimensional analysis (referred to as Diab-DA):

$$C_t = \eta Re^{\beta} \left(\frac{b}{R}\right)^{\gamma} Z^{\delta} \left\{ \left(\frac{h_1}{R}\right)^{\psi} + \left(\frac{h_2}{R}\right)^{\psi} \right\} \tag{2.2}$$

where R, b, and Z are the geometrical gear parameters pitch radius, width, and number of teeth, respectively. η, β, γ, δ, and ψ are constant coefficients that are derived experimentally (see Table 2.2). The parameters h_1 and h_2 are used to account for the presence of flanges near the teeth. When there is no obstacle on the side of the gear $h_1 = h_2 = 0.5^{1/\psi} R$.

Coefficient	Value
η	60
β	-0.25
γ	0.8
δ	-0.4
ψ	0.56

Table 2.2: Coefficients of the dimensional analysis formulation.

The second approach, referred to as Diab-FA, was based on a fluid flow analysis. As reported in Equation 2.3, the power loss coefficient C_t was subdivided into the windage loss from the front and rear faces of the gear (or disk) and the windage loss due to the teeth, defining the C_f and C_l parameters, respectively.

$$C_t = C_f + C_l \tag{2.3}$$

The gear face contribution is given by Equation 2.4:

$$C_f = \frac{2n_1\pi}{5-2m_1} \frac{1}{Re^{*m_1}} \left(\frac{R^*}{R}\right)^5 + \frac{2n_2\pi}{5-2m_2} \left[\frac{1}{Re^{m_2}} - \frac{1}{Re^{*m_2}} \left(\frac{R^*}{R}\right)^5 \right] \tag{2.4}$$

where n_1, m_1 and n_2, m_2 are coefficients for laminar and turbulent flows, respectively, which values are reported in Table 2.3. Re^* is the critical

Reynolds number between laminar and turbulent flow (it is fixed to $3 \cdot 10^5$), R is the pitch radius and $R^* = \sqrt{\mu Re^* / \rho\omega}$ is the critical radius separating the laminar and turbulent regions.

Coefficient	Value
n_1	1.293
m_1	0.5
n_2	0.072
m_2	0.2

Table 2.3: Coefficients of the fluid flow analysis formulation.

The tooth coefficient is given by Equation 2.5:

$$C_l = \xi \frac{Z}{4} \left(\frac{b}{R} \right) \left[1 + \frac{2(1 + X_A)}{Z} \right]^4 (1 - cos\theta)(1 + cos\theta)^3 \tag{2.5}$$

where X_A is the profile shift coefficient, ζ_p and ζ_a are the pressure angle at pitch point and at tooth tip, respectively, whereas the angle θ is given by the formula

$$\theta = \frac{\pi}{Z} - 2(inv\zeta_p - inv\zeta_a) \tag{2.6}$$

where $inv\zeta$ is known as involute function, and it is expresses by Equation 2.7.

$$inv\zeta = tan\zeta - \zeta \tag{2.7}$$

The contributions of deflectors or flanges are introduced via the reduction factor $\xi = \xi_1 + \xi_2$ which represents the influence of obstacles on the fluid aspiration by the teeth, where ξ_1 accounts for an obstacle on one side of the gear and ξ_2 for the other side; both coefficients are defined by Equation 2.8 if there are deflectors or flanges, or $\xi_{1,2} = 0.5$ otherwise.

$$\xi_{1,2} = \left(\frac{h}{R} \right)^{0.56} \tag{2.8}$$

The formulation assumes that the gas flow on one tooth is deflected by the preceding tooth (in the sense of the rotation), such that the active tooth surface is approximately limited by a line from the tooth profile to

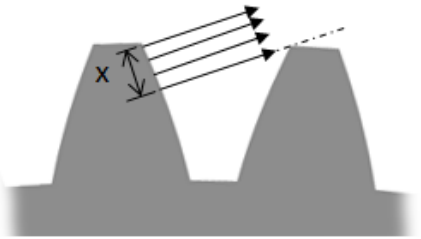

Figure 2.3: Active surface of the teeth considered in the definition of the tooth coefficient [13].

the tip corner of the preceding tooth, as depicted in Figure 2.3.

2.2 Numerical model

Similarly to Marchesse et al. [24], for all simulation presented in this work, the equations are solved according to a rotating reference frame and under steady state conditions. Using this approach, the solver computes the appropriate Coriolis and centrifugal momentum terms.

2.2.1 Computational domain and boundary conditions

Some geometric simplifications have been adopted in the simulations. Despite of the cantilever shaft, it was considered the model as symmetric, in order to reduce the volume of the domain and therefore the amount of cells. Thus, a symmetry condition was imposed to the surface pointed in Figure 2.4.

Furthermore, only one tooth passage instead of the entire set has been discretized by exploiting periodic boundary conditions. After these simplifications, the model appears as shown in Figure 2.4. As the equations are solved in rotating frame, a zero speed in the rotating frame is set for nodes located in gear surfaces and shaft. Periodic and symmetric conditions are applied to the planar surfaces pointed in Figure 2.4, while outlet vent boundary condition [67] is applied to those surfaces suggested

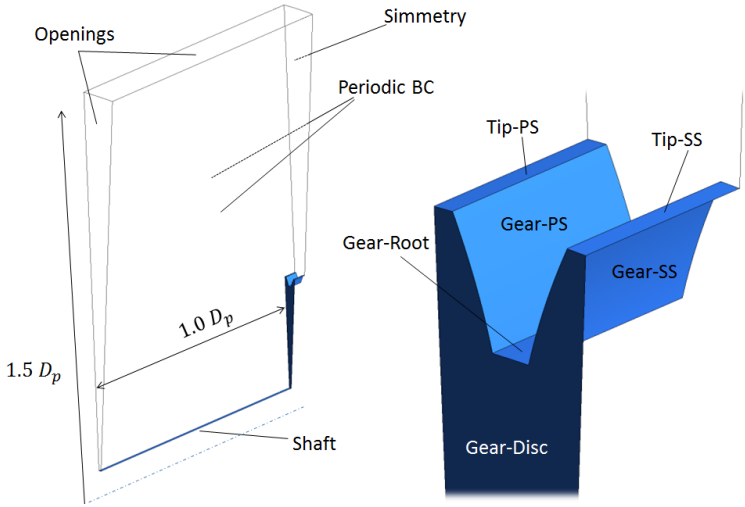

Figure 2.4: Computational domain

as "Openings".

2.2.2 Numerical setup and grids

ANSYS Fluent v.16 has been used to solve the 3D RANS equations. The air was treated as isothermal (air properties are evaluated at 25°C) and incompressible (Mach number < 0.3). The pressure-based Coupled solver with Pseudo Transient option was selected as velocity-pressure coupling algorithm. The pressure field was discretized using Body Force Weighted scheme, recommended when body forces are large as in highly swirling flows [67], whereas a second order upwind scheme was used for the discretization of the velocity field.

Three eddy viscosity models have been selected in this study to model turbulence: standard $k-\epsilon$, RNG $k-\epsilon$ [68] and shear stress transport (SST) $k-\omega$ [69] models. As regards to the near wall treatment, low-Reynold formulation has been adopted for $k-\omega$ SST model, while for the

$k-\epsilon$ models scalable wall functions have been used. The simulations were stopped when the scaled residuals had reached a minimum of $5.5 \cdot 10^{-5}$ for every equation.

Mesh ID	Nodes number $[k]$	Windage Power loss $[W]$
1	298	1126
2	698	1108
3	1014	1097

Table 2.4: Results of mesh sensitivity.

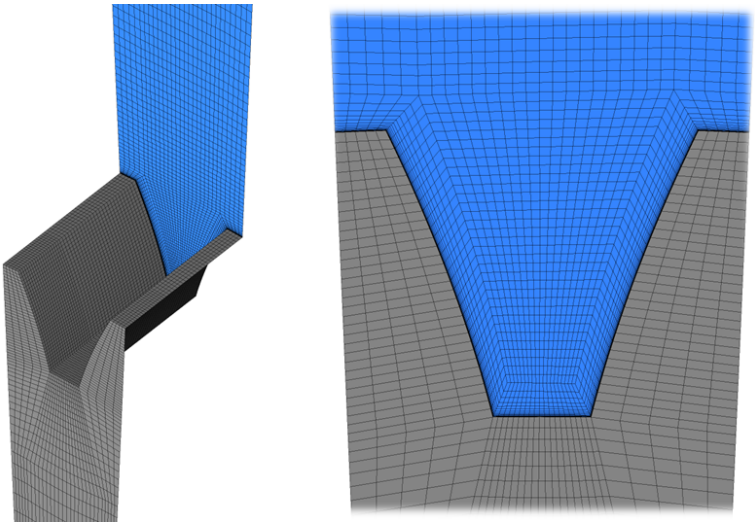

Figure 2.5: Computational grid

ANSYS ICEM-CFD has been used to generate three hexahedral meshes, having an increasing number of elements. A mesh sensitivity study was performed, comparing the windage power losses produced at a rotating speed of 700 rad/s; the grid dimensions and the results are summarized in Table 2.4. Passing from the coarser grid to the medium

size grid, the windage power loss reduces of 1.6 %, whereas a further increase of nodes number (Mesh 3) leads only to a reduction of 1% of the power loss. On the basis of the mesh sensitivity analysis, the medium size grid has been selected for the present work. A picture of the mesh is shown in Figure 2.5.

2.3 Results

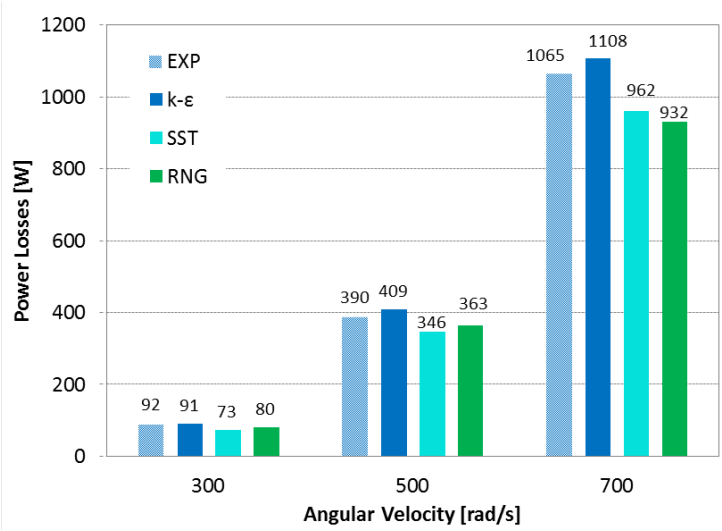

Figure 2.6: Windage power losses: comparisons between CFD and experimental results.

In Figure 2.6 the computational results are compared with the experimental data. CFD analyses exhibit very good agreement with experiment for all of the speed of rotations, especially the predictions obtained with $k-\epsilon$ model are very close to the measurements, with relative error that never exceeds 5 percent. The RNG $k-\epsilon$ and $k-\omega$ SST models have a tendency to underestimate windage power losses, in particular at lower

speeds; however as the speed increases, the underestimation of the SST model decreases.

In Figure 2.7 the total power losses are broken down into viscous and pressure contributions, for all the turbulence models tested. The main difference among the results is in the calculation of pressure force contribution; in fact, as visible in the picture, the power losses related to the shear forces is about the same for every turbulence model (dashed lines).

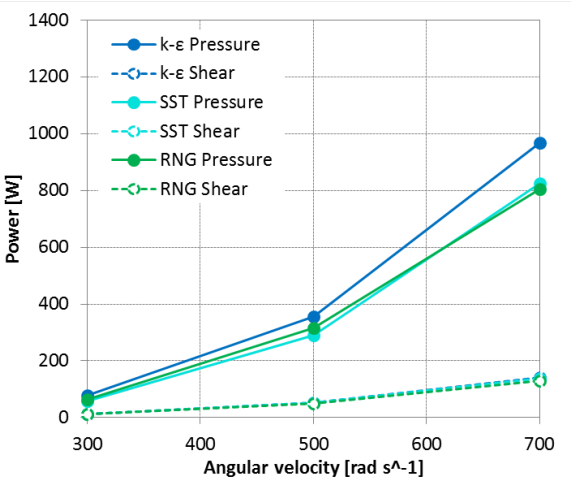

Figure 2.7: Subdivision of windage power losses into pressure and viscous contributions for each turbulence model tested.

Focusing on the standard $k - \epsilon$ model outcomes, in Figure 2.8 the total losses are subdivided into viscous and pressure contributions. The results show how the pressure is the dominant factor for the windage losses, while the shear force contribution stands at 14 % and it slightly decreases when the speed of rotation increases.

Concerning the correlative approach developed by Diab et al. and presented in section 2.1.1, in Figure 2.9 both formulations (Diab-DA and Diab-FA) are compared to the experimental data. A rather good

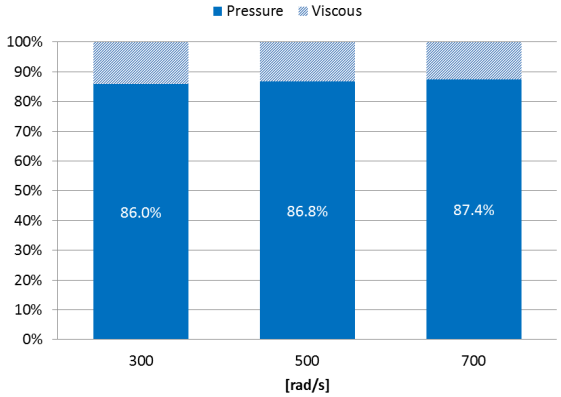

Figure 2.8: $k - \epsilon$ results: subdivision of windage power losses into pressure and viscous contributions.

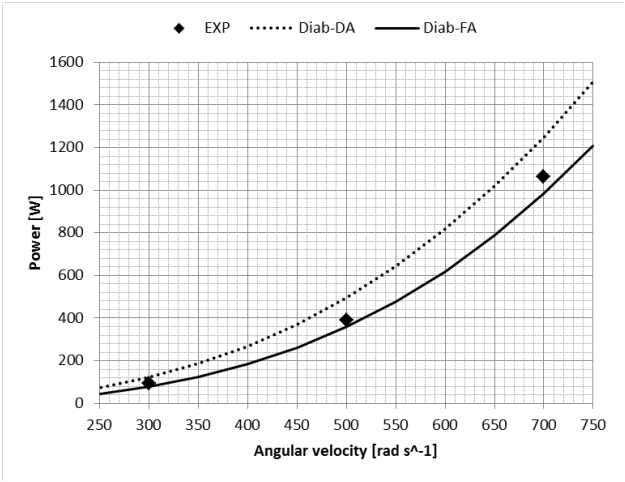

Figure 2.9: Comparisons between the experimental results and the Diab's correlations.

agreement with the measurements is revealed, especially for the Diab-FA. The Diab-DA correlation shows a tendency to overestimate the power loss, on the contrary the Diab-FA is tending to underestimate. In more details, a comparison between the correlations and the measurements are shown in Figure 2.10 in terms of percentage difference; also the CFD results are reported. Diab-DA formulation overestimates the power of 32 % at 300 rad/s, stands to 27 % at 500 rad/s and then reaches 17 % at the maximum tested speed. Diab-FA correlation underestimates the power

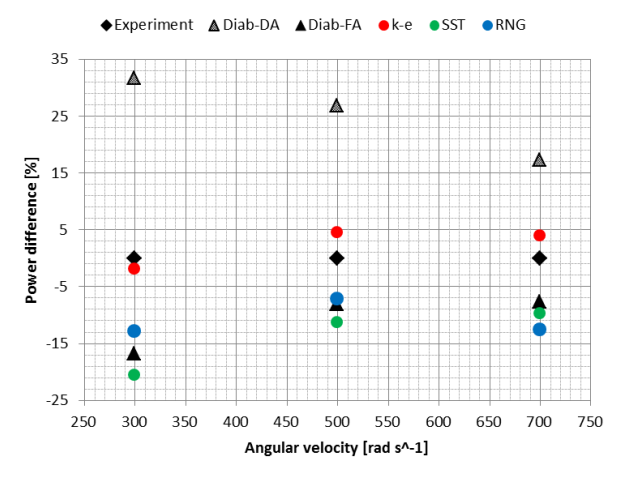

Figure 2.10: Comparisons among experimental measurements, Diab's correlations and CFD results: percentage power difference.

losses of 17 %, 8 % and 7.6 % at the minimum, middle and maximum speeds, respectively.

In conclusion, the Diab-FA has proved to be more accurate than the Diab-DA formulation, by providing differences with the experimental data lower than 10 % when the pitch line velocity exceeds 70 m/s ($\omega > 500 rad/s$). In addition, as suggested by Diab et al. [13], it is believed that the formula from the fluid flow analysis provides more insight into the physical phenomena and should be more versatile than that one coming

from dimensional analysis.

2.3.1 Details of the flow field

To analyse flow and pressure fields generated by the gear motion, the achievements of the simulation adopting the $k - \epsilon$ turbulence model are considered; the results concern the run at the rotating speed of 700 rad/s.

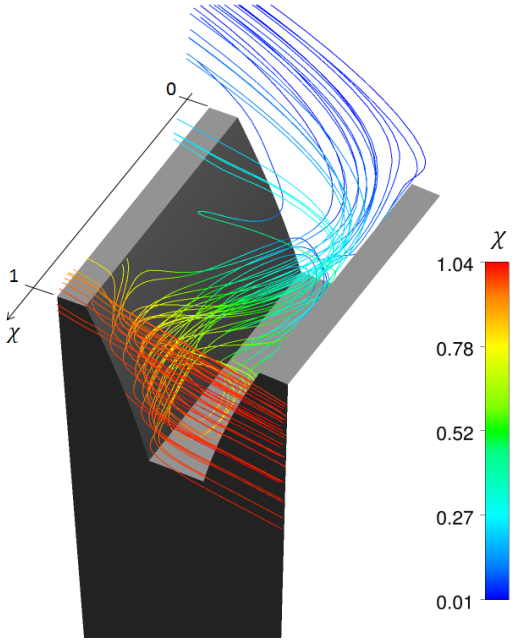

Figure 2.11: Three-dimensional relative frame streamlines colored by χ coefficient.

In Figure 2.11, three-dimensional relative frame streamlines coloured by χ coefficient are reported. χ is a dimensionless axial coordinate defined equal to zero at the symmetry plane position and 1.0 at the end of the tooth surface (see Figure 2.11). With reference to the nomenclature in

Figure 2.4, the air close to the gear teeth impinges on the Gear-PS surface, as a result of the low pressure region located in the tooth space (see Figure 2.12) that draws fluid into the tooth. Therefore, the fluid is diverted into the tooth passage and moves both axially toward the gear centreline and toward the Gear-SS surface. Due to symmetry, this axial transport arises on both sides of the gear and leads to impingement of oppositely directed flows at regions with χ approaching to zero value. After that, the air is ejected radially from the tooth space.

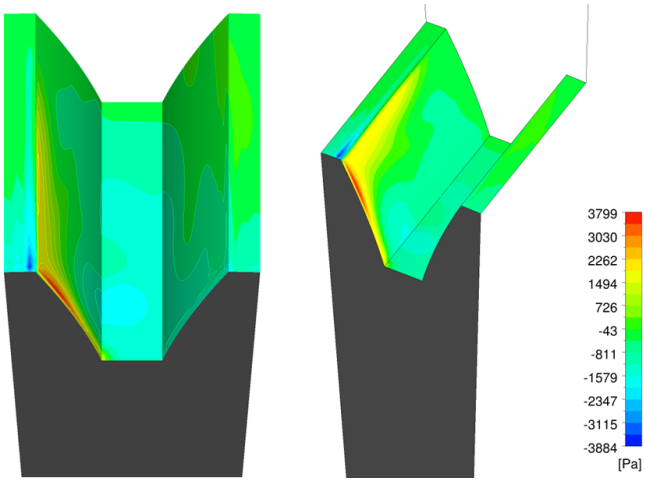

Figure 2.12: Contour plot of relative pressure on the tooth surface.

In Figure 2.12 the static pressure contour is plotted on the gear tooth surface. The Gear-PS surface is characterized by the overpressure region, due to the air flow impingement, while the Gear-SS, Tip-PS, Tip-SS and Gear-Root have negative pressure values. Only the pressure distributions on the Gear-PS and Gear-SS surfaces contribute to the net axial torque. The maximum and minimum pressure values are located at the periphery of the gear where speeds are greatest, so their contribution to the power loss is significant ($Power = Torque \cdot \omega = Force \cdot r \cdot \omega$).

To analyse in more details the phenomenon, in Figure 2.13 the contour

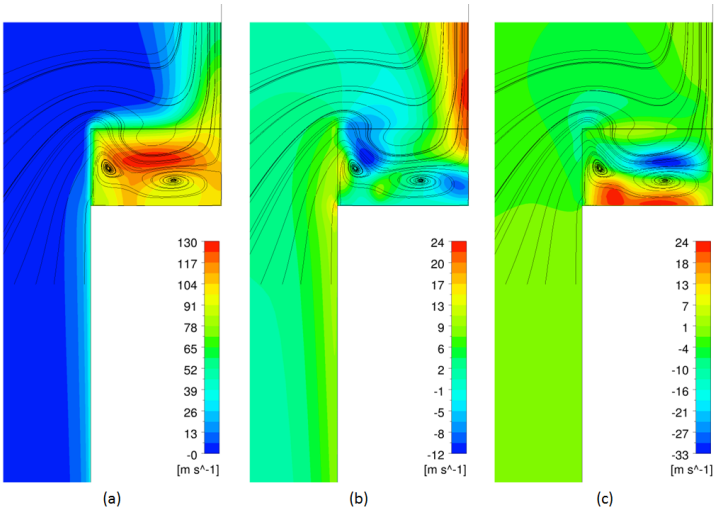

Figure 2.13: Contours plot on the symmetry plane of: a) Tangential Velocity in stationary frame, b) Radial Velocity, c) Axial Velocity.

plots of absolute tangential velocity, radial velocity and axial velocity on the symmetry plane are shown; the streamlines over this plane are reported for easing flow visualization. The pictures show how the flow field is strongly three-dimensional. The air diverted into the tooth passage immediately gains a high tangential velocity, reaching the gear peripheral speed, then accelerates into the tooth toward the bottom of the Gear-SS surface due to the depression located in such a region. The air flow reaches a maximum axial velocity of 33 m/s, then exits from the tooth with radial and tangential velocity components of about 24 and 104 m/s respectively. The streamlines show how the tooth bottom is home to a clockwise rotating vortex that extends over the entire depression region; this vortex is powered by the high speed air flow drawn in by the tooth.

Furthermore, in Figure 2.13-b, it can be observed that the air near the tooth is drawn into it also from a region with negative radial velocity set close to the gear top land, where χ tends to 1.

2.4 Enclosed gear

As mentioned in section 1.1.1, several researchers have shown reductions in gear windage loss when shrouds of various configurations are employed.

The gear previously studied has been enclosed within cylindrical casing, studying how the flow field and hence the power losses change with the casing dimensions. Seven configurations have been examined, which dimensions are quantified and illustrated in Table 2.5 and Figure 2.14, respectively.

Casing ID	δ_{axial} [−]	δ_{radial} [−]	Fluid Volume [−]
0	1.000	1.000	1.000
1	0.500	0.239	0.125
2	0.235	0.239	0.062
3	0.500	0.032	0.062
4	0.103	0.239	0.031
5	0.032	0.032	0.005
6	0.014	0.014	0.002

Table 2.5: Characteristic dimensions of the tested casings.

The geometries are characterized by two parameters, the axial gap between the Gear-disc surface and the enclosure (δ_{axial}), and the radial gap between the gear top land and the cylindrical surface of the casing (δ_{radial}). The enclosure of greatest dimension, Casing-0, has axial and radial gaps of about the pitch diameter dimension, whereas the smallest geometry has such spaces of the order of magnitude of the teeth module. The dimensions of Casing-0 have been used to normalise every values reported in Table 2.5.

The main idea is to assess a possible relationship between windage power loss and the variation of the enclosed air volume, evaluating whether casings with small dimensions can modify the relative magnitude of the pressure and shear contributions in the loss budget.

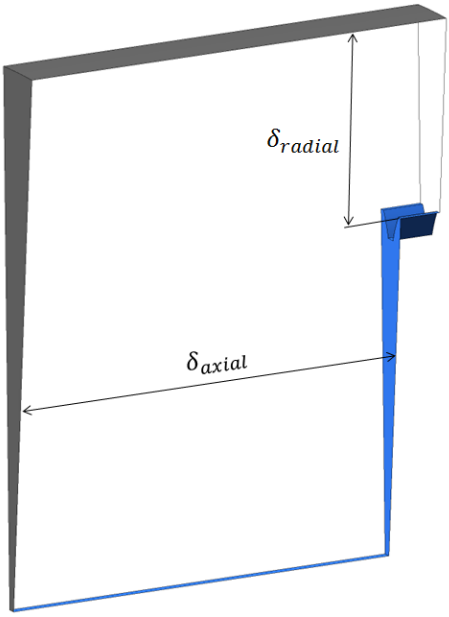

Figure 2.14: Casing geometry.

2.4.1 Numerical setup and grids

In the light of the results shown before, standard $k-\epsilon$ model has been selected to model turbulence, adopting scalable wall functions for the near wall treatment. The numerical set-up is the same of the previous simulations while as regard to the boundary conditions, the outlet vent boundaries have been replaced by counter-rotating rigid walls, because the equations are solved in rotating frame. Three rotating speeds have been analysed, 300, 500 and 700 rad/s, for a total of twenty-one simulations.

For every geometry a hexahedral grid has been generated, whose elements have the same characteristic dimension of the mesh adopted in the simulations discussed before.

2.4.2 Results

In Figure 2.15 and 2.16 the contour plot of absolute tangential velocity on the symmetry plane for free and enclosed geometries are reported. These results are relative to the rotating speed of 700 rad/s.

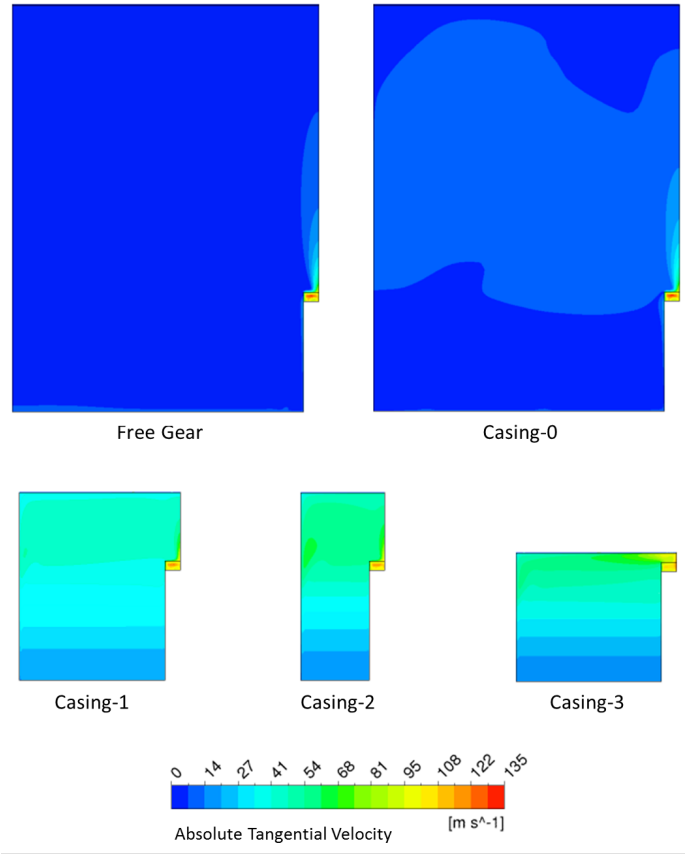

Figure 2.15: Contour plot of absolute tangential velocity on the symmetry plane for free and configurations named Casing-0,1,2,3. Speed of rotation, 700 rad/s.

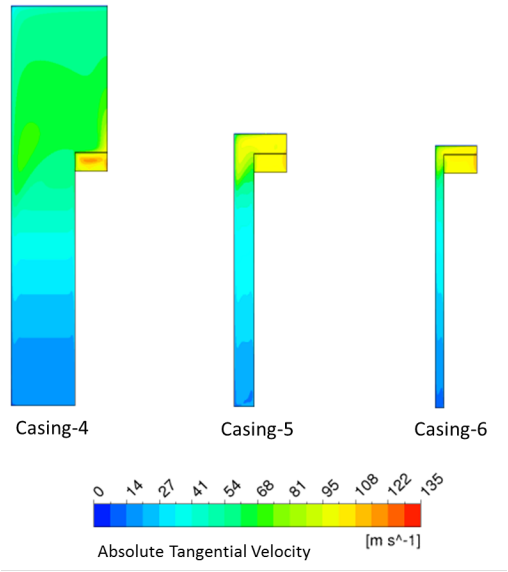

Figure 2.16: Contour plot of absolute tangential velocity on the symmetry plane for configurations named Casing-4,5,6. Speed of rotation, 700 rad/s.

The air is drawn into the tooth passage because of the low pressure within it; this flow impinges on tooth surface that transfers momentum to the air. In the configuration without enclosure, such process always acts on 'new' fluid that is expelled from the tooth passage with high velocity moving away. Instead, in the enclosed configurations, the casing keeps the fluid near to the tooth surfaces, confining the angular momentum imparted by the gear tooth. In this way, the fluid progressively gains angular momentum, increasing its tangential velocity as long as a stationary condition is achieved. By reducing the casing dimensions, the volume of air within the system decreases and the fluid reaches a higher average tangential velocity.

To further analyse the phenomenon, in Figures 2.17, 2.18 and 2.19,

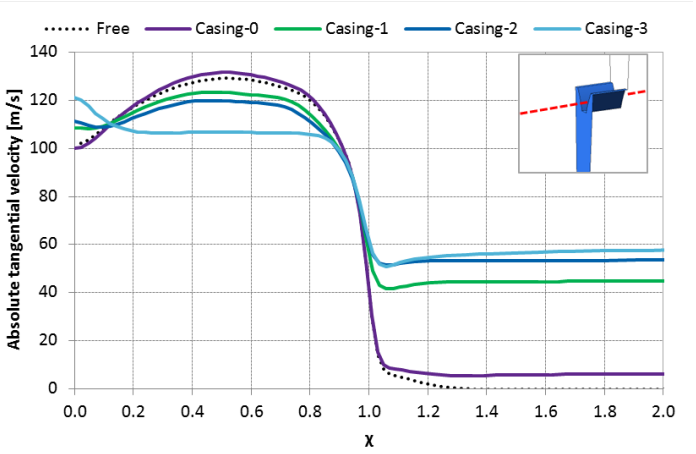

Figure 2.17: Absolute tangential velocity values along the red dashed line for free and configurations named Casing-0,1,2,3, at 700 rad/s.

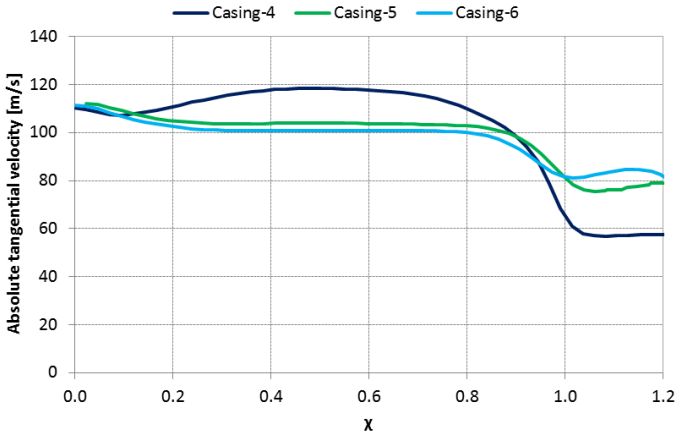

Figure 2.18: Absolute tangential velocity values along the red dashed line for configurations named Casing-4,5,6, at 700 rad/s.

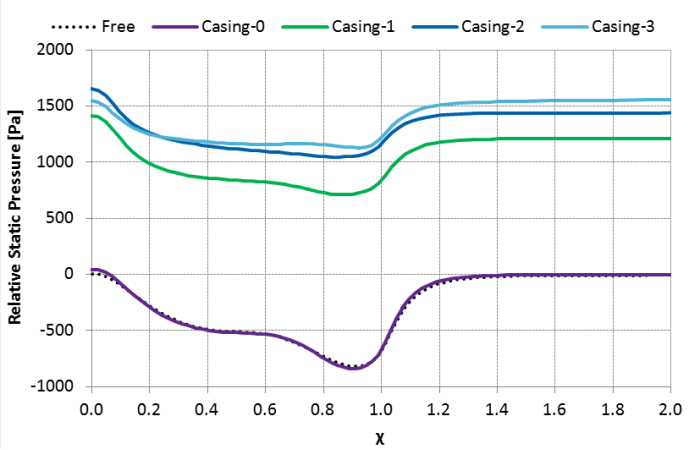

Figure 2.19: Relative pressure values along the red dashed line for free and configurations named Casing-0,1,2,3, at 700 rad/s.

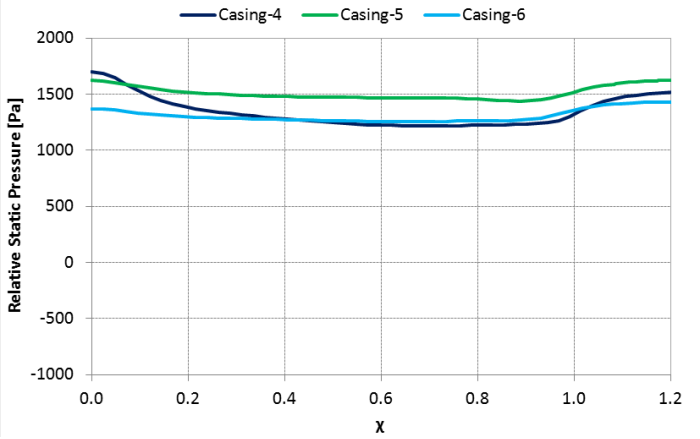

Figure 2.20: Relative pressure values along the red dashed line for configurations named Casing-4,5,6, at 700 rad/s.

2.20 the values of absolute tangential velocity and relative pressure along the red dashed line are shown, respectively. Such line, drawn at the right corner in the Figure 2.17, is parallel to the rotational axis and it is located on the symmetry plane at a diameter equivalent to the pitch circle.

As the fluid approaches the gear tooth ($\chi = 1$), it is abruptly accelerated to the local tangential velocity of the gear. In both enclosed and free cases, the flow is accelerated to the same tangential velocity upon entering the tooth space, but the enclosed geometries experiencing a significantly smaller change in velocity. Because of the rotating flow field formed in the system, a centripetal pressure gradient occurs for balancing the centrifugal forces due to the circumferential motion. The pressure gradient increases as the tangential velocity of fluid grows up, and that is when the casing's dimension decreases, as visible in Figures 2.19 and 2.20. The pressure increase acts on the entire system, in fact, it can be noticed how in the casings characterised by axial and radial gaps comparable to the tooth height (Casing-5 and 6), the pressure level within and outside of teeth is almost the same.

This also affects the intensity of the air acceleration within the tooth (χ between 0 and 1), in fact, when the system volume decreases, the centripetal pressure gradient reduces the depression located in the bottom of the Gear-SS surface, which results in an air tangential velocity reduction, as shown in Figures 2.17 and 2.18.

The casing dimensions impact directly on windage power loss. As said before, by conserving the angular momentum of the flow near the teeth, the fluid progressively gains momentum, leading to a rotating flow field within the system. This generates a centripetal pressure gradient that reduces the depression in the tooth space. As a result, the power required of the gear to accelerate the flow decreases. The increase of the centripetal pressure gradient continues as long as a stationary condition is achieved.

In Figure 2.21 the percentage of power losses reduction with respect to the free configuration are reported; every value related to a particular rotating speed has been made dimensionless using the power loss of the

free configuration at that speed of rotation. The bar chart shows how, when the casing dimensions decrease, the percentage reduction of the power losses whit respect to the free case is not sensibly affected by the speed of rotation and it is depend just to the casing dimensions.

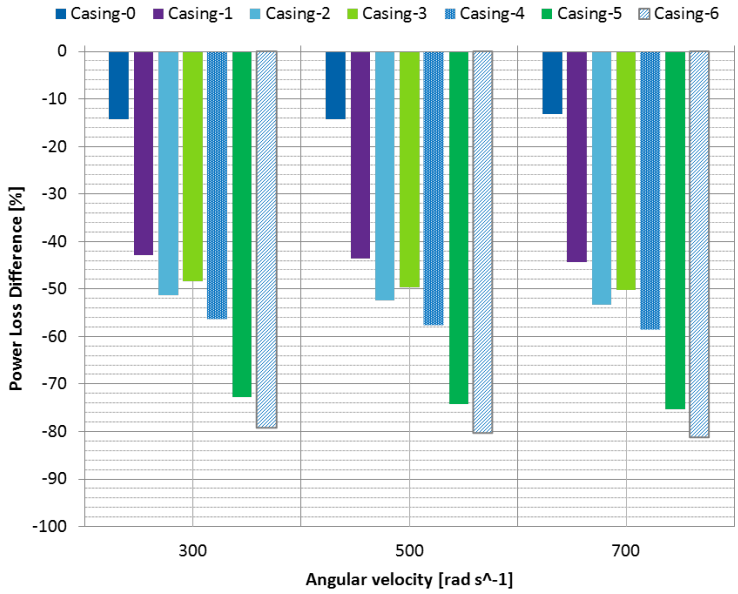

Figure 2.21: Percentage reduction of windage power losses as function both of casing dimensions and rotating speed.

Therefore, only the results related to the maximum speed of rotations can be considered to comment on results. To compare the power reduction with the fluid volume trend, in Figure 2.22 both the normalized power losses and the normalized fluid volume are plotted, where the former has been normalised by power loss of the free gear configuration at 700 rad/s and the latter by the volume of the Casing-0.

In Figure 2.21, it can be seen a reduction of about 15 % passing from the free gear case to the enclosed configuration named Casing-0. In this

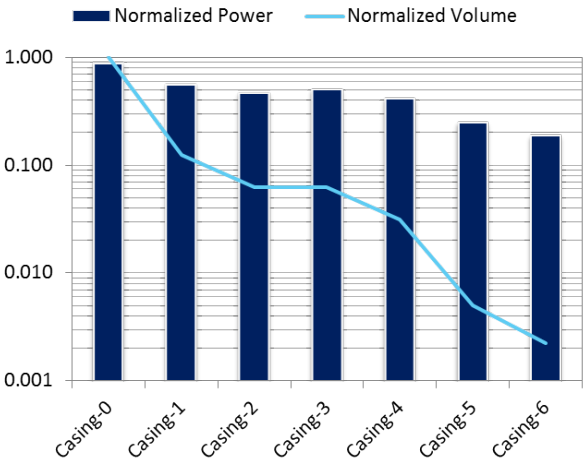

Figure 2.22: Bar chart of the normalized power losses at 700 rad/s compared to the trend of the normalized air volume contained in the system.

case, the volume of air contained in the system is a big amount with respect to the gear dimension, thus the effect of the casing walls on the windage losses reduction is limited. By reducing fluid volume of about 8 times, Casing-1, the power decreases of 44 % compared to the free gear value. By decreasing the volume by one-half compared to the Casing-1, the power loss further reduces of 53 % and 50 % in the Casing-2 and Casing-3, respectively. These geometries indeed, enclose the same fluid volume, but differ in the axial and radial dimensions. In relation to the Casing-1, the Casing-2 is characterized by the same axial gap, but a smaller gap between the gear top land diameter and the casing, whereas in the Casing-3, the axial gap has been reduced of 47 % and the radial one remains the same of the Casing-0. The simulations show that, for the same fluid volume, a reduction of the axial gap in the casing has slightly more effect on the power loss with respect to a radial gap reduction.

In the Casing-4, the fluid volume is a quarter of that in the Casing-1;

in this geometry a further reduction of the axial gap with respect to the Casing-3 has been carried out. The calculated power loss is about 60 % of the value achieved for the free gear configuration

Finally, in the smallest casing, the windage loss is the 80% of the free configuration in the face of a fluid volume which is the 2 per thousand of the bigger enclosed geometry. This, moreover, is a sign of the non-linear relationship between windage power losses and the casing dimensions.

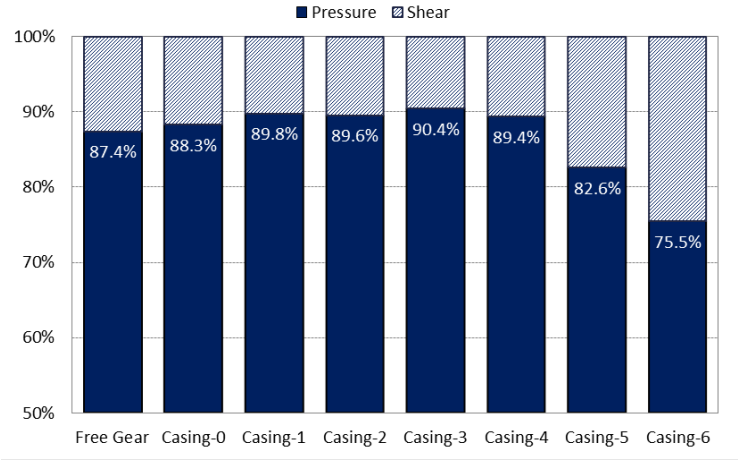

Figure 2.23: Percentage subdivision of windage power losses into pressure and viscous contributions (700rad/s).

In Figure 2.23 the total power losses are broken down into viscous and pressure contributions, for all the tested configurations at 700 rad/s. As shown for the free gear case, the main contribution to the windage power losses is related to the pressure force distribution. In particular, at first, the shear force contribution decreases when the gear is enclosed, to stand at 10 % of the total power loss, then starts to increase when the axial and radial gaps between the gear and the casing become comparable to the tooth height, reaching the 24.5 % of the total power loss when the smaller casing is considered (Casing-6).

To conclude, the air mass flow pumped by the gear has been calculated, to evaluate how this is related to the windage power losses. Results are summarized in Table 2.6, where the normalization was carried out by dividing the mass flow rates by the value obtained in the free configuration.

Configuration	Normalised Mass Flow [−]
Free	1.00
Casing-0	1.08
Casing-1	0.99
Casing-2	1.00
Casing-3	1.18
Casing-4	0.99
Casing-5	0.97
Casing-6	0.77

Table 2.6: Normalised mass flow rate pumped by the teeth.

The air mass flow does not match the power reduction trend which decreases with the fluid volume reduction. On the contrary, in the Casing-0 an increase of 8 % is achieved, then the mass flow rate remains approximately constant in the Casing-1, 2, 4 and 5, while a further increase of 18 % of the pumped air is observed when the Casing-3 is adopted. A valuable reduction is achieved only for the Casing-6, in fact the mass flow rate is 23 % lower then the free case, but it is significantly higher than the corresponding power reduction, which is of the 80 %.

These achievements show that the reduction of windage loss, occurring when the casing dimensions decrease, is not related to the air mass flow rate pumped by the teeth. The latter is rather a consequence of the pressure distribution that develops in the tooth space.

2.4.3 Improvement of Diab correlation

In the light of the relationship between the windage power losses and the volume of fluid within the system, and verified the capability of the

Diab correlations in the calculation of the windage losses relating to a non confined gear, it has been considered to revise such a formulation by introducing an appropriate parameter for include the effects of a casing on the power losses prediction.

Casing ID	$\hat{P_n}$
0	0.861
1	0.564
2	0.477
3	0.506
4	0.424
5	0.259
6	0.196

Table 2.7: Average normalised power loss as function of casing dimensions.

To do that, the power losses reported in the previous section have been processed. Every value related to a particular rotating speed has been made dimensionless using the power loss of the free configuration at that speed of rotation, then, the average normalised value ($\hat{P_n}$) is obtained by carrying out an arithmetic average of the data for the different speeds of rotation, achieving the values presented in Table 2.7.

In Figure 2.24 the scatter diagram of $\hat{P_n}$ is reported as function of the volume ratio coefficient defined by Equation 2.9: this is the ratio between the volume of fluid enclosed between the casing and the rotating parts, namely the gear and the shaft, with the gear volume. In the graph both axes are in logarithmic scale.

$$V_r = \frac{Fluid\,Volume}{Gear\,Volume} \tag{2.9}$$

A regression analysis has been performed, obtaining the trend line described by the power-law in Equation 2.10, where m is the power-law exponent, and n is a constant. The coefficient of determination (R^2) equal to 0.989 highlights a strong positive correlation between the power-law

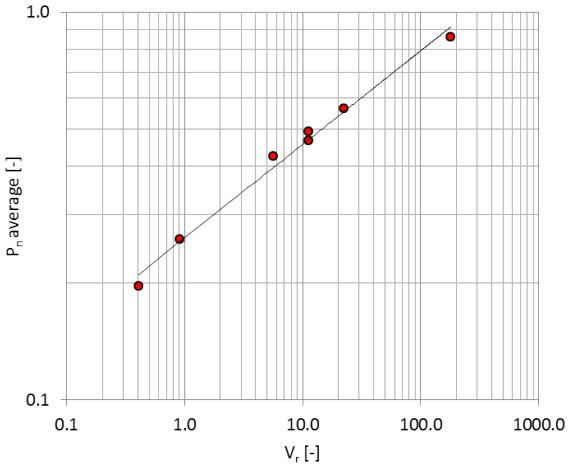

Figure 2.24: Normalized power reduction: averaged values.

and data.

$$C_v = mV_r{}^n \tag{2.10}$$

Equation 2.10 describes the volume correction parameter (C_v) which has to be implemented within Diab's correlation. As a result, the improved Diab formulation, P_{C_v}, to be use for calculating the windage power losses of a spur gear enclosed within a cylindrical casing is described by Equation 2.11, where P_{Diab} is the windage power losses for a non confined gear expressed by Equation 2.1.

$$P_{Cv} = C_v \cdot P_{Diab} \tag{2.11}$$

To conclude, in Figure 2.25 the predictions of Equation 2.11 has been compared with the CFD results obtained for the speed of rotation equal to 700 rad/s. A good agreement between correlation and CFD is displayed. In more detail, the formula has a tendency to underestimate the numerical result, presenting a maximum, minimum and average percentage

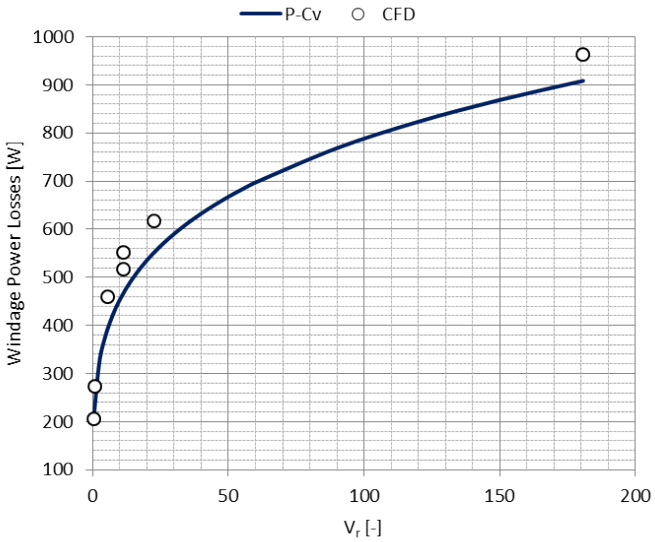

Figure 2.25: Comparisons between Diab-Cv correlation and the CFD results.

underestimation of about 17 , 3 and 10 %, respectively, as summarized in Table 2.8.

Casing ID	Power difference [%]
0	-4.4
1	-11.3
2	-11.1
3	-16.6
4	-15.7
5	-10.3
6	-3.1

Table 2.8: Power difference between modified Diab-Cv correlation and CFD results.

The capability of the improved correlation will be assessed in chapter 4, by a comparison with the experimental measurements performed on the High Speed Test Rig.

2.5 Concluding remarks

In this chapter, numerical investigations about the windage losses have been presented. Firstly, the capability of using a CFD code to calculate windage power losses of a single spur gear rotating in air has been assessed, using ANSYS FLUENT. The experiment of Diab et al. [13] has been computationally replicated. Steady state RANS calculations in the rotating frame of reference have been performed with conventional eddy viscosity models. The numerical results have been compared with experimental data.

The CFD analysis have exhibited a very good agreement with experiment for all of the speed of rotations. Especially the predictions obtained with $k-\epsilon$ model are very close to the measurements, with relative error that never exceeds 5 %. The RNG $k-\epsilon$ and $k-\omega$ SST models have a tendency to underestimate windage power losses, in particular at lower speeds.

The resulting numerical setup has been adopted to simulate a single gear enclosed within seven cylindrical casing having different dimensions, to assess the effect of the boundary walls on the windage power losses. The main conclusions arising from this research are listed below:

- In all the investigated configurations, the pressure field is the dominant factor for the windage losses, whereas the contribution of the shear forces is about of 10 % and it decreases when the speed of rotation increases. However viscous contribution with respect to the pressure one starts to increase, as the axial and radial gaps between the gear and the casing become comparable to the tooth height.

- The windage losses reduce when the gear is enclosed within a casing. This preserves the angular momentum of the flow, so that the fluid progressively gains momentum, leading to a rotating flow field

within the system. This generates a centripetal pressure gradient that reduces the depression in the tooth space. As a result, the power required to accelerate the flow decreases.

- The reduction of windage loss, that occurs when the casing dimensions decrease, is not related to the air mass flow rate pumped by the teeth, but it depends on the volume of fluid enclosed within the casing.

- In the basis of the relationship between the windage power losses and the volume of fluid within the system assessed for the enclosed geometries, the Diab correlation has been revised by introducing an appropriate parameter for include the effects of boundary walls on the power losses prediction. The capability of the improved correlation will be assessed in chapter 4, by a comparison with the experimental measurements performed on the High Speed Test Rig.

Chapter 3

Numerical investigation of oil jet lubrication losses

In this chapter the CFD studies on the oil injection losses are reported. In order to reach a deeper knowledge of this loss, a comprehensive numerical study of a single oil jet impinging radially on a single spur gear has been carried out using the VOF method, within the context of transient RANS calculations. The main objective of this study is to predict the power losses due to the oil jet lubrication, as well as the lubrication performance, whereas the oil recirculation losses are not considered.

The main challenges regarding this analysis are: large three-dimensional domain that leads to high computational cost, two-phase transient simulation, high speed free surface flow, stationary and rotating domains.

The Volume of Fluid method, described by Hirt and Nicholos [50], represents one of the most suitable methods to simulate oil jet impact on the moving gear teeth. This allows one to efficiently track the evolution of the oil surface within the calculation domain, capturing the air-oil interface, as well as the droplets and ligaments formation produced by jet's breakup. However this technique requires a very fine mesh in the liquid region, leading to significant computational costs if a strategy for local grid refinement is not adopted. The solution adaptive mesh

feature implemented in the commercial code ANSYS Fluent [67] has been used. This method provides several automatic criteria to refine and/or coarsen the grid based on geometric and numerical solution data. Hybrid adaptation functions have been created to confine the adaptation to specific domain regions.

In order to carry out a global sensitivity analysis of grid adaptation strategy and model parameters, a simplified geometry has been defined. The resulting numerical set-up has been adopted for the simulation of a reference geometry. Finally, several simulations by varying both oil jet inclination and injection velocity have been performed, in order to evaluate how these parameters affect the resistant torque as well as the lubrication performance.

3.1 Geometry and Operating conditions

3.1.1 Reference geometry

In order to study the forces exchanged between a high speed spur gear and the lubricating jet, a representative geometry was defined (3.1). It consists of a spur gear confined within a symmetrical casing; the entire 360° geometry is modelled. The lubricating jet is introduced by a cylindrical duct set up on the casing surface. The oil is directed towards the rotor axis, impinging on the gear face center. No outlet has been defined because as only few tooth passages were simulated, in fact the lubricant volume injected is negligible with respect to the volume of air in the system.

The geometrical dimensions are summarized in Table 3.1. The defined gaps between transmission and casing are chosen in order to minimize domain volume, maintaining enough space in the radial direction to track the oil breakup during impact.

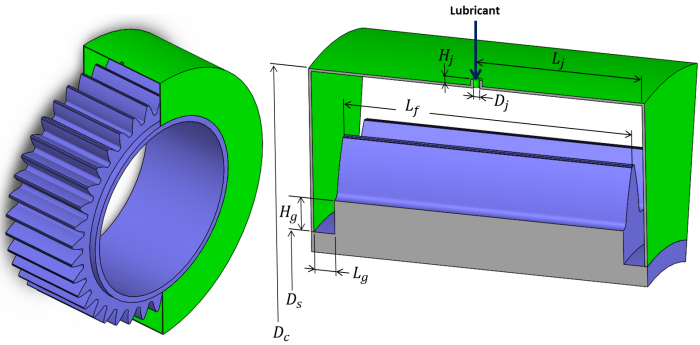

Figure 3.1: Reference geometry.

$\frac{D_p}{D_j}$	$\frac{D_c}{D_j}$	$\frac{D_s}{D_j}$	$\frac{L_f}{D_j}$	$\frac{L_g}{D_j}$	$\frac{L_j}{D_j}$	$\frac{H_g}{D_j}$	$\frac{H_j}{D_j}$	Z
126.7	158.3	105	45.8	3.3	26.3	6.7	1	38

Table 3.1: Dimensionless geometrical parameters.

3.1.2 Theoretical model

The expected average resistance torque produced by the oil jet lubrication can be estimated calculating the oil momentum variation during the interaction with the tooth. Assuming that gear accelerates the oil up to the pitch line velocity, the resistant torque, as function of the oil injection angle, can be calculated as reported in Equations 3.1 and 3.2.

$$F(\alpha) = \dot{m}_j \Delta U_t = \dot{m}_j (U_p - U_j \sin\alpha) \tag{3.1}$$

$$T(\alpha) = \frac{P}{\omega} = \frac{U_p F}{\omega} = \frac{\dot{m}_j U_p (U_p - U_j \sin\alpha)}{\omega} \tag{3.2}$$

The simple model, referred to as 0D-Model, provides a resistant torque equal to T_0 when the oil injection angle is set to a zero value (Equation

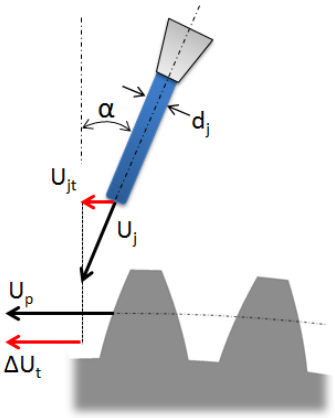

Figure 3.2: 0D-Model's sketch.

3.3).

$$T(0) = T_0 = \dot{m}_j \omega {R_p}^2 \tag{3.3}$$

All torque values reported in this analysis have been made dimensionless using T_0 (Equation 3.3).

3.1.3 Operating conditions

The operating conditions used in the simulations are representative of an aero-engine cruise conditions:

- sub-atmospheric pressure condition,
- temperature was matched with the typical operating value within gearbox systems,
- the ratio between the oil jet and the pitch line velocities was fixed to 0.25.

The choice of such conditions takes effect on the oil jet behaviour. The lubricant has to cross a rotating air flow before to impact on the gear teeth. As it will be shown in section 3.3.1, the airflow is characterized

by a tangential velocity of the same order of the pitch line velocity ($U_{air} \approx 0.9U_p$). To a first approximation, the problem can be treated as

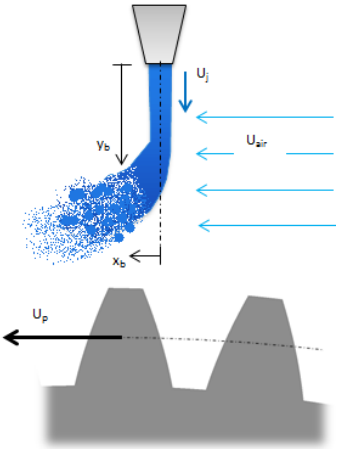

Figure 3.3: Sketch of liquid jet in the air crossflow.

an injection of liquid into a high-speed cross flow (see Figure 3.3). For such issue, a lot of empirical correlations have been developed by many researchers to predict the liquid column trajectory, breakup distance x_b and height y_b, for various flow conditions [70], [71]. The main parameter governing the phenomenon is the liquid to gas momentum ratio, Equation 3.4, whereas the crossflow Weber number, Equation 3.5, is the parameter that controls the breakup regime [72].

$$q = \frac{\rho_j U_j^2}{\rho_{air} U_{air}^2} \tag{3.4}$$

$$We_{cf} = \frac{\rho_{air} d_j U_{air}^2}{\sigma} \tag{3.5}$$

$$\frac{y_b}{d_j} = kq^n \tag{3.6}$$

The correlations for y_b have a power law form as reported in Equation 3.6,

where k and n are constant values; therefore the jet penetration increases when q goes up. Because of the small distance between the jet inlet and the gear surface (equal to 12.5 jet diameters) and the sub-atmospheric pressure condition that leads to a significant reduction of air density as well as the aerodynamic forces that act on the lubricant flow ($q = 900$ and $We_{cf} = 36$), a notable oil breakup is not expected before the jet impact on the gear. On the contrary, at ambient pressure a significant oil jet breakup may take place, as a result of the air density increase.

As the oil jet hits the high speed gear teeth, a fast momentum transfer occurs. To identify the order of magnitude of the different phenomena involved, a dimensionless groups analysis has been carried out. The useful dimensionless groups for this multiphase system are listed below:

$$Re_j = \frac{\rho_j d_j U_{imp}}{\mu_j} = 3.2 \cdot 10^4 \tag{3.7}$$

$$We_j = \frac{\rho_j d_j {U_{imp}}^2}{\sigma} = 3.9 \cdot 10^5 \tag{3.8}$$

$$Fr_j = \frac{{U_{imp}}^2}{g d_j} = 9.0 \cdot 10^5 \tag{3.9}$$

where U_{imp} is the oil jet impact velocity (Equation 3.10).

$$U_{imp} = \sqrt{{U_j}^2 + {U_p}^2} \tag{3.10}$$

The liquid jet Weber number (We_j) represents the relative magnitude of the liquid inertia forces and surface tension forces, while the Froude number (Fr_j) characterizes the ratio of inertia and gravity forces. As shown by the dimensionless numbers, the phenomenon is driven by the inertia forces, whereas gravity and surface tension effects are negligible.

After the impact, the lubricant can form a thin film on the tooth surface: at this time the characteristic length to be used in the dimensionless group is the film thickness, thus the surface tension and shear forces may not be negligible.

3.2 CFD modelling

3.2.1 Computational domains and grids

In order to carry out a global sensitivity analysis of grid adaptation strategy and model parameters, a simplified geometry has been defined. Subsequently, the resulting numerical set-up has been adopted for the reference geometry's simulation.

Two simplifications have been used:

- symmetry boundary conditions,
- simplified geometry.

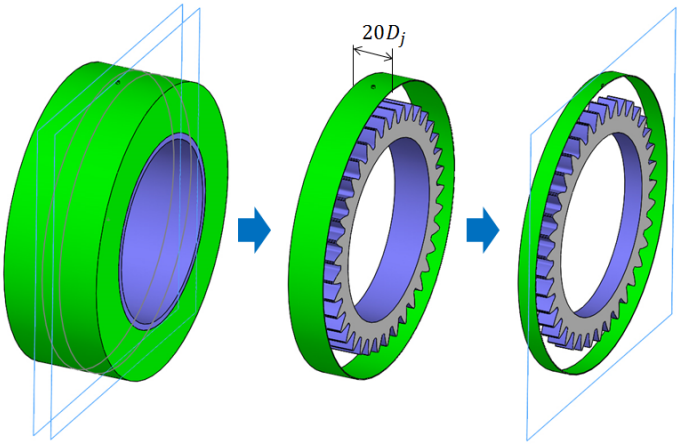

Figure 3.4: Simplified geometry definition.

The symmetry boundary condition has been used, exploiting the geometrical symmetry of the problem with respect to the oil jet axis. This condition leads to a considerable reduction of the computational cost, as only one half of geometry has to be simulated. Preventing the flow from crossing the boundary, symmetry condition introduces an approximation in the URANS simulation, in fact the velocity components of the lubricant

jet aligned with rotational axis are neglected. The impact on the resistant torque calculation due to this boundary condition will be evaluated in this work. The simplified geometry has been obtained by cutting the reference geometry with two radial planes passing through the gear teeth, as represented in Figure 3.4. Each plane is set 10 jet diameters away from the inlet axis, so that the gear face width is 20 times the oil jet diameter.

A sketch of the simplified computational domain is reported in 3.5, whereas that one of the reference geometry is sketched in Figure 3.6.

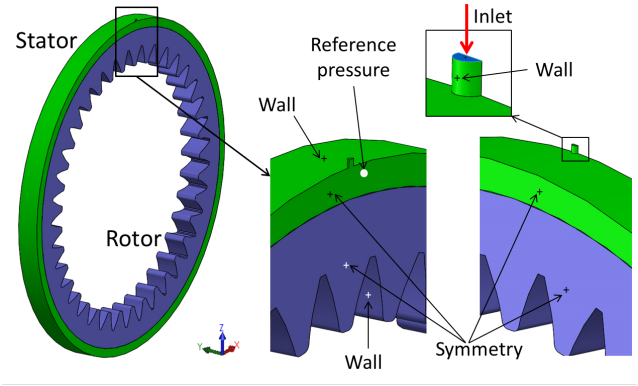

Figure 3.5: Simplified computational domain.

The boundary conditions at the inlet were assigned in terms of a velocity-inlet boundary condition type:

- velocity components: 0, 0, $-U_j$;
- oil volume fraction: 1;
- turbulence equations: a low intensity and a length scale equal to D_j were assumed.

The reference pressure value was fixed at a point located on the symmetry plane highlighted in Figure 3.5 and Figure 6. All the walls were treated as smooth with a no slip condition; casing and inlet duct walls were

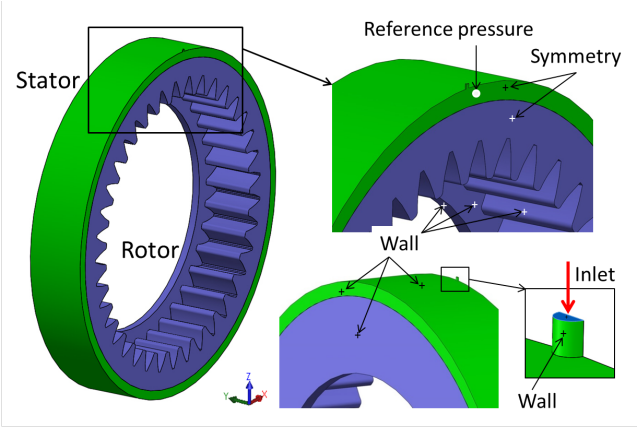

Figure 3.6: Computational domain of reference geometry.

stationary, while the gear and shaft wall were rotating. The symmetry condition for the simplified and reference geometry was set at the surfaces indicated in Figure 3.5 and Figure 3.6 respectively.

The computational domain has been subdivided into two domains: a rotating domain that encompasses the gear and the flow surrounding it, and a stationary one for the flow outside the gear region. The flow field within the rotor has been solved using the rotating reference frame equations, whereas the stationary zone uses the stationary frame equations. The sliding mesh model has been adopted in the this analysis to treat the stator-rotor interface. It is a mesh motion method wherein the rotor domain slides rigidly downwards along the stationary domain. Additionally, the rotor and stator zones are connected with each other through non-conformal interfaces; as the mesh motion is updated in time, the non-conformal interfaces are likewise updated to reflect the new positions of each zone.

The commercial code ANSYS ICEM-CFD has been used to generate the hexahedral meshes. The characteristics of the grids employed for the simulations are reported in Table 3.2 (see also Figure 3.7).

Geometry	Max size	Initial Min size	Initial nodes
Simplified	$D_j/2$	$D_j/8$	$1.06 \cdot 10^6$
Reference	$D_j/2$	$D_j/8$	$2.79 \cdot 10^6$

Table 3.2: Main features of the computational grids before VOF calculation.

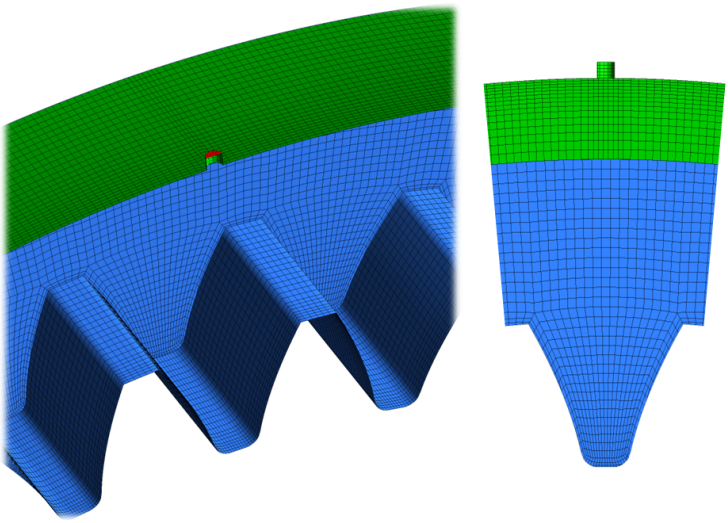

Figure 3.7: Computational grid.

3.2.2 Grid Adaptation method

The solution-adaptive mesh feature implemented in ANSYS Fluent has been used with the aim to confine mesh refinements to specific regions, minimizing the simulation efforts. The initial meshes used in this work contain sufficient cells to represent the shape of the body and to capture the essential features of the aerodynamic flow field. The mesh regions to be adapt during VOF simulations are:

- Liquid-Air Interface (LAI),
- Near Wall Region (NWR).

The refinement of *LAI* region has been obtained by means of the gradient adaptation function, selecting the cells at the air-oil interface based on the gradient of the volume fraction ($\nabla\phi$). Maximum and minimum threshold values for $\nabla\phi$ were fixed before starting the simulation. In particular, the maximum value was set to 0.1 while the minimum to 0.001. The cells, containing a $\nabla\phi$ lower than the minimum threshold, are coarsened whereas cells having a $\nabla\phi$ higher than the maximum threshold are refined. One of the purposes of this approach is to efficiently resolve the liquid surface minimizing numerical diffusion of the interface.

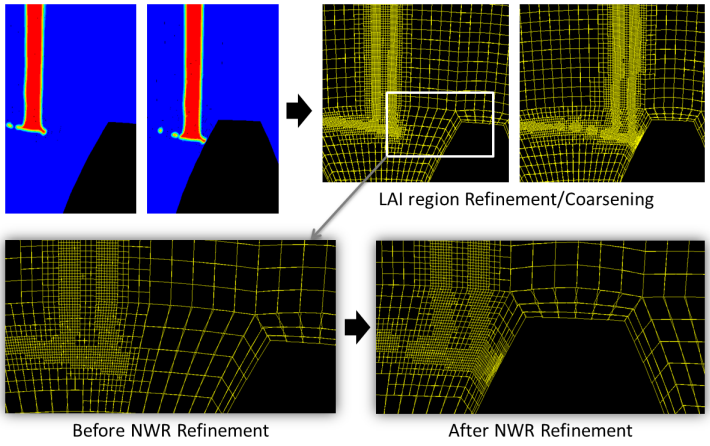

Figure 3.8: Mesh adaptation strategies.

A hybrid adaptation function has been created to refine the *NWR*. Combining the boundary adaptation and the isovalue adaptation functions, native functions of the code, the cells close to the gear tooth surface are refined only if the lubricant is present, in order to reproduce the strong velocity gradients and high shear stresses due to the liquid-solid

interactions. A visualization of the adaptation strategies is reported in Figure 8.

The Hanging Node Adaptation Process [67] is used for the hexahedral grid used in the present work: the mesh is refined by splitting "parent" cell into 8 "child cells", adding a new point on each face of every parent cell, as depicted in Figure 3.9. The Level Of Refinement (LOR), is the parameter that fixes the maximum number of the hexahedron's splits. The mesh is coarsened by uniting the child cells to reclaim the previous parent cell. The grid cannot be coarsened any further than the original grid using the hanging node adaptation process. The adaptation processes are automatically and periodically executed during the unsteady calculation by means of an *Execute Commands* functions.

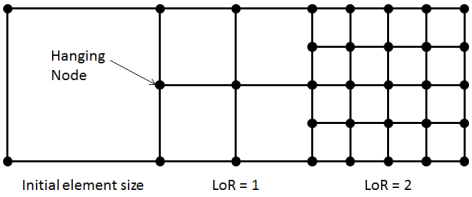

Figure 3.9: Hanging node adaptation process.

A sensitivity analysis of the results to the LOR parameter has been assessed for both strategies of refinement.

3.2.3 Numerical set-up

The commercial code ANSYS Fluent v14 has been used to solve the 3D unsteady RANS equations. A segregated solver with SIMPLEC scheme as velocity-pressure coupling algorithm was selected, in conjunction with a first order backward difference scheme for time discretization, and an explicit scheme for the VOF equation with implicit body forces. The flow system was treated as isothermal, considering air and oil as incompressible fluids (Mach number < 0.3). The pressure field was discretized using PRESTO scheme. A second order upwind scheme was used for the

discretization of the velocity field.

The compressive interface scheme was used for the volume fraction: this is a high resolution differencing scheme that produces an interface that is almost as sharp as the geometric reconstruction scheme [67]. The surface tension force was modelled using the continuum surface force (CSF) model proposed by Brackbill et al. [62] (see section 1.2.1). Although more accurate approaches for the surface tension forces calculation exist, like the CLSVOF approach proposed by Sussman and Puckett [53], the VOF method with CSF model has been adopted because the two-phase problem under consideration is not a surface tension-dominant flow ($We_j = 3.9 \cdot 10^5$). An improvement of the surface tension forces calculation has been obtained acting on grid refinement.

Turbulence was modelled by means of $k - \epsilon$ model, using scalable wall functions for near wall treatment to avoid the deterioration of standard wall functions under grid refinement below $y^+ < 11$. For the convection terms first-order discretization scheme was used.

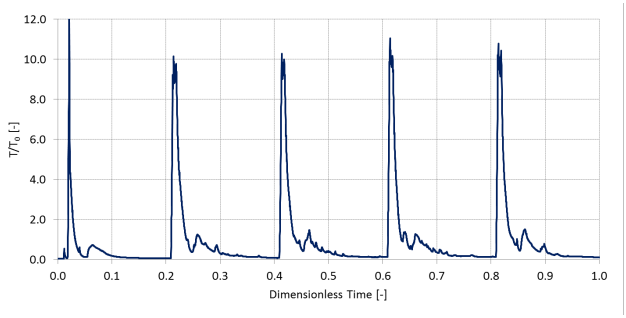

Figure 3.10: Dimensionless resistant torque curve resulting from calculation.

The simulations have been carried out with fixed time step, by maintaining a global Courant number lower than 1. A typical resistant torque curve derived by the simulations is depicted in Figure 3.10: every torque peak is related to an oil jet impact on the gear tooth, and the first

peak is the first one of the calculation. The torque data have been non-dimensionalised by T_0 value, while the time has been non-dimensionalised by 5 tooth passing intervals. Figure 3.10 shows how the calculation has reached a periodicity condition after a few impacts; therefore the simulations were stopped after five impacts. In order to assess the convergence quality of the solution, the scaled residuals were monitored at every time step. The scaled residuals reached a minimum of $5.5 \cdot 10^{-5}$ for every equation.

As regards to computational efforts, the simulation of a simplified geometry with 4 levels of refinement for the *NWR* requires approximately 168 hours using 2 CPUs with Intel® Xeon® Processor E5-2630 with 8 cores or the equivalent of about 2700 CPU hours.

3.3 Results

3.3.1 Flow field initialization

Before starting the VOF simulations, the air flow distribution inside the system is computed. Unsteady single-phase calculations were run, imposing a wall condition at the lubricant inlet instead of the velocity-inlet condition. When the resisting torque reached an asymptotic value, the calculation was stopped. In Figure 3.11 the contour plot of the absolute tangential velocity, made dimensionless by the pitch line velocity, is shown for the reference geometry simulation. How a rotating flow field occurs in the entire domain can be seen, and it is characterized by a tangential velocity of about 90 % of the pitch line velocity in the region between the casing and the gear top land.

In high speed transmissions, the resistant torque due to windage effects becomes very intensive, as reported in the works of Dawson [20], [73]. The calculation of windage losses is not the objective of this study, but it is calculated by VOF simulation and it is added to the resistant torque due to the oil jet lubrication. The sub-atmospheric pressure condition leads to a significant reduction of air density, as a consequence the windage torque decreases with respect to the lubrication torque, in fact windage losses

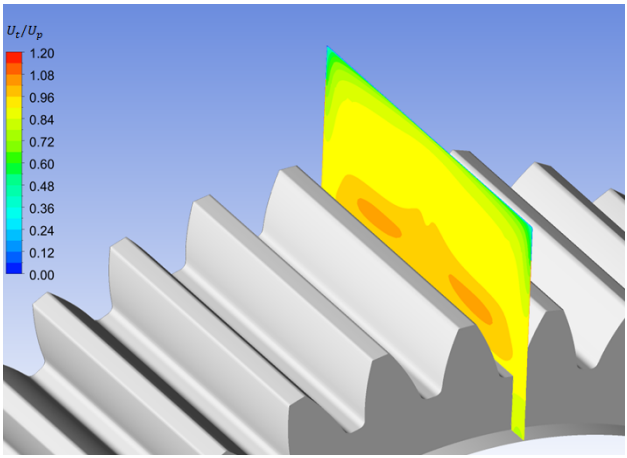

Figure 3.11: Contour plot of U_t/U_p on the section plane for the reference geometry simulation.

are proportional to air density, as presented by Diab et al. [13]. The resultant windage torque will be subtracted from the torque calculated in the VOF simulation, in order to evaluate only the contribution due to the oil jet lubrication.

The windage torques resulting by the single phase simulations of simplified and reference geometries are reported in Table 3.3. The values are non-dimensionalised by the T_0 value, and are relating to the entire gear of 38 teeth.

Geometry	Simplified	Reference
T/T_0	0.02	0.06

Table 3.3: Dimensionless windage torques relating to single phase simulations.

3.3.2 Sensitivity analysis

An extensive sensitivity study has been conducted, evaluating the effect of the computational parameters listed below:

- *LOR* parameter for *LAI*,
- *LOR* parameter for *NWR*,
- geometry simplification (symmetry condition),
- turbulence model.

A better description of the lubricant-gear interactions will be reported in the next section, whereas the main effect of modelling parameters on the resistant torque computations are now presented.

The simulations that were carried out are reported in Table 3.4. The average torque value, T_{ave}, is calculated resolving numerically the Equation 3.11, where the interval [a,b] corresponds to the dimensionless time interval [0.2, 1]. The first peak has not been considered in the average torque calculation.

Run	BC symmetry	LOR LAI	LOR NWR	Turbulence model	$\frac{Final\,nodes}{Initial\,nodes}$	$\frac{T_{ave}}{T_0}$
1	yes	3	-	$k-\epsilon$	2.6	0.995
2	yes	3	3	$k-\epsilon$	2.6	0.995
3	yes	3	4	$k-\epsilon$	4.2	0.885
4	yes	3	5	$k-\epsilon$	8.9	0.883
5	no	3	4	$k-\epsilon$	7.9	0.874
6	yes	3	4	$k-\omega$ SST	4.2	0.873

Table 3.4: Sensitivity analysis: test matrix.

$$T_{ave} = \frac{1}{b-a}\int_a^b T(t)dt \tag{3.11}$$

Results have been compared in terms of the dimensionless average resistant torque, obtaining the bar chart represented in Figure 3.12.

The maximum and minimum values of y+ have been monitored at every time step: on the walls where the lubricant was present, the y+

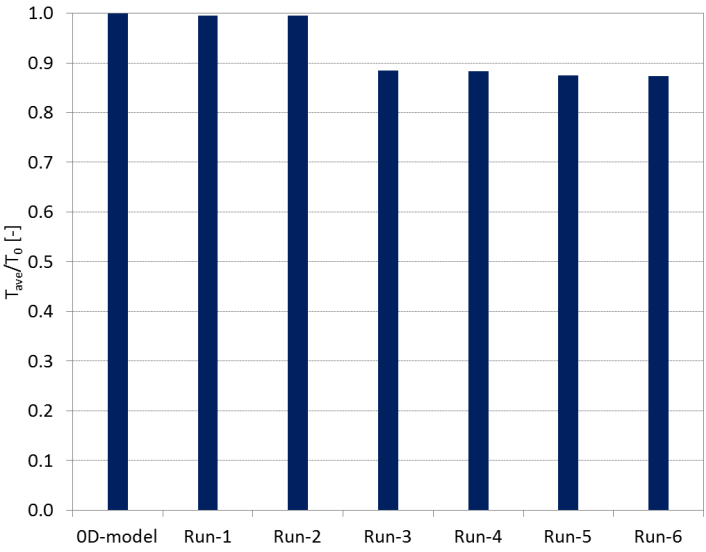

Figure 3.12: Dimensionless averaged torques.

values were kept within the range [20;170] in every simulation, while the mean value was kept within the range [33;52]. A reduction of 25 % in the upper limit of y+ and of 37 % in the mean values was achieved for the simulations where the *NWR* refinement was activated.

The level of refinement for the near wall region is the parameter that mainly affects the resistant torque. Run 1 has no near wall refinement and run 2 has *LOR* equal to 3. In both these cases there is very little variation in average torque compared to T_0. In fact the average torque for Run-1 and Run-2 is the 99.5 % of the 0D-Model value. With *LOR* fixed to 4 (Run-3) the torque decreases by about 11.5 % with respect to the T_0 value. No significant variation of resistant torque is achieved by further increasing the level of refinement; in fact the torque decreases only by 0.2 % passing from *LOR* of 4 to 5. The explanation of these results can be achieved studying Figures 3.13, 3.14 and 3.15.

The results of Run-1 and Run-3 related to the second impact were compared in terms of torque trend (Figure 3.13) and velocity contour plot on the liquid surface (Figure 3.14 and 3.15). The points corresponding to the stages represented in the snapshots of Figures 3.14 and 3.15 are indicated in Figure 3.13 over the torque trends, in order to relate the main features of the impact time history to the physical evolution of the phenomenon.

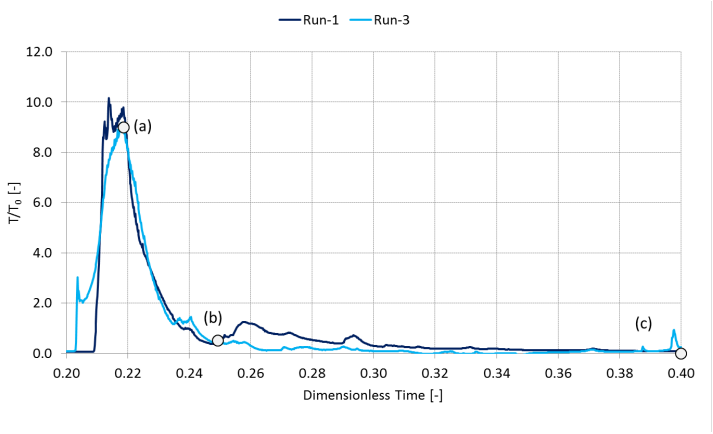

Figure 3.13: Dimensionless resistant torques during the second impact: Run-1 Vs Run-3.

From the data analysis, the liquid-gear interaction can be subdivided in four phases, summarized in Table 3.5, corresponding to dimensionless time intervals: the oil jet hits the tooth face (phase *a*), then passes over the front zone (phase *b*) and the rear zone of the gear top land (phase *c*) and finally the oil film, formed after the impact, moves on the tooth surface (phase *d*). The curves trend differs mainly during the phases *a*, *c* and *d*. To quantify such differences, the average torque related to each interaction phase has been calculated, as summarized in Table 3.6.

The average torque for Run-3 is 11.4 % greater than Run-1 value for the phase *a* and about 70 % lower for phases *c* and *d*; this last difference

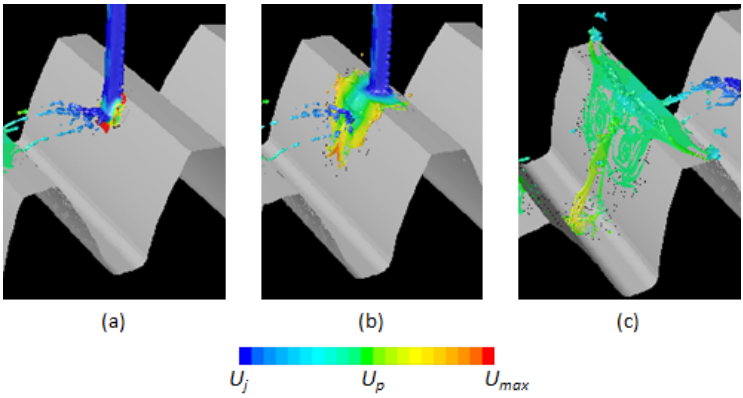

Figure 3.14: Run-1: contour plot of velocity on the liquid surface.

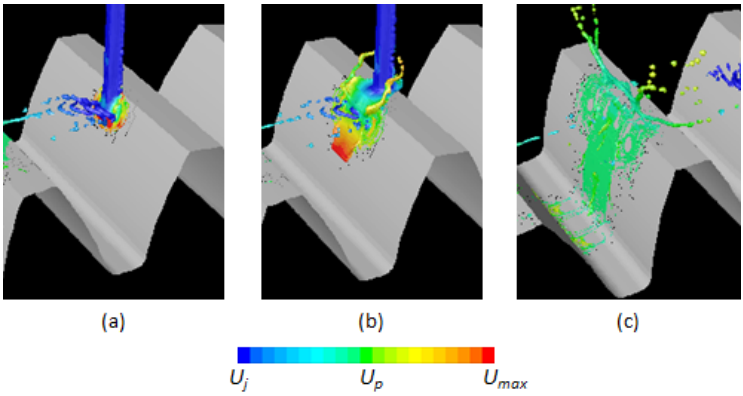

Figure 3.15: Run-3: contour plot of velocity on the liquid surface.

is the main factor leading to the overall average torque overestimation of the Run-1; in fact phases c and d represent together 75.4 % of the overall oil-gear interaction time. The torque differences recorded during phases c and d have been investigated comparing the oil flow field for these periods. As shown in Figure 3.14-c, at the end of phase d the oil

Phase	Description	Dimensionless time interval
a	Oil jet hits the tooth face	$0.20 - 0.22$
b	Oil jet on the front zone of gear top land crest	$0.22 - 0.25$
c	Oil jet on the rear zone of gear top land crest	$0.25 - 0.30$
d	Oil film motion on the tooth surface	$0.30 - 0.40$

Table 3.5: Liquid-gear interaction phases.

Phase	a	b	c	d	Overall
$\Delta time$ %	9.3	15.3	25.4	50.0	100
Run-1	3.85	2.53	0.67	0.14	0.985
Run-3	4.29	2.71	0.20	0.04	0.884

Table 3.6: Average dimensionless torques related to the oil-gear interaction phases during the second impact: Runs 1 and 3.

covers the tooth crest in Run-1, whereas no oil is observed in such a region in Run-3 (Figure 3.15-c).

This behaviour can be explained by studying the contour plots of the volume fraction field on the symmetry plane, reported in Figure 3.16. For Run-1 and Run-2 the oil jet impinges on the tooth crest, forming an oil film that expands radially, exchanging momentum with the gear surface. When LOR is set to 4, there are a greater number of computational cells within the boundary layer zone and then the strong velocity gradients, due to the liquid-solid interactions, are better reproduced. In this case, the oil jet does not impinge on the tooth crest but forms a suspended oil film. As the jet passes over the gear top land, the oil mass flow that reaches the jet base does not impinge on the gear surface, but feeds the liquid film that breaks up into ligaments and small droplets. This amount of oil is not involved in the gear lubrication process and the total oil mass that exchanges momentum with the gear decreases, resulting in the resistant torque reduction. When the LOR parameter for near wall region is set to 5 (Run-4), a similar suspended film is obtained.

The other computational parameters do not significantly affect the

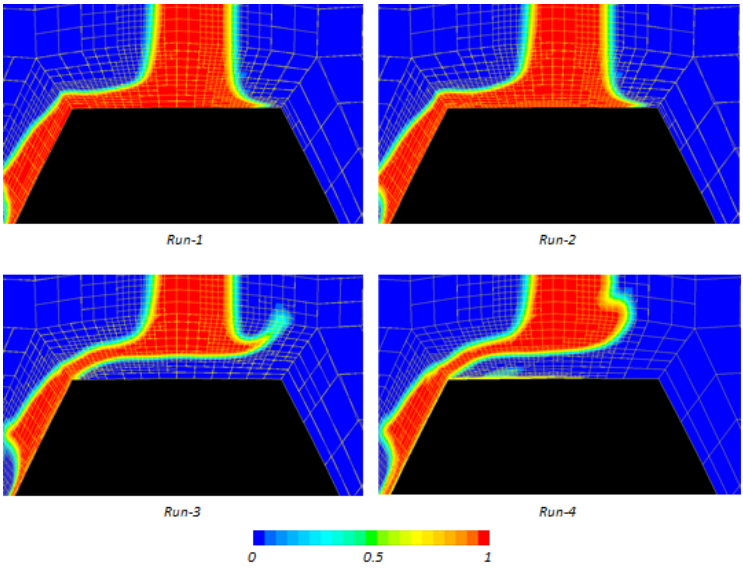

Figure 3.16: Contour plot of oil volume fraction at the symmetry plane: Runs 1, 2, 3, and 4.

resistant torque. To assess the effect of symmetry boundary condition on the torque calculation, in Run 5 a new mesh was adopted. It was generated redoubling the grid used for the other runs with respect to the symmetry plane. As can be seen from results (see Table 3.4), the symmetry plane boundary condition do not significantly affect the results, in fact the average resistant torque for Run-3 is 1.14 % greater than Run-4 value. As regards the turbulence modelling, in Run-6 the model $SSTk-\omega$ was used instead of $k-\epsilon$: this leads only to an average torque reduction of 1.2 %.

3.4 Reference geometry analysis

Two simulations of the reference geometry have been carried out, exploiting the numerical setup obtained by sensitivity analysis. The simulation parameters are reported in Table 3.7.

Run	BC symmetry	LOR LAI	LOR NWR	Turbulence model	$\frac{Final\,nodes}{Initial\,nodes}$	$Tave/T_0$
3D-1	yes	3	4	$k-\epsilon$	2.3	0.899
3D-2	yes	4	4	$k-\epsilon$	3.9	0.865

Table 3.7: Modelling parameters adopted in the reference geometry simulations.

During the sensitivity analysis, the effects of the level of refinement of the liquid-air interface on the resistant torque were not evaluated. This sensitivity has been assessed in the present section, comparing the average resistant torques arising from the simulations, as summarized in Table 3.7. The average resistant torque derived by the Run 3D-2 is only 3.8 % lower than the Run 3D-1 value, while the mesh node number is about double. The main effect of the highest level of refinement for LAI regions is a greater breakup of oil ligaments after the impact with the gear. Below the results obtained by Run 3D-2 are discussed.

3.4.1 Resistant torque analysis

A visualization of the resistant torque curve is depicted in Figure 3.17: how the curve reproduces the periodic nature of the jet lubrication can be seen. Moreover, it is important to note that instantaneous torque reaches maximum values about 12 times above the mean value (T_0) determined by 0D-Model.

A better description of the lubricant-gear interactions can be achieved focusing on the second impact: the resistant torque trend and the corresponding cumulative torque curve are depicted in Figures 3.18 and 3.19, respectively. In both graphs, some characteristic flow times are

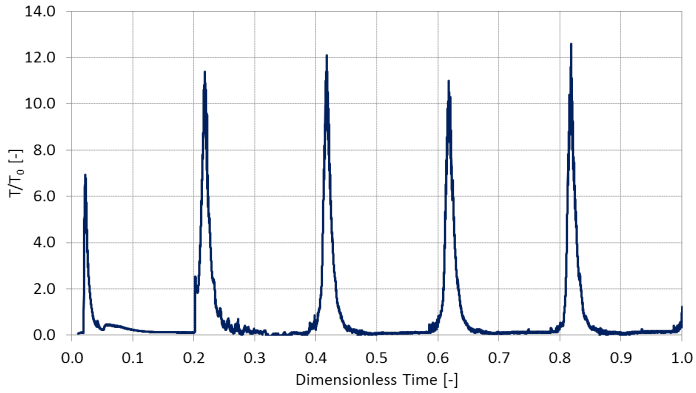

Figure 3.17: Dimensionless resistant torque curve for Run 3D-2.

highlighted, to relate the torque history to the isosurface plots reported in Figure 3.20.

The oil jet reaches the tooth without the occurrence of significant deformation and breakup phenomena, then hits the tooth flank (point 1). The momentum transfer occurs in a very short time, leading to the resistant torque peak. At this time the tooth has transferred to the liquid thirty percent of the total momentum exchanged. On the tooth flank, the jet forms a thin oil film that gets down with high velocity toward the gear axis, as guessed by Dewinter and Blok [32] (see section 1.1.2).

When the oil jet is passing over the gear top land the lubricant does not impinge on the gear, but forms a liquid film that flies over the tooth (Figure 3.20-2 and 3.20-3). At this time, the lubricant that is reaching the jet base feeds the suspended film that breaks up into ligaments and small droplets. This amount of oil is not involved in the gear cooling process, and the total oil mass that exchanges momentum with the gear decreases, resulting in a reduction of average torque with respect to 0D-Model value.

The jet remains connected to the oil on the tooth flank by means of the liquid film: the jet drags the oil ligament close to the tooth crest until the oil film does not break up, as visible in Figure 3.20-4. The detached oil

ligament moves away from the gear tooth in the radial direction, spreading in the axial direction. When the oil jet is passing over the tooth crest (point 3) the gear has transmitted ninety percent of the total momentum.

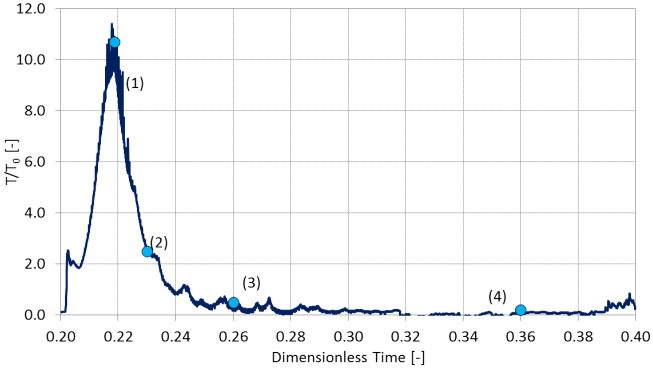

Figure 3.18: Second impact data related to Run 3D-2: dimensionless resistant torque.

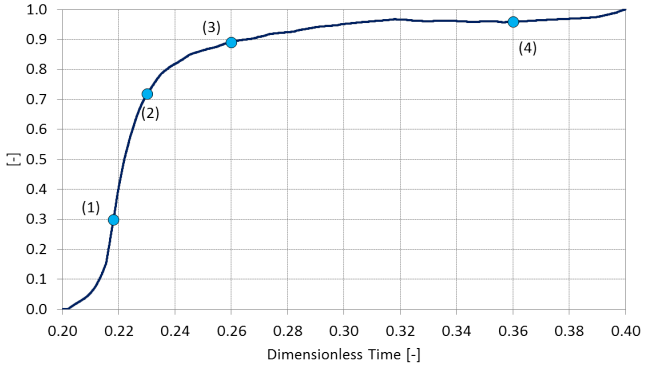

Figure 3.19: Second impact data related to Run 3D-2: cumulative torque curve normalized.

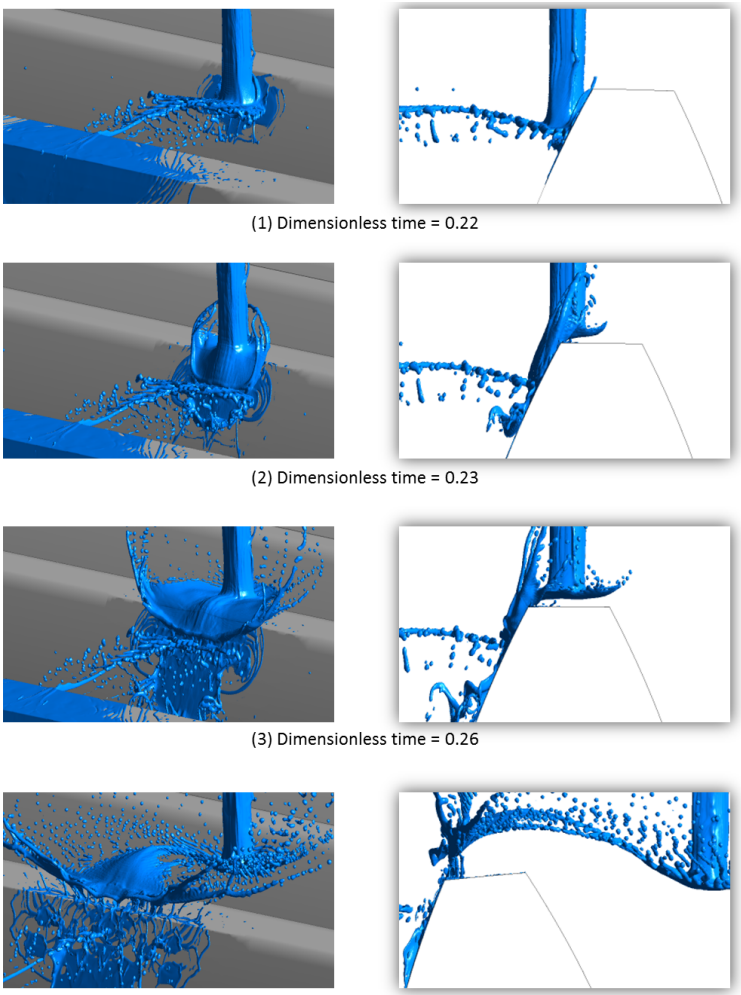

Figure 3.20: Run 3D-2: isosurface of oil volume fraction equal to 0.5.

In order to analyse the relative contribution of pressure and shear

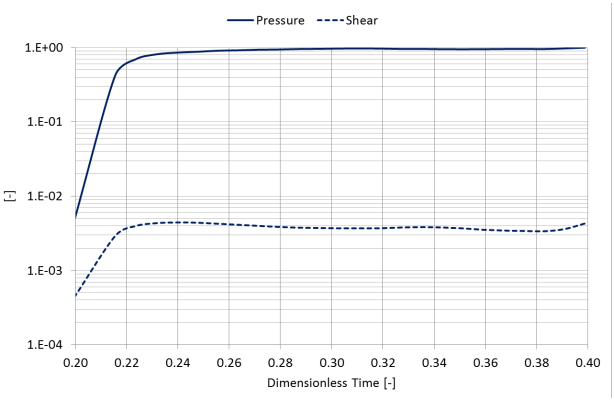

Figure 3.21: Second impact data related to Run 3D-2: normalized cumulative torque curves resulting by pressure and shear forces.

forces to the resistant torque calculation, the normalized cumulative torque curves, resulting from both forces, are reported in Figure 3.21. These data are related to the second impact. How the shear force contribution is very low can be observed; in particular, it is at least two orders of magnitude lower than the pressure data. This result proves that the mechanism which mainly contributes to the resistant torque is the pressure distribution on the tooth flank resulting from the oil jet impact, while the shear forces contribution is negligible.

3.4.2 Lubrication performance

The torque calculation allows the assessment of the power losses relating to oil jet lubrication; however, a lot of other useful information may be provided by VOF simulations. In particular, for gearbox designers is very important to know how deep the jet can penetrate between the teeth and how much coverage of oil it provides to the contact surfaces. Consequently, the lubrication performance have been evaluated defining:

- the lubrication Coverage Factor (CF),

- the oil jet Penetration Factor (PF).

The former has been defined as the wetted surface of the gear normalized by the area of oil jet cross section. The latter factor, defined by Equation 3.12, describes the normalized average value of the oil penetration between the teeth, where $R(t)_{awa}$ is the area-weighted average of the radial coordinate on the wetted surface at time t. PF is equal to zero when the oil does not penetrate into the tooth space, while tends to 1 as the lubricant moves toward the tooth root.

$$PF = \frac{R_{tip} - R(t)_{awa}}{R_{tip} - R_{root}} \tag{3.12}$$

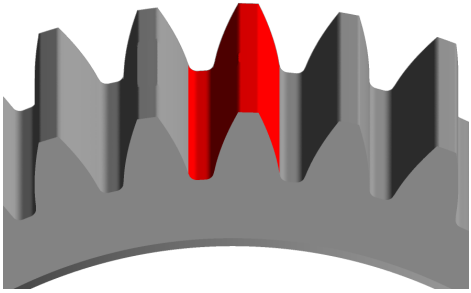

Figure 3.22: Visualization of the tooth surface considered for the calculation of Coverage and Penetration Factors.

The lubrication performance have been assessed by focusing on the gear tooth involved in the second impact: the tooth has been tracked during the simulation, by evaluating how the coverage and penetration factors change with time. The tooth surface considered for the calculation of CF and PF is highlighted in Figure 3.22.

In Figure 3.23 the Coverage Factor is plotted against dimensionless time. The CF increases with time, reaching a maximum value of 120 at dimensionless time equal to 0.96, then it starts to decrease. The integral mean value of CF, calculated within the time interval [0.2 , 1.0], is equal

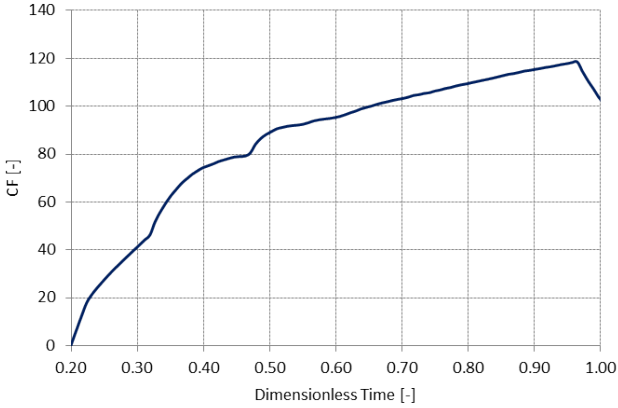

Figure 3.23: CF, as function of dimensionless time, calculated on the gear tooth involved in the second impact.

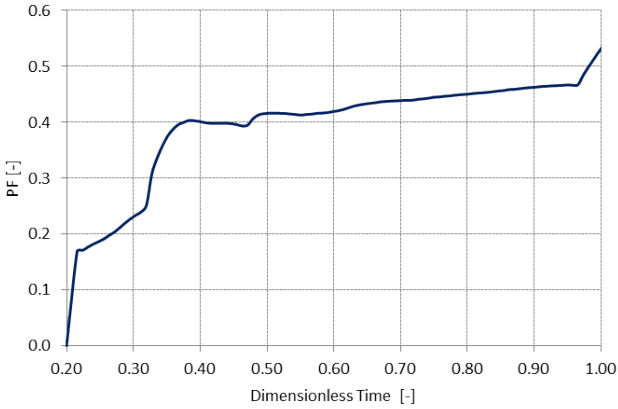

Figure 3.24: PF, as function of dimensionless time, calculated on the gear tooth involved in the second impact.

to 87, meaning that the lubricant averagely covers a surface equal to 87 times the cross sectional area of the oil jet.

By analysing CF curve and the graph of PF, reported in Figure 3.24, useful insights on the lubricant film behaviour can be achieved. As the oil jet hits the gear tooth a thin oil film starts to growth on the tooth surface, developing with high velocity toward the tooth root, as shown by the abrupt increase of penetration factor in Figure 3.24. At dimensionless time 0.22, which correspond to the maximum value of the torque curve shown in Figure 3.17, the PF and CF are equal to 0.17 and 16, respectively. After this time, the slope of the curve changes for both factors.

The oil film expands, moving toward the tooth root with constant speed until reaching the normalized time 0.33. At such instant, the first derivative of both curves increases; this can be explained by analysing Figure 3.25, where the liquid surface is observed from top and axial views, at time 0.25 and 0.31. In the earliest stages of oil film growth, a cluster of suspended droplets and ligaments is created, as shown in Figure 3.25-a. This lubricant quantity, which moves toward the tooth root (see Figure 3.25-b), drops on the tooth surface at time 0.32. This phenomenon leads to the sudden increase in CF and PF discussed before. When the group of ligaments and droplets hits the teeth surface, it breaks up forming a thin film which expands on the tooth space, crossing the tooth root, climbing the opposite tooth face, and thereby leaving the control surface defined for lubrication performance analysis.

The oil on the control surface continues to expand increasing the Coverage Factor, whereas the Penetration Factor remains approximately constant. A new abrupt change in the shape of both curves is observed at normalized time equal to 0.47; this can be explained with the aid of Figure 3.26, where the oil distribution during such a time is observed from top and axial views. In the picture, the profile of the tooth involved in the second impact is highlighted in red. As indicated by the circle in the picture, it can be observed how the back face of tooth under investigation is hit by an amount of suspended lubricant generated by the third impact of the oil jet with the gear. It is this phenomenon that lead to the sudden

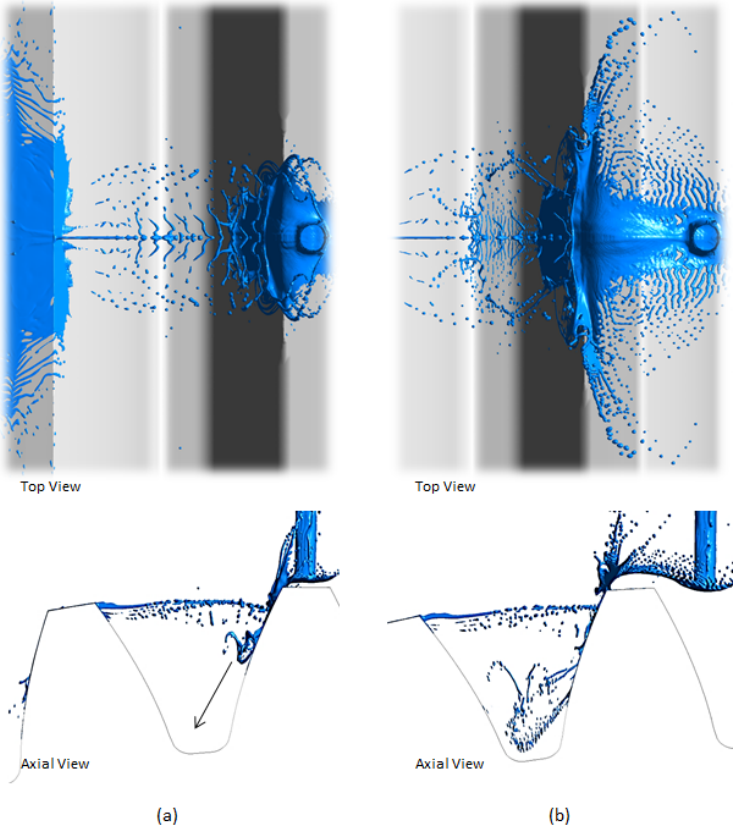

Figure 3.25: Iso-surface of oil volume fraction equal to 0.1: (a) Top and Axial view at time = 0.25, (b) Top and Axial view at time = 0.31.

increase of the coverage and penetration factors at time 0.47.

The oil film that cover the gear surface is subjected to centrifugal forces which tend to strip off the oil layer from the tooth surface. Therefore, the oil is pumped towards the tooth top land where it is expelled in radial direction. The lubricant is ejected away from the gear surface at dimensionless time equal to 0.97, as visible by the abrupt decrease of CF

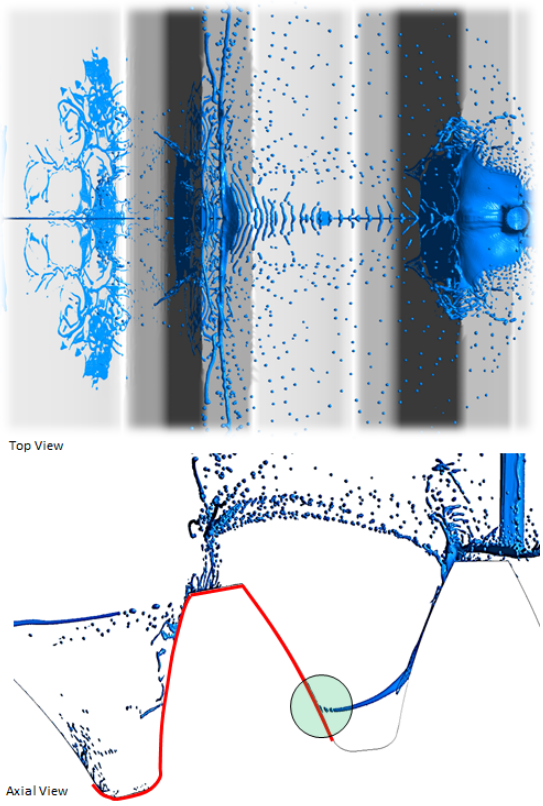

Figure 3.26: Iso-surface of oil volume fraction equal to 0.1: Top and Axial view at time = 0.47.

in Figure 3.23. Consequently , the PF increases because of the reduction of the oil quantity located close to the gear top land.

In the light of the above, it may be concluded that the velocity of the oil film formation, expansion and expulsion from the tooth surface is sensibly slower than the momentum transfer. In fact, comparing Figures 3.19 and 3.23 , it can be seen how, in a normalized time interval of

about 0.06, the gear is able to transfer the 90% of the total momentum exchanged, while the lubricant coverage starts to reduce only after a time interval equal to 0.77, having considered the time 0.2 as the initial time for the film formation. Therefore, the lubrication phenomena take place in a characteristic time an order of magnitude greater than the momentum transfer mechanism.

3.5 Analysis of the oil jet inclination and injection velocity

Several simulations varying the oil jet inclination (α) have been performed, in order to evaluate how this parameter affects the resistant torque and the lubrication performance. As shown in Figure 3.27, the injection angle was obtained rotating the oil jet axis with respect the intersection point between the pitch circle and the vertical axis.

The tested injection angles, normalised by the maximum injection angle, are listed below:

- $\alpha = 0.0$
- $\alpha = 0.33$
- $\alpha = 0.66$
- $\alpha = \alpha_{max} = 1.0$

As regards to the injection velocity study, two values were tested, corresponding to the following values of the velocity coefficient UR, defined as the ratio between oil jet velocity and pitch line velocity:

- $UR_1 = \frac{U_j}{U_p} = 0.25$
- $UR_2 = 0.35$

The injection velocity rises of 40 % from the former to the latter coefficient. In this study, the simplified geometry has been used, changing the inlet duct position and inclination as function of α, in particular, a new grid of the stationary domain has been realized for each injection angle. The numerical set-up derived by the sensitivity analysis has been employed (see Table 3.8). As in previous cases, the simulations were stopped after five impacts.

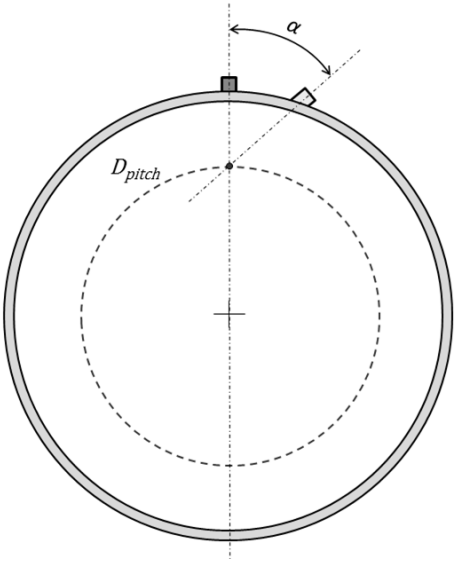

Figure 3.27: Definition of the oil jet inclination angle (α).

BC symmetry	LOR LAI	LOR NWR	Turbulence model
yes	3	4	$k-\epsilon$

Table 3.8: Modelling parameters adopted in the simulations.

3.5.1 Resistant torque analysis

Results have been compared in terms of average torque with the values resulting by 0D-Model, obtaining the chart represented in Figure 3.28. 0D-Model curves, the black dashed and continuous lines, have been achieved by Equation 3.2 by varying the injection angle between 0 to α_{max}, for both velocity coefficients. The average torque values obtained by simulations were calculated resolving numerically the Equation 3.11, where the interval [a,b] corresponds to the dimensionless time interval [0.2,

1]. The first peak is not been considered in the average torque calculation. Each torque value was non-dimensionalised by T_0 (given by Equation 3.3).

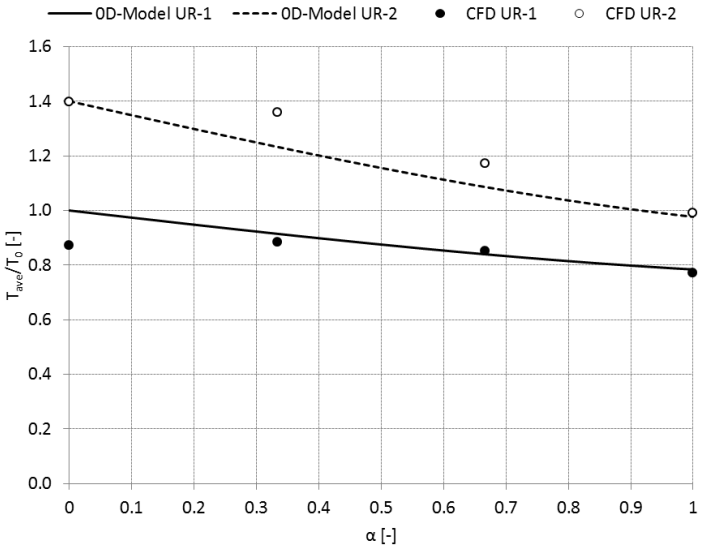

Figure 3.28: Dimensionless averaged torque: 0D-model vs CFD.

0D-Model provides for a reduction of the average torque as α increases, because of the lower difference in tangential velocity between the oil jet and tooth surface (see Equation 3.1). An increase of jet velocity leads to a growth of the resistant torque, due to the greater lubricant amount which has to be accelerated by the tooth.

A good agreement between CFD results and 0D-Model is clear. In the following, a detailed analysis of results is reported.

The main assumptions of 0D-Model are: firstly, the entire mass of oil jet reaches the gear teeth, secondly, all the lubricant is accelerated up to the pitch line speed. However, both these assumptions are not always respected when the injection angle and velocity vary.

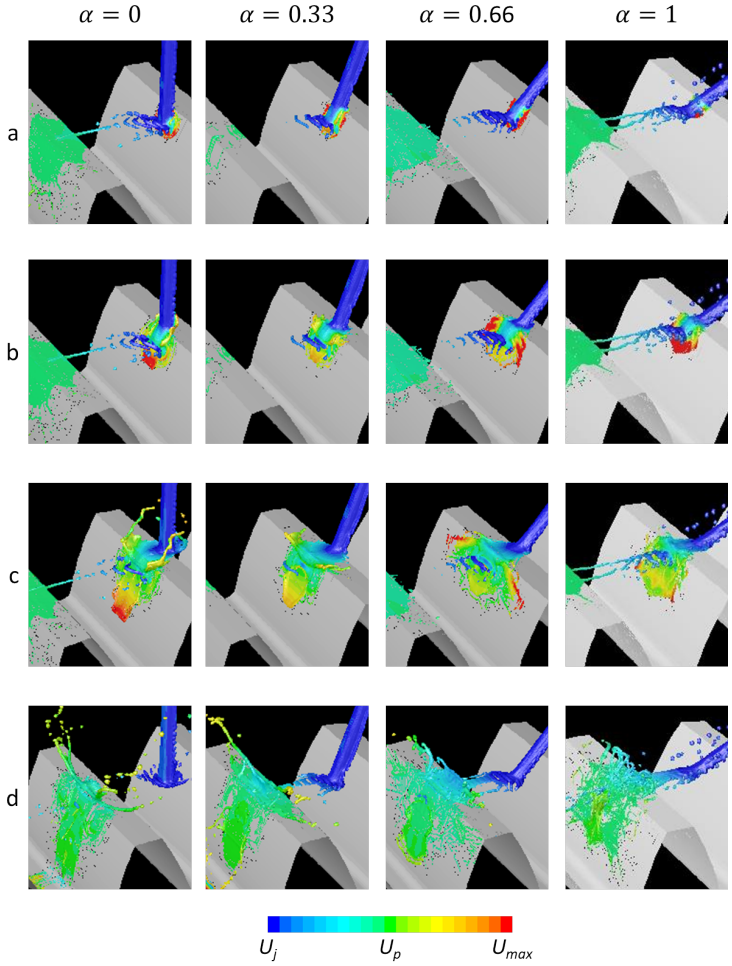

Figure 3.29: Contour plot of absolute velocity on the liquid surface, to the different injection angles. The velocity coefficient is equal to UR_1. The snapshots are related to the dimensionless times below: a) 0.215, b) 0.23, c) 0.26, d) 0.36.

Focusing on CFD outcomes related to UR_1, it can be observed how results approach the values of 0D-Model when the injection angle increases: this trend can be explained by analysing Figure 3.29, where velocity contour plots on the liquid surface are shown, for each injection angle. Four time instants have been selected with the aim to compare both impact phenomenon and oil film growth. In each column the snapshots concerning a single injection angle are reported, whereas each row is relating to a specific time instant. The radial coordinate at which the first interaction between lubricant and tooth takes place is above the pitch radius, and moves toward higher values as the injection angle increases; this is not totally in agree with the second hypothesis of 0D-Model. Therefore such model would tend to underestimate the average torque as the injection angle rises up. This does not happen because also the first hypothesis of the theoretical model is not completely verified. For zero injection angle the oil jet does not impinge on the tooth crest but forms a suspended oil film, as discussed in section 3.4. For this reason, the total oil mass which exchanges momentum with the tooth decreases, leading to a resistant torque reduction; in the theoretical model this is equivalent to a reduction of $\dot{m}_j$ in the Equation 3.2. When the injection angle is greater than zero, the lubricant does not fly over the gear top land but reaches such a region. The amount of oil having direct contact with the tooth is accelerated up to the tooth surface speed, while the upper layers flow on the underlying oil, moving away in radial-tangential direction. This oil mass does not reach the superficial gear speed, as highlighted by to blue-green colour of the lubricant in Figure 3.29-d, therefore it accounts for a reduction in the resistant torque. The combination of two phenomena discussed above leads to results in Figure 3.28, where a considerable agreement between CFD and 0D-Model is achieved when α is equal to 0.66 and 1. In the numerical simulation with $\alpha = 1$ a further deficiency in the torque value is due to a numerical problem which rises at the stator-rotor interface: with such injection angle a significant misalignment rises between the grid cells of the stator and rotor that leads to formation of non-physical droplets around the oil jet, as can be seen in Figure 3.29-d for $\alpha = 1$.

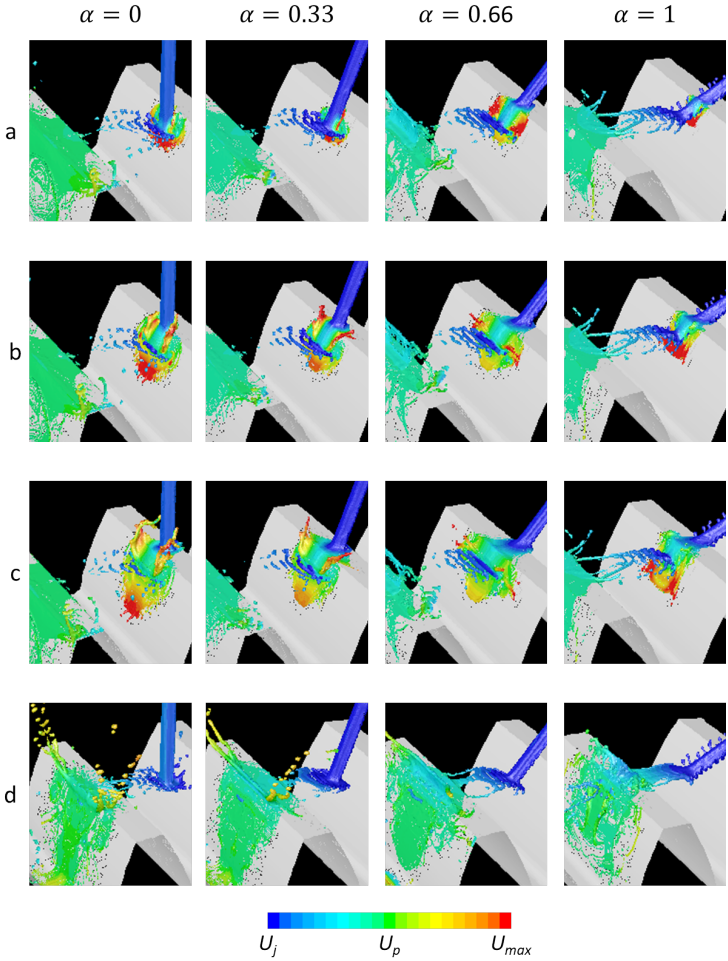

Figure 3.30: Contour plot of absolute velocity on the liquid surface, to the different injection angles. The velocity coefficient is equal to UR_2. The snapshots are related to the dimensionless times below: a) 0.22, b) 0.24, c) 0.26, d) 0.37.

Concerning the results of simulations with the velocity coefficient equal to UR_2, when α is fixed to 0 and 1, the average torque values resulting by CFD and 0D-Model are overlapping, on the contrary, higher values are obtained for the other injection angles. Similarly to Figure 3.29, in Figure 3.30 the velocity contour plots on the liquid surface for the different injection angles are shown for the velocity coefficient equal to UR_2. By increasing the injection velocity, the amount of lubricant involved in the impact increases, consequently consider that the lubricant acceleration occurs at the pitch radius rather than to higher radial positions, leads the theoretical model to underestimate the average torque. However a very good agreement between CFD results and 0D-model is reached with injection angles of 0.33 and 0.66. This is because, in such configurations, does not all the lubricant is accelerated by the gear tooth. In fact, in the simulation with $\alpha = 0$ the oil covers only partially the tooth crest, as observed in Figure 3.30-d. For $\alpha = 1$ a different phenomenon takes place. As discussed above, despite the oil reaches the gear top land when the injection angle is increased, only the lubricant having direct contact with the tooth is accelerated up to the tooth surface speed, while the upper layers flow on the underlying oil, moving away in radial-tangential direction. This mass has only partially transferred momentum with the gear, as highlighted by to blue-green colour of the lubricant in Figure 3.30-d, hence this causes a reduction of the average resistant torque. The amount of oil which slides and moves away from the tooth increases with the injection angle, therefore is greater in the simulation with $\alpha = 1$. For such injection angle, a further reduction in the torque value is due to the growth of non-physical droplets at the stator-rotor interface (seen in Figure 3.30-d), as already discussed for the simulation with velocity coefficient equal to UR_1. The combination of such phenomena leads to the considerable agreement between CFD and 0D-Model for $\alpha = 1$.

A quantitative comparisons between the different injection configurations can be achieved by analysing the torque trend and the corresponding cumulative torque curve, depending on the angle and velocity of injection. The data are related to the second impact of the oil jet with the gear

teeth, and each cumulative curve has been normalized.

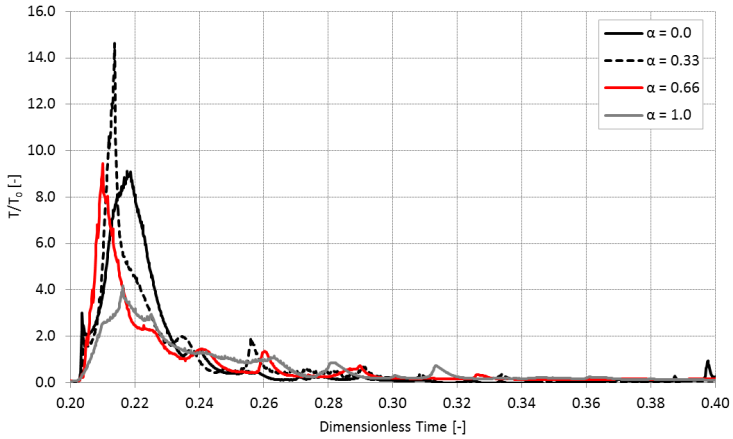

Figure 3.31: Second impact: dimensionless resistant torque (UR_1).

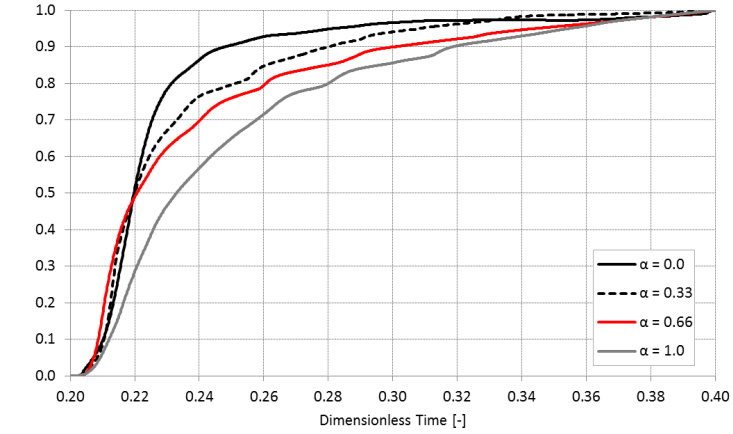

Figure 3.32: Second impact: cumulative torque curve normalized (UR_1).

With regard to velocity coefficient equal to UR_1, in Figure 3.31 and 3.32 the torque graphs and the cumulative torque curves are reported, respectively. By observing Figure 3.31 it can be seen how the torque peak is sensibly affected by the injection angle, both in module and at the time at which it occurs. From a physical point of view, the torque peak is correlated to the amount of lubricant accelerated at that time. The maximum peak takes place when α is equal to 0.33, reaching a value of about 15 times T_0, whereas is about 9 times T_0 with $\alpha = 0$ and $\alpha = 0.66$. As regard to the injection angle of 1, the curve has a tendency to flatten, leading to a peak value of 4 times T_0. The maximum torque value occurs first in the simulation with the injection angle of 0.66, then in the one with $\alpha = 0.33$, finally in those having $\alpha = 0$ and $\alpha = 1$.

Varying the injection angle, the momentum transfer between gear and lubricant occurs with different velocities: such differences are well shown in Figure 3.32. The lubricant acceleration is very fast for all the simulations with the exception of the case with $\alpha = 1$, in fact the growth of the corresponding cumulative curve is slower than the other curves. It is interesting to note that the curves for injection angles equal to 0, 0.33 and 0.66 intersecting at dimensionless time 0.22, which correspond to a value for the cumulative curve of 0.5. Therefore, in a time range of 0.02, which corresponds to 10 % of one tooth passing interval, these configurations have already transferred the fifty percent of the overall momentum exchanged, while the thirty percent is achieved by the simulation with $\alpha = 1$. After time 0.22, for $\alpha = 0$ the oil acceleration is faster than in the other configurations, in fact the 90 % of the global momentum transferred is reached at time 0.25. The other angles reach the 90 % of the momentum transferred at time 0.28, 0.30 and 0.32 respectively for angles of 0.33, 0.66 and 1. Therefore, the normalised cumulative curve is a simple parameter which allows to evaluating the amount of lubricant accelerated at a specific time instant, with respect to the total mass involved into one tooth passage.

In Figure 3.33 and 3.34 the resistant torque and cumulative curves related to the velocity coefficient of 0.35 are shown. An increase of forty

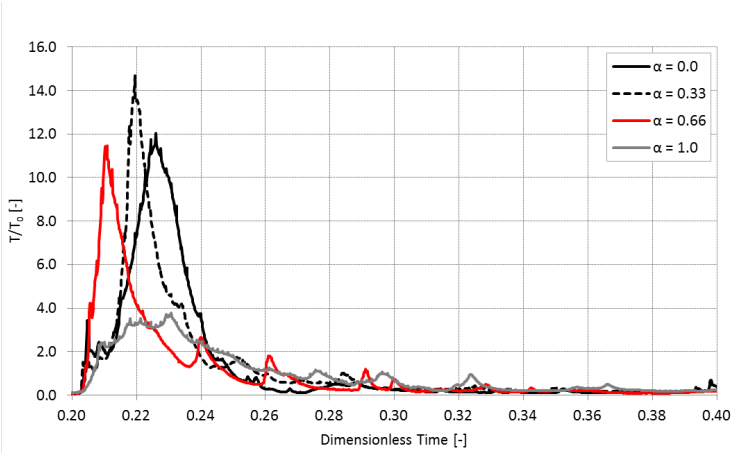

Figure 3.33: Second impact: dimensionless resistant torque (UR_2).

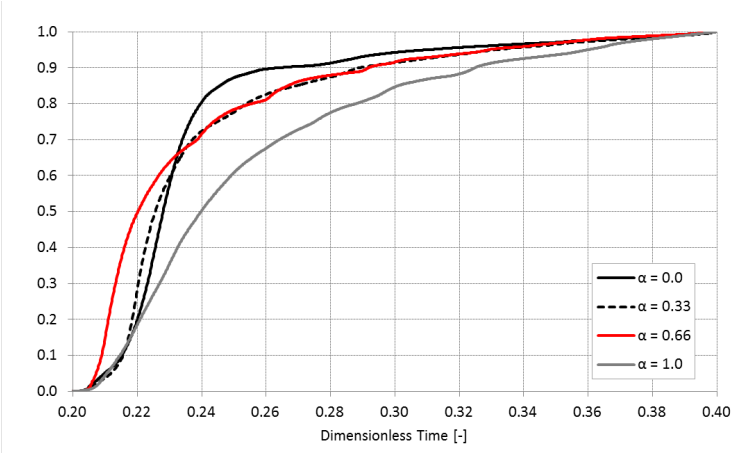

Figure 3.34: Second impact: cumulative torque curve normalized (UR_2).

percent in the oil injection velocity causes an increase of the torque peak by 27 % for injection angles of 0 and 0.66, whereas for $\alpha = 0.33$ and 1 it is

about the same obtained by simulations with velocity coefficient of 0.25.

It should be noted that the maximum torque value is achieved with the injection angle of 0.33, to both the tested injection velocities: this angle corresponds exactly to the pressure angle of the gear.

The oil jet velocity also influences the time at which the torque peak occurs. By comparing Figure 3.31 and 3.33, a time shift of the maximum torque value can be identified for the injection angles of 0 and 0.33. On the contrary, for the other inclinations, the peak occurs at about the same instant of time.

As regards the momentum transfer velocity, it can be observed in Figure 3.34 that it occurs with a lower speed with respect to the simulations with the velocity coefficient fixed to 0.25, with the exception of the simulation with $\alpha = 0.66$. In fact, at time 0.22, the cumulative torque curve is equal to 0.2 for $\alpha = 0$ and $\alpha = 1$, and 0.3 for $\alpha = 0.33$, on the contrary, for the injection angle of 0.66 the cumulative torque curve remains at 0.5 as in the simulation with velocity coefficient equal to UR_1.

In summary, the resistant torque due to the oil jet lubrication, and hence the correlated power loss, is a function of both oil jet inclination and injection velocity. The 0D-Model is able to reproduce the average torque trend, showing a good agreement with CFD results. Clearly, 0D-Model can not provide information about the instantaneous torque as well as about the peak values. CFD results have shown that the torque peak value is about ten times the average value; the absolute maximum is reached when the lubricant is injected with the same inclination of the pressure angle of the gear. A further increase of the oil jet inclination leads to a more gradual momentum transfer between the gear teeth and lubricant, as well as the torque peak value reduction. By increasing the oil jet velocity, the mean torque enhances for every injection angle, whereas the peak value shows a lower sensitivity.

In order to select the optimum set up for the oil injection system, the lubrication parameters have to be assessed.

3.5.2 Lubrication performance

Useful information regarding lubrication performance can be formulated by observing the contour plots of absolute velocity on the liquid surfaces presented in Figures 3.29 and 3.30, previously discussed. At a first insight, the imprint of the lubricant on the gear tooth has a greater extension, both in radial and axial direction, into the simulations that adopting an higher injection velocity, as visible by comparing the snapshots in the row d in Figures 3.29 and 3.30. As regards the comparison between the different injection angles, it is not so clear which one provides the greater oil coverage on tooth surface.

More details can be obtained exploiting the coverage and penetration factors defined in section 3.4.2. As carried out in such a section, the lubrication performance have been obtained by analysing the gear tooth involved in the second impact: the tooth has been tracked during the simulation, by evaluating how the coverage and penetration factors change with time. The surface considered for the calculation of CF and PF is highlighted in Figure 3.22. For every value of α, the mechanisms of oil film formation, expansion and expulsion are basically similars to that explained in section 3.4.2.

Regarding the lower injection velocity, the CF and PF factors are reported in Figure 3.35 and 3.36, respectively. When the oil jet hits the gear tooth, a thin oil film quickly starts to growth. In this first stage of film growth, it expands toward the tooth bottom, as evidenced by the rapid increase of PF in Figure 3.36 at dimensionless time about 0.2. A that stage follows a oil film growth toward axial direction, independently of the injection angle, as visible in Figure 3.29 rows b and c; this results in the coverage factor increase. The maximum value reached by the coverage factor is a function of the injection angle. When $\alpha = 0$ the CF curve achieves a maximum of 110. As the angle increases, the maximum reaches a value of 130 and 140 for $\alpha = 0.33$ and 0.66, respectively. With the injection angle sets to 1, the peak value decreases with respect to the other injection geometries. Concerning the penetration factor, in Figure 3.36 it can be observed how it decreases when the injection angle increases.

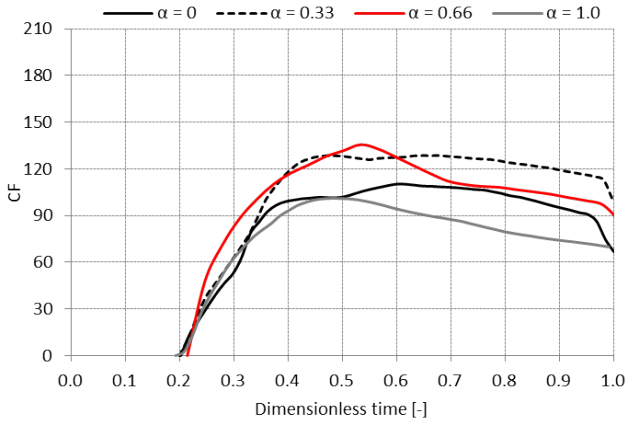

Figure 3.35: CF, as function of dimensionless time, calculated on the gear tooth involved in the second impact (UR_1).

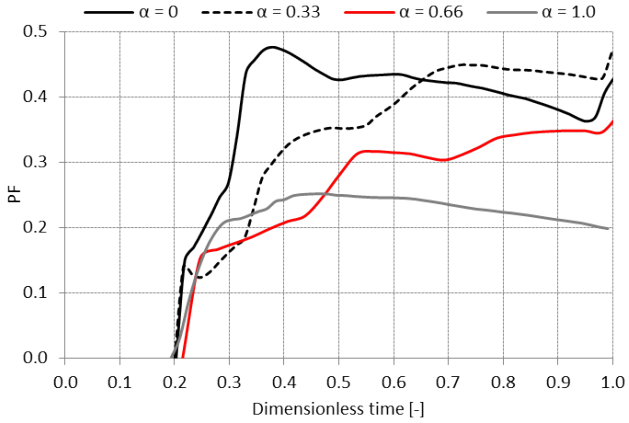

Figure 3.36: PF, as function of dimensionless time, calculated on the gear tooth involved in the second impact. (UR_1).

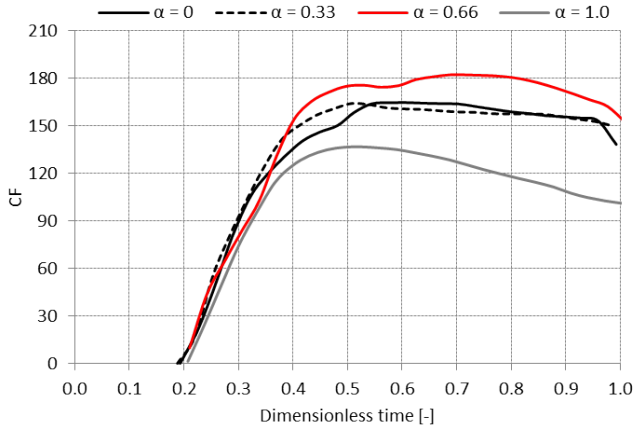

Figure 3.37: CF, as function of dimensionless time, calculated on the gear tooth involved in the second impact. (UR_1).

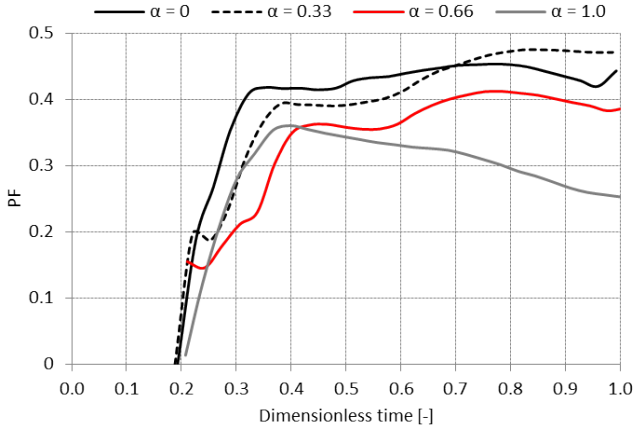

Figure 3.38: PF, as function of dimensionless time, calculated on the gear tooth involved in the second impact. (UR_2).

This shall certainly take effect on liquid film behaviour over the tooth

surface. In fact, the curves of CF and PF factors are substantially linked to the impact phenomenon. As discussed above, when the injection angle increases the torque values go down, especially in the maximum values, meaning that the momentum transfer occurs more gradually. This leads to a reduction of the forces exchange during the impact phase, therefore the oil expansion on the tooth surface diminishes, as well as the coverage factor. In addition, a lower expansion of the lubricant implies a higher oil film thickness, increasing the amount of the lubricant which is not in direct contact with the tooth surface. Such a oil, subjected to significant centrifugal forces, flows over the underlying layer moving away from the tooth surface, thereby reducing the penetration factor.

These observations also applies to results achieved by the simulations having the velocity coefficient equal to UR_2. The curves of CF and PF factors resulting by such simulations are reported in Figure 3.37 and 3.38, respectively. The greatest effect of an higher injection velocity is the increase of both coverage and penetration factors, whereas the shape of curves is about the same.

To summarize the information given by CF and PF curves, the integral mean value of these curves is reported in Figure 3.39, as a function of on both the angle and velocity of injection; the average values have been calculated in the dimensionless time interval [0.2, 1].

It can be seen how, for both the injection velocities, the coverage factor increases with the injection angles of 0.33 and 0.66, while decreases with $\alpha = 1$. Concerning the lower injection velocity, the CF shows a maximum for $\alpha = 0.66$: in detail, a small increase of 1 % is observed by passing from $\alpha = 0$ to $\alpha = 0.33$, hence an improvement of 18 % for $\alpha = 0.66$, finally a reduction of 19 % with the maximum injection angle. The penetration factor instead is a decreasing function of the injection angle, in both the oil jet velocities. In particular, the reduction is more important in the simulations with the lower injection speed; in fact, passing from $\alpha = 0$ to $\alpha = 1$, the mean value of PF reduces of 44 % in that case, while a reduction of 27 % is achieved when the velocity coefficient is fixed to UR_2.

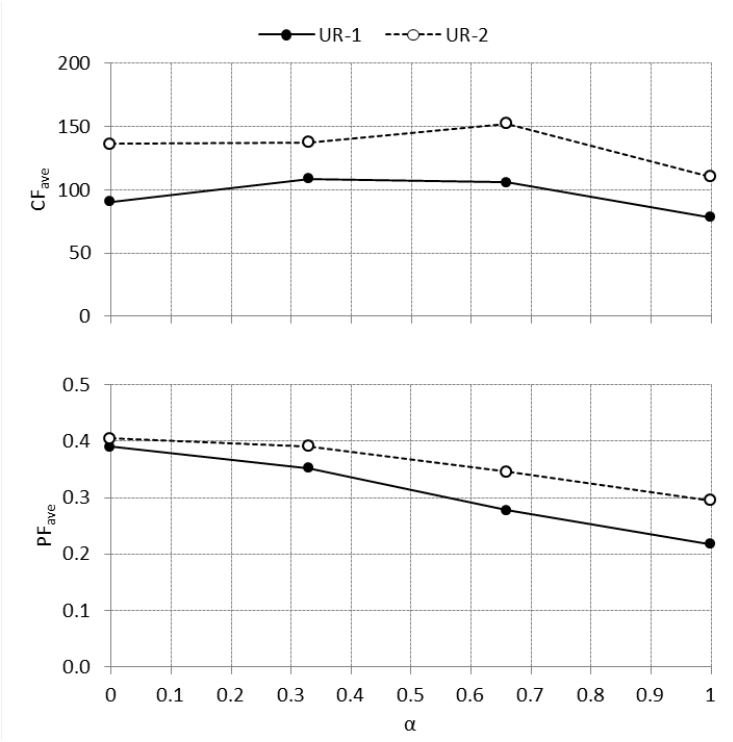

Figure 3.39: Integral mean value of Coverage and Penetration Factors, evaluated in the normalised time interval [0.2 , 1], as function of both oil jet inclination and injection velocity.

To conclude, in Figure 3.40 the mean value of the resistant torque depending on the angle and injection velocity is presented again. By observing the results, it can be deduced that the optimum configuration to be adopted in the oil jet lubrication system is the configuration with an injection angle equal to 0.66. In fact, especially when the higher oil jet velocity is used, it is the best possible compromise between coverage factor, penetration factor and resistant torque.

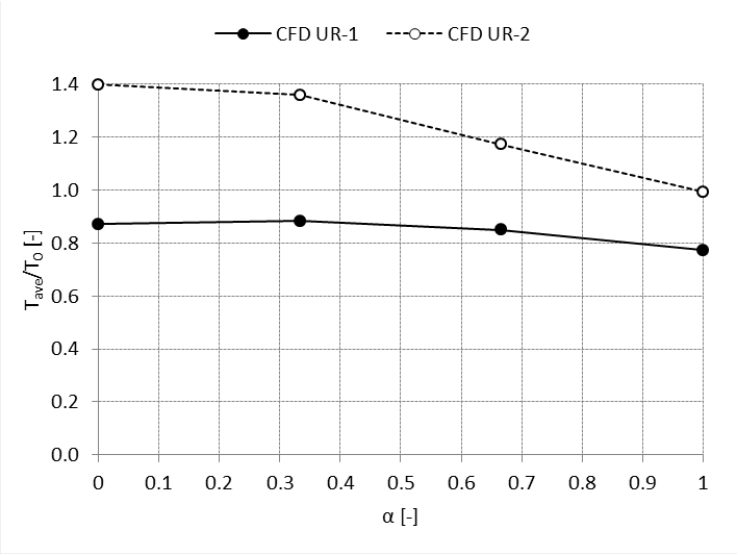

Figure 3.40: Integral mean value of resistant torque, evaluated in the normalised time interval [0.2 , 1], as function of both oil jet inclination and injection velocity.

3.6 Concluding remarks

A comprehensive numerical study of a single oil jet impinging radially on a single high speed gear has been carried out using VOF method. The adapting mesh feature, available in the commercial code ANSYS Fluent, has been exploited, developing hybrid adaptation functions to confine the adaptation to specific domain regions. A global sensitivity analysis of grid adaptation strategy and model parameters was carried out. The level of refinement adopted for the near wall region is the parameter that mainly affects the simulation results, while the effect of other computational parameters is less significant. Thus a robust numerical setup has been defined. After that, several simulations varying the oil injection angle have been performed, in order to evaluate how this parameter affects the

resistant torque and the lubrication performance. The main conclusions arising from this research are summarized as followings:

- In oil jet lubrication method the mechanism which mainly contributes to the resistant torque is the pressure distribution on the tooth flank resulting from the oil jet impact, while the shear forces contribution is negligible. The resistant torque, and hence the correlated power loss, is a function of both oil jet inclination and injection velocity. The mean value decreases when the angle increases, whereas it increases as the injection velocity rises. As regards the peak value, it is about ten times the mean one; regardless of the injection velocity, the maximum torque value is achieved when the lubricant is injected with the same inclination of the pressure angle of the gear. A further increase of the oil jet inclination leads to a more gradual momentum transfer between the gear teeth and lubricant, which lead to a reduction of the torque peak value.

- A very good agreement between simulation results and 0D-Model predictions has been assessed. In fact, the 0D-Model is able to well reproduce the dependency of the average torque from the injection velocity and inclination angle. Therefore such a formulation represents a valuable tool to be exploited in industrial design process of high speed gearboxes.

- The behaviour of the oil-film on the tooth surface has been investigated, achieving very useful information for gearbox designers. It has been shown that a thin oil film is generated on the tooth face as result of the oil jet impact. Such a film expands with high velocity both in axial and radial direction, prevalently toward the tooth root. Furthermore, it has been shown how the film which moving into the tooth space, crosses the tooth root, and climbs the opposite tooth face mainly because of centrifugal forces which pumping the oil film toward the gear top land, where it is expelled in radial direction. The lubrication performance have been considered by evaluating the coverage of the tooth surface provided by the oil film, as well as

the lubricant penetration into the tooth space.

- VOF simulations have allowed to establish an optimum configuration for the oil jet lubrication system, by evaluating whereby injection angle is the best possible compromise between coverage factor, penetration factor and resistant torque. This is the configuration having an injection angle equal to 0.66.

Concerning the state of art for the oil jet lubrication simulation, this research constitutes a significant step forward in this field, being one of the first in literature which provides detailed insight on the physic of such a lubrication method.

Chapter 4

Experimental validation of numerical models

This chapter deals with the preliminary comparisons between the numerical results and the measurements performed on the High Speed Test Rig, which was designed and manufactured in the framework of this research. The test rig, installed in the facility at University of Florence, is a result of a collaboration between the Department of Industrial Engineering of the University of Florence and GE Avio S.r.l, global leader in designing and manufacturing of power gearboxes for aero-engine applications.

Several objectives are related to this experimental survey, such as:

- deepen the knowledge of fluid-dynamic power losses in gearing systems, operating in a relevant air/oil mixture;
- detect and analyse the sources of losses correlating them with gear parameters;
- provide a wide experimental database to carry out comparisons with advanced CFD models and assess their accuracy and reliability;
- validate CFD models developed during the research activity, both in terms of fluid dynamic losses and flow field reproduction.

In this chapter the test rig layouts and measurement devices will be

presented. In a second part, the description will be focused on the windage measurements, by comparing outcomes with the correlations reported in chapter 2. After that, the data concerning the oil jet lubrication tests will be presented, in particular the pictures taken by a high speed camera will be discussed and compared with VOF simulation results.

4.1 Test rig layout

As depicted in Figure 4.1 the test facility consists of an electric motor which drives a shaft on a couple of ball bearings, installed within a bearing chamber outside the test box. The test gear is fitted at one free-end of the

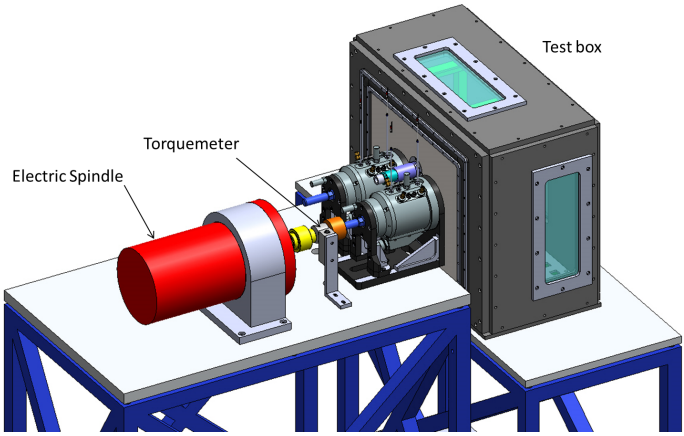

Figure 4.1: High speed test rig layout.

shaft, and the other free-end is used for torque measurement by an high accuracy torque sensor, also be able to measure the speed of rotations. The torque meter is connected to the high speed motor and to the input shaft by means of elastic couplings. The Torque sensor has bearing-less design, suitable for high-speed applications, with a capacity of rated to 10 Nm and a maximum rotating speed of 30000 rpm. It is characterised by $\pm$ 0.1 % full scale accuracy, 16-bit resolution and 10 kHz sample rate.

As shown in Figure 4.2, the test rig has a driven shaft which is not connected to a mechanical load or a brake system, but it is free to rotate on a couple of ball bearings, which are installed in a bearing chamber identical with that of the drive shaft; the test gear is mounted at one free-end of the shaft. A dedicated hydraulic system lubricates and cools continuously both the bearing chambers, to control operating temperature of bearings, which is kept nearly steady during the tests. This allows to maintain as constant as possible the bearing losses when the facility works at fixed rotating speed.

The high speed motor is an electric spindle with hybrid ceramic bearings, maximum speed of 15000 rpm, power 27 kW and maximum torque of 32 Nm. The motor can turn in both ways. The device is equipped with an external inverter to set the required operating speed, moreover it is provided by a liquid cooling system with external chiller unit for temperature control.

The gears to be tested are contained into a test box, as visible in Figure 4.2. This is composed by a steel frame on which removable steel plates are fastened by bolts. Moreover, the test cell is sealed from the external environment by appropriate sealings. The box is linked to a vacuum system which controls the pressure value within the chamber, with a view to asses how the fluid dynamic losses are affected by such a operating parameter. In more details, pressure can be adjusted from 1 atm to 10000 Pa, representative values of those tested by gearboxes on aero-engines. Furthermore, the test box is equipped with large optical accesses made of borosilicate glass, in order to perform a fluid-dynamic characterization by means of high speed visualizations and PIV measurements.

A spray bar is installed inside the test cell: this device creates small oil jet directed toward the gear tooth surfaces, for providing the necessary lubrication. A specific oil system feeds the spray-bar, allowing an accurate check of operating temperature and pressure, thus controlling the oil jet injection velocity.

In order to analyse each fluid dynamic loss individually, the test rig was designed to operate in two configurations:

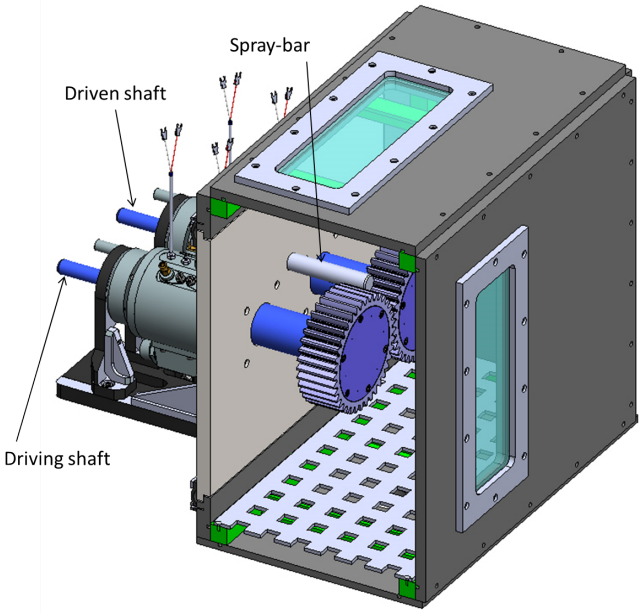

Figure 4.2: Test cell layout.

- Couple of Gears
- Single Gear

In the former setup, driving and driven shafts are installed. With this configuration both windage and meshing losses occur simultaneously, hence the different contributions of such mechanisms on the total power loss cannot be obtained. In the Single Gear layout, only the driven axis is installed and therefore just one gear is present in the test cell.

The experimental surveys reported in this chapter were obtained with the test rig in the Single Gear configuration. In such a layout, the windage losses relating to one gear may be analysed, as well as the oil jet lubrication mechanism. The tested wheel was a spur gear having dimensions typical of power gearboxes.

For isolating the net contribution of windage losses, the power loss achieved without the wheel installed were subtracted from the total system loss. To do this, a characterization of the viscous losses of bearings has been performed, by varying the speed of rotation, the pressure within the test cell and the temperature of the oil system adopted in bearings lubrication.

4.2 Measure of windage power losses

A series of test with the Single Gear layout were performed, with the aim of measuring windage losses of a single gear, by varying the speed of rotation and the pressure level within the test cell. The measures were performed in an oil free environment, by removing the spray-bar (see Figure 4.3). Five speed of rotations and three pressure levels were tested,

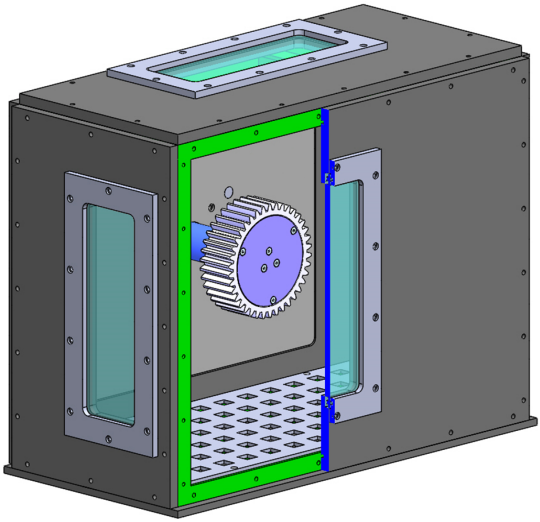

Figure 4.3: Test cell layout for windage measurements.

for a total of 15 test points. Concerning rotating speed, the maximum value was consistent with typical high-speed gearboxes.

Before conducting a test campaign, the rig was started and warmed up at maximum rotational speed until all temperatures, pressures and lubricant flow rates in the bearings chamber had reached a steady condition.

In each test, the speed of rotation was kept constant until the torque reached a steady mean value, then the torque value, air pressure and temperature within the test cell were acquired. Pressure and temperature were measured respectively by means of a static pressure tap and a thermocouple, thus the air density was calculated for each test point.

As far as the uncertainty of torque measurements is concerned, it was estimated to be within ± 10 % related to the averaged values. The average experimental uncertainty has been computed through the procedure proposed by Bell [74], based on the Kline and McClintock method [75]; this estimation include the effects of calibration and data post-processing. The uncertainty is inversely proportional to the gear speed and directly proportional to the pressure within the box, therefore it is minimum at the maximum rotating speed and at the lower pressure. Tests were repeated several times in order to confirm the repeatability of results.

Pressures and rotating speeds reported in the current section have been normalised, respectively, by maximum values of pressure and speed reached in the experimental survey.

In Figure 4.4, the windage power losses resulting by the experiment have been compared with the values predicted by Diab correlation given by Equation 2.1, which is reported below:

$$P_{Diab} = \frac{1}{2} C_t \rho \omega^3 R^5$$

where C_t is given by the Equation 2.3, resulting from the fluid flow analysis (see section 2.1.1). Such a correlation is valid for a single gear rotating in air without enclosure. The power data have been normalised by the value provided by the Diab's correlation at the maximum speed of rotation tested in the experimental campaign.

Looking at the results, it can be noticed how the Diab's correlation overestimates the experimental data in every test points. The formula

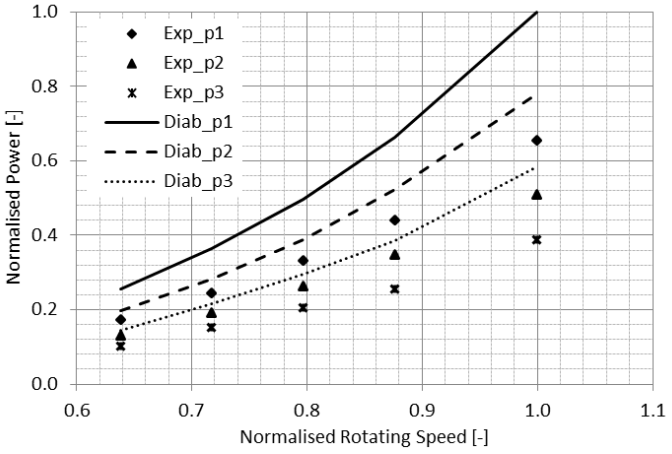

Figure 4.4: Comparison between windage power losses measurements and the values predicted by the Diab's correlation.

replicates the experimental data trend, while the absolute values are visibly higher. In detail, at the highest pressure (p1) as well as at the middle one (p2), the correlation overestimates the measurements of about 51 %, and at the lowest pressure level (p3) of about 47 %.

As already discussed, the dimensions of the casing have a direct impact on windage power loss. By conserving the angular momentum of the flow near the teeth, the fluid progressively gains momentum, leading to a rotating flow field within the system. This generates a centripetal pressure gradient that reduces the depression in the tooth space. As a result, the power demanded to the gear for accelerating the air decreases (see section 2.4). This behaviour, that has been numerically assessed, seems to occur also in the experiment under investigation, although the casing geometry is a box instead of a cylinder. Unfortunately PIV measurements are not yet available for further analysing the phenomenon, thus the rotating flow field within the system cannot be verified.

The experimental results have been exploited for testing the improved

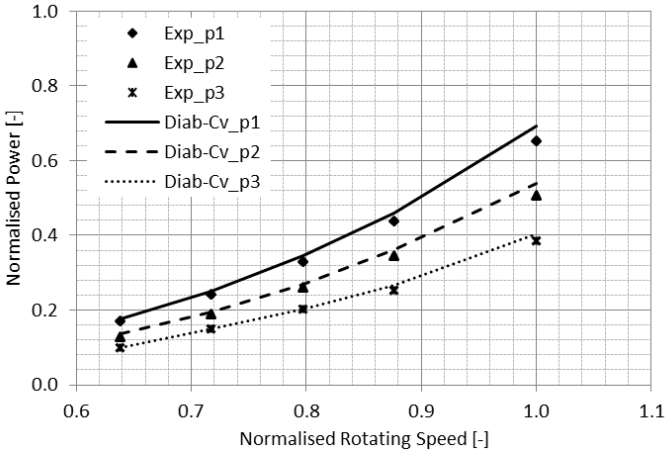

Figure 4.5: Comparison between windage power losses measurements and the values predicted by the modified Diab's correlation.

version of Diab formulation developed in this research and discussed in section 2.4.3. Such a correlation, expressed by Equations 2.11, is reported below

$$P_{Cv} = C_v \cdot P_{Diab}$$

The volume correction parameter (C_v) was defined as (Equation 2.10):

$$C_v = m{V_r}^n$$

where V_r is the ratio between the volume of fluid enclosed between the casing and the rotating parts.

The results are represented in Figure 4.5: a very good agreement with the experimental measurements is clear. Windage power losses predicted by the improved correlation are slightly higher than the measurements, with differences that are always lower than 5 %. Although this result does not represent a complete validation of the correlative approach developed in this research, it is certainly a first evidence of the predictive capability

of such a formulation.

4.3 Visualization of the Oil jet lubrication

An experimental campaign has been performed to look into the oil jet lubrication method, with the aim of providing a preliminary validation of VOF simulations presented in the section 3.4.

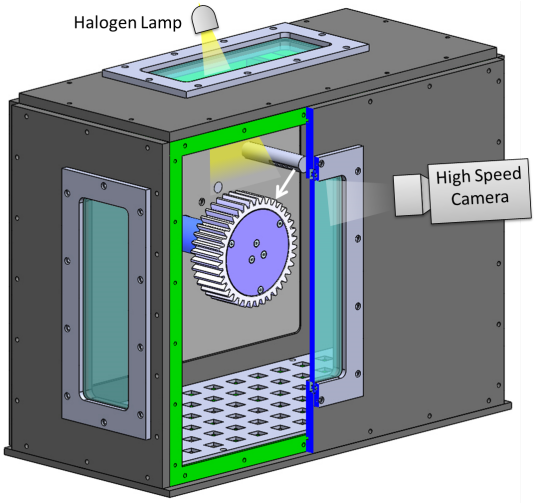

Figure 4.6: Test cell layout for the oil jet lubrication visualization.

As shown in Figure 4.6, the facility was configured in the Single Gear layout, with the spray-bar installed at 75 jet diameters from the gear top land. The oil jet axis was oriented perpendicularly to the wheel axis, while axial position of the spray bar was fixed so that the oil stream impinges the center of the tooth face. The lubricant used in the tests was the hydraulic oil ISO 46, whose density and dynamic viscosity were known. The window located on the upper cover of the box was exploited for illuminating the test using a halogen lamp, whereas the frontal optical access was used to take pictures of the phenomenon. A 4 megapixel high

speed camera was adopted, able to shoot over 800 frames-per-second by a maximum resolution of 2560 x 1600 pixels (10 μm pixel size), while at reduced resolution of 128 x 8 pixels the frame rate reaches up to 325,000 Hz.

In section 3.1.3 the operating conditions adopted in VOF simulations were explained, analysing the main dimensionless parameters useful for describing the oil jet behaviour. To make the discussion clearer, such parameters are listed below:

- $UR = \frac{U_j}{U_p} = 0.25$
- $q = \frac{\rho_j U_j^2}{\rho_{air} U_{air}^2} = 644$
- $We_{cf} = \frac{\rho_{air} d_j U_p^2}{\sigma} = 36$
- $We_j = \frac{\rho_j d_j {U_{imp}}^2}{\sigma} = 3.9 \cdot 10^5$
- $Re_j = \frac{\rho_j d_j U_{imp}}{\mu_j} = 3.2 \cdot 10^4$

where U_{imp} is the oil jet impact velocity $U_{imp} = \sqrt{{U_j}^2 + {U_p}^2}$.

The velocity coefficient (UR) controls the oil jet impingement depth, hence the amount of oil involved in the momentum transfer with the teeth. The lubricant has to cross a rotating air flow before hitting the gear teeth: as shown in section 3.3.1, the airflow is characterized by a tangential velocity of the same order of the pitch line velocity, thus the problem can be treated as an injection of liquid into a high-speed cross flow. For such issue, the liquid column trajectory, breakup distance and height, are governed by the liquid to gas momentum ratio (q), whereas the crossflow Weber number (We_{cf}) assesses the relative magnitude between the aerodynamic forces acting on the liquid stream and the surface tension forces, therefore it controls the deformation and breakup's regime. Concerning the oil jet impact on the teeth, this is characterized by the jet Weber number (We_j) and jet Reynold number (Re_j).

The test rig was commissioned a few weeks before of the experimental campaign under discussion, therefore it was not fully operational. In fact, the oil injection speed could not be varied, and it was about the 34% of value adopted in VOF simulations. On that basis, the speed of rotation

of the gear was reduced to achieve similitude for the velocity coefficient. As far as the pressure level in the test cell is concerned, it was set at atmospheric value, achieving similitude for the crossflow Weber number (We_{cf}), as result of the air density increase. Due to the latter similitude, it is expected that the oil stream in the experimental test does not deform or break up before it reaches the teeth of the gear, as predicted by VOF simulations.

With regard to the liquid to gas momentum ratio (Equation 3.4) in the experimental test it was equal to 55, sensibly lower than 644 which was adopted in the VOF simulations, but anyway, high enough to ensure that oil reaches the tooth surface.

Concerning the impact phase, in the experiment both the impact Reynolds and Weber numbers assume values about one order of magnitude lower than those in the simulations:

- $Re_j = 7.9 \cdot 10^3$
- $We_j = 3.0 \cdot 10^4$

As a consequence the forces exchanged during the impact phase decrease, having effect on the liquid film growth on the tooth surface. In particular, a reduction of the oil film expansion is expected, as well as an increase of thickness.

In the experimental configuration the average torque predicted by the 0D-model, presented in section 3.1.2, is about 93 % lower than that calculated by VOF simulation. Therefore the measure of such a torque was difficult and not very significant, since the expected value was equivalent to the measurement uncertainty of the torque sensor. For this reason a quantitative comparison between VOF simulations and experiments was not performed, thus the investigation was focused on visualization tests.

Before to inject the oil, the rig was started and kept at constant speed until the aerodynamic field in the system reached a steady condition, as verified by monitoring the pressure and temperature within the test cell. After that, the oil was injected and pictures of the phenomenon were taken using the high speed camera, which was previously placed and set

up for framing the surface of impact. The "Image Based Auto Trigger" feature was exploited to synchronize the acquisition with the time at which the oil jet entered into the picture. The ratio between the camera acquisition rate and the tooth passing frequency was fixed about 10.

In Figures 4.7 and 4.8 the lubricant evolution predicted by VOF simulation is compared with the pictures taken by the high speed camera; in the left column the experimental images are reported, whereas on the right the numerical ones. A qualitative good agreement between the simulation and the experiment is clear.

By analysing the experimental results, it can be observed how the oil stream does not deform before reaching the gear teeth, as predicted by VOF simulation. As a consequence, also the impingement penetration depth is well reproduced, as shown in Figure 4.7-a. When the oil jet hits the tooth surface it forms a thin oil film which expands with high velocity, meanly toward the tooth root. The first instants of film formation are shown in Figure 4.7-b: the axial and radial expansion of the liquid film are very similar between simulation and experiment, as well as the shape of the jet base which is placed over the gear top land.

As already discussed in section 3.4 concerning the VOF results, when the oil jet is passing over the gear top land, the lubricant does not impinge on the gear but feeds a suspended film that flies over the gear top land; the jet remains connected to the oil on the tooth flank by means of the film. This seems to be confirmed by the experimental data, in fact by observing the Figures 4.7-c and 4.8-d, although the gear top land is not sufficiently enlightened and consequently the absence of the oil film on such a surface cannot be fully verified, the formation of the suspended oil film is evident; moreover the shape of liquid in the experiment is very similar to the numerical pictures.

In both experimental and numerical outcomes reported in Figures 4.8-d and 4.8-e, how the suspended film moves away from the gear tooth meanly in radial direction and spreading in the axial direction can be observed. However some ligaments preserve the oil connection with the tooth surface. When the oil stream is located over the tooth crest, the

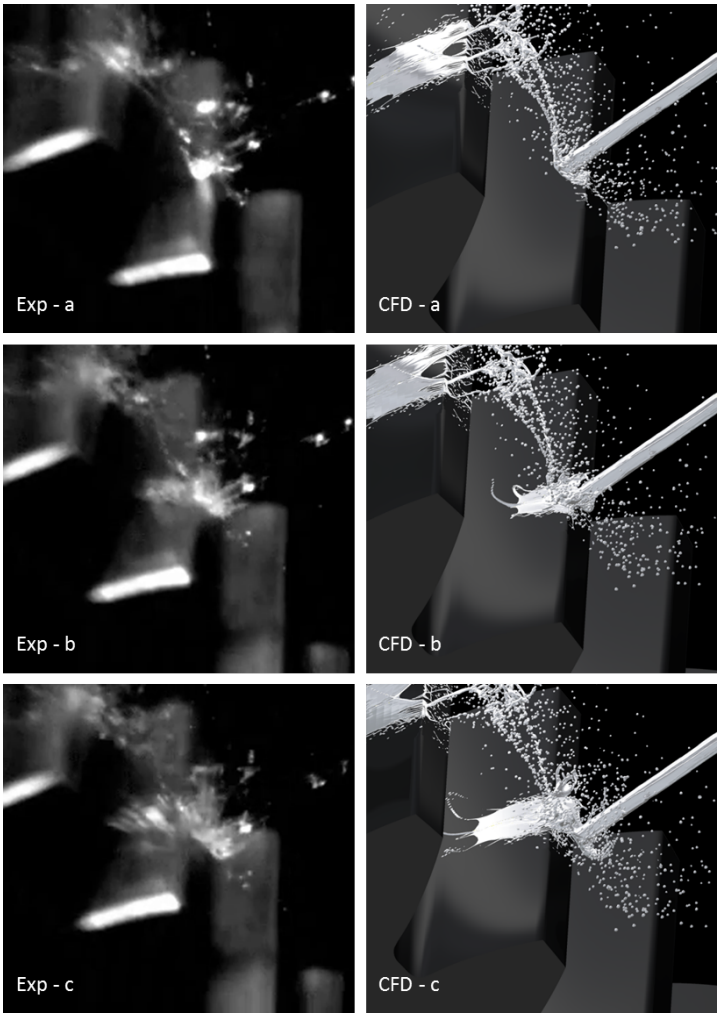

Figure 4.7: Comparison between the oil behaviour predicted by VOF simulation with the pictures taken by the high speed camera: pictures a, b, and c.

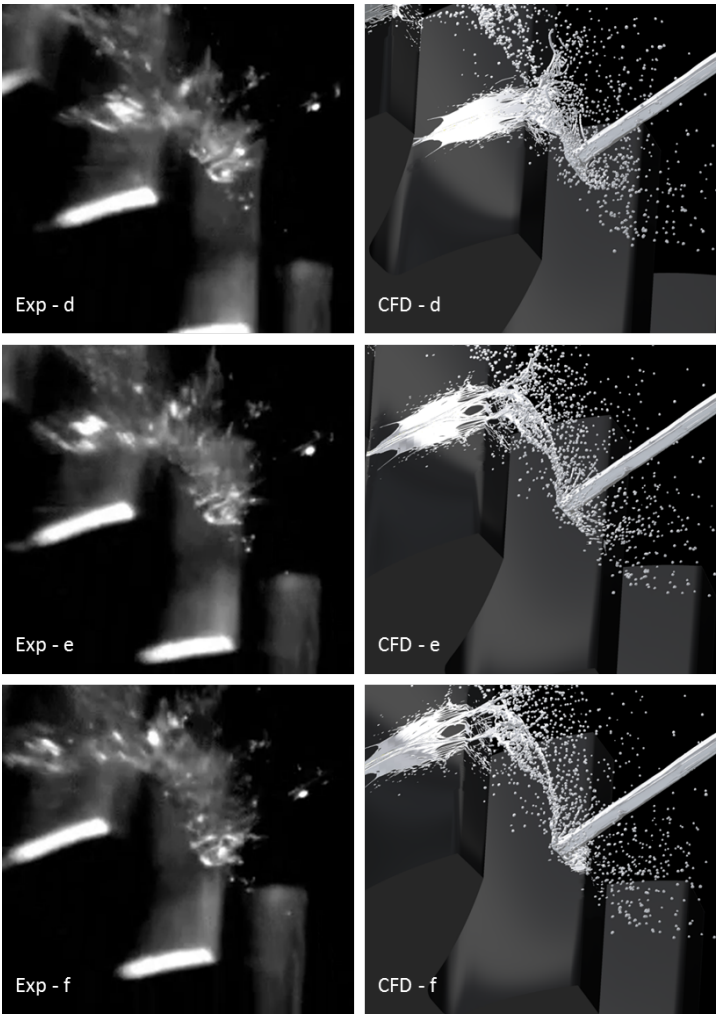

Figure 4.8: Comparison between the oil behaviour predicted by VOF simulation with the pictures taken by the high speed camera: pictures d, e, and f.

lubricant that is reaching the jet base feeds the suspended film; this phenomenon also occurs while the oil jet is passing over the tooth space, as can be seen by the liquid stream that developing in tangential direction and connects the jet with the oil located on the tooth flank. As shown in Figures 4.8-e and 4.8-f, at this stage, the main difference between experiment and simulation is a larger number of ligaments and droplets in the simulations with respect to the experimental data, as well as a higher radial position assumed by the oil stream. Both differences may be partially attributed to a sensibly higher centrifugal field experienced by the liquid in the CFD calculation. In fact, the radial component of the speed gained by the lubricant which moves away from the teeth surface is due to the centrifugal acceleration acting on the fluid particle on the tooth surface. The magnitude of such acceleration is $\omega^2 r$, but the angular velocity in the test is 1/3 of that in the simulation, therefore, at equal radius, the intensity of the centrifugal force is 9 times greater in CFD case. As a result, the oil above the gear top land moves away from such a region with a greater radial velocity in VOF results, dragging all the linked liquid toward the radial direction, thus promoting the liquid film breakup.

Concerning the development of the liquid film on the tooth flank, in the simulation it expands quickly, and the maximum coverage is reached in Figure 4.8-d. This does not happen for the experiment, in fact the oil is still expanding in in Figure 4.8-f. Moreover, it can be observed how, in the experimental case, the film expansion occurs meanly with oil suspended above the tooth surface, and the oil film seems attached only at the impact point. Such discrepancies may be due to multiple reasons. In the experiment both liquid Reynolds number and liquid Weber number assume values about one order of magnitude lower than in the simulations, and this certainly has effect on the oil film development. This also applies to the liquid to gas momentum ratio, that in the experimental test is equal to 55, sensibly lower than 644 adopted in the VOF simulation. Moreover it is not negligible the surface roughness of the gear teeth (1.6 μm), which is distant by the smooth wall condition adopted in the simulation, as well

as the uncertainty on the value of the surface tension coefficent.

In conclusion, a qualitative good agreement between VOF simulation results and the experimental survey has been verified. In fact, the numerical model has proved to well reproduce the main features of the oil jet lubrication method. Unfortunately torque measurements are not yet available, hence a quantitative comparison in terms of resistant torque cannot be verified. Although the achieved results do not represent a complete validation of the VOF approach developed in this research, these are certainly a first evidence of the predictive capability of the developed methodology.

Conclusions

The research activity presented in this dissertation is aimed at defining CFD methodologies to be used in the comprehension of fluid-dynamic losses in gearbox systems for aero-engine applications. The developing of physical knowledge on such losses is indeed mandatory to enhance the efficiency of epicyclical gearbox adopted in the Geared Turbofan engines. In fact, the implementation of this engine architecture for high thrust engine class, which would allow a significant reduction of specific fuel consumption as well as noise and emissions, is strictly depending on the gearbox performance improvement.

This activity has been carried out within a collaboration between the Department of Industrial Engineering of the University of Florence and GE Avio S.r.l., aimed at analysing, both experimentally and numerically, the fluid-dynamic losses in high-speed gearboxes.

A global study of the multiphase flow within the epicyclic gear train would be too complex and not useful in the understanding of the various loss mechanisms, therefore each one should be studied individually, by turning to simpler geometries. In this work, the power losses related to the windage phenomena and to the oil jet lubrication method were numerically investigated in a simplified configuration consisting of a single high speed spur gear.

The windage losses of a spur gear in free and enclosed configuration have been analysed by means of RANS simulations. At first, the capability of using a CFD code to calculate windage power losses of a single spur gear

rotating in air has been assessed, using ANSYS FLUENT. The experiment of Diab et al. [13] has been computationally replicated. Steady state RANS calculations in the rotating frame of reference have been performed with conventional eddy viscosity models. The numerical results have been compared with experimental data. CFD analysis has exhibited a very good agreement with experiments for all of the rotating speeds. Especially the predictions obtained with $k-\epsilon$ model were very close to the measurements, with relative error that never exceeds 5 %. The RNG $k-\epsilon$ and $k-\omega$ SST models had a tendency to underestimate windage power losses, in particular at lower speeds. The resulting numerical setup has been adopted to simulate a single gear enclosed within seven different cylindrical casing, in order to assess the effect of the boundary walls on windage power losses.

In all the investigated configurations, the pressure field was the dominant factor for the windage losses, while the contribution of the shear forces was about of 10 %. However viscous contribution with respect to the pressure one starts to increase, as the axial and radial gaps between the gear and the casing become comparable to the tooth height. The windage losses reduce when the gear was enclosed within a casing, which preserves the angular momentum of the flow, so that the fluid progressively gains momentum, leading to a rotating flow field within the system. This generates a centripetal pressure gradient that reduces the depression in the tooth space. As a result, the power required to accelerate the flow decreases.

In the light of the relationship between the windage power losses and the volume of fluid within the system assessed for the enclosed geometries, the Diab correlations has been revised by introducing an appropriate parameter for including the effects of a casing on the power losses prediction. The modified formulation has been tested with the measurements performed on the High Speed Test Rig, installed in the facility at University of Florence, which was designed and manufactured in the framework of this research. A very good agreement with the experimental data has been observed. Although this result does not

represent a complete validation of the correlative approach developed in this research, in fact further investigation are needed, it is certainly a first evidence of the predictive capability of such a formulation, representing a useful and simple tool to be employed in industrial design process.

Concerning the numerical investigation of the oil jet lubrication, a comprehensive numerical study of a single oil jet impinging on a high-speed spur gear has been carried out using the Volume of Fluid method. The simulation of such a system is very challenging, because involving transient multiphase flows, moving boundaries, and large three-dimensional domains which lead to high computational effort. For these reasons, numerical studies on this issue, which provide detailed insight on the physic of the oil jet lubrication, are not present in the open literature.

This research is aimed at improving the description of the complex physical phenomena characterizing the oil jet lubrication and the resulting liquid film formation in high speed gearing systems, within the context of transient RANS calculations. However this approach requires a very fine mesh in the liquid region, leading to very high computational efforts. Exploiting the adapting mesh feature, available in the commercial code ANSYS Fluent, a strategy for local grid refinement and coarsening has been developed to confine the adaptation to selected domain regions, heavily reducing the numerical effort. A global sensitivity analysis of grid adaptation strategy and model parameters was carried out. The level of refinement adopted for the near wall region was proved to be the parameter that mainly affects the simulation results, while the effect of other computational parameters was less significant. Thus a robust numerical setup was defined. After that, several simulations varying the oil injection angle have been performed, in order to evaluate how this parameter affects the resistant torque and the lubrication performance.

Very useful information about the oil jet lubrication arising from this research. In the oil jet lubrication method the mechanism which mainly contributes to the resistant torque is the pressure distribution on the tooth flank resulting from the oil jet impact, while the shear forces contribution is negligible. The resistant torque, and hence the correlated power loss, is

a function of oil jet inclination and injection velocity. The mean value decreases when the angle increases, whereas it increases as the injection velocity rises. As regards the peak value, it is about ten times the mean one; regardless of the injection velocity, the maximum torque value is achieved when the lubricant is injected with the same inclination of the pressure angle of the gear. A further increase of the oil jet inclination leads to a more gradual momentum transfer between the gear teeth and lubricant, which lead to a reduction of the torque peak value.

The behaviour of the oil-film on the tooth surface has been investigated, achieving very useful information for gearbox designers. It has been shown that a thin oil film is generated on the tooth face as result of the oil jet impact. Such a film expands with high velocity both in axial and radial direction, prevalently toward the tooth root. Furthermore, it has been shown how the film which moving into the tooth space, crosses the tooth root, and climbs the opposite tooth face mainly because of centrifugal forces which pumping the oil film toward the gear top land, where it is expelled in radial direction. The lubrication performance have been considered by evaluating the coverage of the tooth surface provided by the oil film, as well as the lubricant penetration into the tooth space. VOF simulations have allowed to establish an optimum configuration for the oil jet lubrication system, by evaluating whereby injection angle is the best possible compromise between coverage factor, penetration factor and resistant torque.

A very good agreement between simulation results and 0D-Model predictions has been assessed. In fact, the 0D-Model, a simple formulation developed in this work for the prediction of the average power loss due to the oil jet lubrication, is able to well reproduce the dependency of the average torque from the oil jet inclination and injection velocity. Therefore such a formulation represents a valuable tool to be exploited in industrial design process of high speed gearboxes.

Finally, a preliminary comparison between VOF results and experimental data resulting by the High Speed test rig was carried out. The test bench was commissioned few weeks before of the experimental campaign

under discussion, therefore it was not fully operational. In fact, the oil injection speed could not be varied and it was about the 34% of value adopted in VOF simulations. In such conditions, the torque due to the oil jet was too low, by providing a value equivalent to the measurement uncertainty of the torque sensor. For this reason a quantitative comparison between VOF simulations and experiments was not performed, thus the investigation was focused on visualization tests. A qualitative good agreement between VOF simulation and experimental survey has been observed. In fact, the numerical model has shown to well reproduce the main features of the oil jet lubrication method. Although the achieved results do not represent a complete validation of the VOF approach developed in this research, these are certainly a first evidence of the predictive capability of the developed methodology.

This study has allowed the evaluation of the power losses due to oil jet cooling methods, as well as the lubrication performance of such a system, developing a more in-depth understanding of the oil-gear interaction phenomena. Concerning the state of art for the oil jet lubrication simulation, this research constitutes a significant step forward in this field, being one of the first in literature which provides detailed insight on the physic of such a lubrication method.

Bibliography

[1] Dewanji, Dipanjay, Rao, G Arvind, and van Buijtenen, Jos. Feasibility study of some novel concepts for high bypass ratio turbofan engines. In *ASME Turbo Expo 2009: Power for Land, Sea, and Air*, pages 51–61, 2009.

[2] Farokhi, S. *Aircraft propulsion*. John Wiley & Sons, 2014.

[3] Kurzke, Joachim. Fundamental differences between conventional and geared turbofans. In *ASME Turbo Expo 2009: Power for Land, Sea, and Air*, pages 145–153, 2009.

[4] Kyprianidis, Konstantinos G. Future aero engine designs: An evolving vision. 2011.

[5] Visual inspections of commercial jet engines. URL `http://www.olympus-ims.com/en/applications/rvi-passenger-jet-engine`.

[6] Boggia, S and Rüd, K. Intercooled recuperated aero engine. *DGLR Paper*, 179:2004, 2004.

[7] Pure power engine family specifications, . URL `http://www.pw.utc.com`.

[8] Pure power engine features, . URL `http://www.purepowerengine.com`.

[9] Hughes, Chris. Geared turbofan technology, 2010. URL `http://www.aeronautics.nasa.gov/pdf/hughes_green_aviation_summit.pdf`.

[10] Seetharaman, S. and Kahraman, A. Load-independent spin power losses of a spur gear pair: model formulation. *Journal of Tribology*, 131(2), 2009.

[11] Eastwick, C. N. and Johnson, G. Gear windage: a review. *Journal of Mechanical Design*, 130(3), 2008.

[12] Hill, M. J. and Kunz, R. F. A computational investigation of gear windage. *Pennsylvania State University, Philadelphia*, NASA/CR-2012-217807.

[13] Diab, Ville F. Velex P. Y. and Changenet, C. Windage losses in high speed gears - preliminary experimental and theoretical results. *Journal of Mechanical Design*, 126, pp. 903-908, 2004.

[14] Von Kármán, Th. Technical memorandum on laminar and turbulent friction. *National Advisory Committee for Aeronautics Report*, (1092), 1921.

[15] Goldstein, S. On the resistance to the rotation of a disc immersed in a fluid. In *Mathematical Proceedings of the Cambridge Philosophical Society*, volume 31, pages 232–241. Cambridge Univ Press, 1935.

[16] Dorfman, Lev Abramovic. *Hydrodynamic resistance and the heat loss of rotating solids.* Oliver & Boyd, 1963.

[17] Townsend, D. P. *The Design, Manufacture and Application of Gears.* Gear Handbook. McGraw-Hill, New York, 2nd edition, 1992.

[18] Anderson, N. E. and Loewenthal, S. H. *Spur-Gear-System Efficiency at Part and Full Load.* Tech. rep. NASA, 10 Dec. 1979.

[19] Anderson, N. E. and Loewenthal, S. H. Effect of geometry and operating conditions of spur gear system power loss. *Journal of Mechanical Design*, 103, pp. 151-159, 1981.

[20] Dawson, P. H. Windage loss in larger high-speed gears. *Proc. Inst. Mech. Eng., Part A: Power and Process Engineering*, 198(1), pp. 51-59, 2009.

[21] Farrall, Simmons K. Hibberd S. M. and Young, C. Computational investigation of the airflow through a shrouded bevel gear. *ASME Turbo Expo 2005*, 2005.

[22] Winfree, D. D. Reducing gear windage losses from high speed gears. *Proceedings of DETC2000, ASME Power Transmission and Gearing Conference*, 2000.

[23] Al-Shibl, Simmons K. K. and Eastwick, C. N. Modelling windage power loss from an enclosed spur gear. *Journal of Power and Energy*, 2007.

[24] Marchesse, Changenet C. Ville F. Y. and Velex, P. Investigations on cfd simulation for predicting windage power losses in spur gears. *3rd International Conference on Integrity, Reliability and Failure.*

[25] Hill, Kunz R. F. Noack R. W. Long L. N. Morris P. J. M. J. and Handschuh, R. F. Application and validation of unstructured overset cfd technology for rotorcraft gearbox windage aerodynamics simulation. *64th Annual Forum of the American Helicopter Society.*

[26] Hill, Matthew J, Kunz, Robert F, Medvitz, Richard B, Handschuh, Robert F, Long, Lyle N, Noack, Ralph W, and Morris, Philip J. Cfd analysis of gear windage losses: Validation and parametric aerodynamic studies. *Journal of Fluids Engineering*, 133(3):031103, 2011.

[27] Akin, LS. An interdisciplinary lubrication theory for gears (with particular emphasis on the scuffing mode of failure). *Journal of Manufacturing Science and Engineering*, 95(4):1178–1195, 1973.

[28] Townsend, D. P. Lubrication and cooling for high speed gears. Technical Memorandum 87096, NASA, 1989.

[29] Akin, L. S. and Townsend, D. P. Lubricant jet flow phenomena in spur and helical gears. Technical report, Gear Technology, 1987.

[30] Saavedra, Jaime Joaquin. *Effect of jet prandtl number on impingement cooling of rotating bodies.* PhD thesis, Texas Tech University, 1981.

[31] Akin, L. S., Townsend, D. P., and Mross, J. J. Study of lubricant jet flow phenomena in spur gears. Technical Memorandum TM X-71572, NASA, 1974.

[32] DeWinter, A and Blok, Harmen. Fling-off cooling of gear teeth. *Journal of Manufacturing Science and Engineering*, 96(1):60–70, 1974.

[33] El-Bayoumy, E, Akin, Lee S, Townsend, Dennis P, and Choy, FC. The role of thermal and lubricant boundary layers in the transient thermal analysis of spur gears. Technical report, DTIC Document, 1989.

[34] Johnson, G., Chandra, B., Foord, C., and Simmons, K. Windage power losses from spiral bevel gears with varying oil flows and shroud configurations. *Journal of Turbomachinery*, 131(4):041019, 2009.

[35] Li, Li, Versteeg, Henk K, Hargrave, Graham K, Potter, Theo, and Halse, Chris. Numerical investigation on fluid flow of gear lubrication. 2009.

[36] Arisawa, H., Nishimura, M., Imai, H., and Goi, T. CFD simulation for reduction of oil churning loss and windage loss on aeroengine transmission gears. In *ASME Turbo Expo 2009: Power for Land, Sea, and Air*, pages 63–72. ASME, 2009.

[37] Rosen, Moe William. Noises of two spur-gear transmissions. *Noise Control*, 7(6):11–19, 1961.

[38] Diab, Youssef, Ville, Fabrice, Houjoh, H, Sainsot, Philippe, and Velex, Philippe. Experimental and numerical investigations on the air-pumping phenomenon in high-speed spur and helical gears. *Proceedings of the Institution of Mechanical Engineers, Part C: Journal of Mechanical Engineering Science*, 219(8):785–800, 2005.

[39] Wittbrodt, Michael John and Pechersky, MJ. A hydrodynamic analysis of fluid flow between meshing spur gear teeth. Technical report, DTIC Document, 1987.

[40] Houjoh, Haruo, Ohshima, Shun-ichi, Matsumura, Shinji, Takimoto, Takayuki, and Maenami, Kentaro. Dynamic behavior of atmosphere in a tooth space of a spur gear during mesh process from the viewpoint of efficient lubrication. In *Proceedings of DETC'00-8th International Power Transmission and Gearing Conference, Baltimore*, number PTG-14372, 2000.

[41] Houjoh, Haruo, Ohshima, Shun-ichi, Matsumura, Shigeki, Yumia, Yasuhiro, and Itoh, Keiji. Pressure measurement of ambient air in the root space of helical gears for the purpose of understanding fluid flow to improve lubrication efficiency. In *ASME 2003 International Design Engineering Technical Conferences and Computers and Information in Engineering Conference*, pages 957–964. ASME, 2003.

[42] Gorla, Concli F. Stahl K. Höhn B.R. Michaelis K. Schulthei H. C. and Stemplinger, J. P. Hydraulic losses of a gearbox: Cfd analysis and experiments. *Journal of Tribology*, 66:337–344, 2013.

[43] Brennen, Christopher E. *Fundamentals of multiphase flow*. Cambridge University Press, 2005.

[44] Wörner, Martin. *A compact introduction to the numerical modeling of multiphase flows*. Forschungszentrum Karlsruhe, 2003.

[45] Ishii, Mamoru and Hibiki, Takashi. *Thermo-fluid dynamics of two-phase flow*. Springer Science & Business Media, 2010.

[46] Prosperetti, Andrea and Tryggvason, Grétar. *Computational methods for multiphase flow*. Cambridge university press, 2007.

[47] Tryggvason, Grétar, Scardovelli, Ruben, and Zaleski, Stéphane. *Direct numerical simulations of gas–liquid multiphase flows*. Cambridge University Press, 2011.

[48] Tryggvason, Grétar, Bunner, Bernard, Esmaeeli, Asghar, Juric, Damir, Al-Rawahi, N, Tauber, W, Han, J, Nas, S, and Jan, Y-J.

A front-tracking method for the computations of multiphase flow. *Journal of Computational Physics*, 169(2):708–759, 2001.

[49] Sussman, Mark, Smereka, Peter, and Osher, Stanley. A level set approach for computing solutions to incompressible two-phase flow. *Journal of Computational physics*, 114(1):146–159, 1994.

[50] Hirt, C.W. and Nichols, B.D. Volume of fluid (VOF) method for the dynamics of free boundaries. *Journal of Computational Physics*, 39: 201–225, 1981.

[51] Sun, Xiaosong and Sakai, Mikio. Numerical simulation of two-phase flows in complex geometries by using the volume-of-fluid/immersed-boundary method. *Chemical Engineering Science*, 139:221–240, 2016.

[52] Scardovelli, Ruben and Zaleski, Stéphane. Direct numerical simulation of free-surface and interfacial flow. *Annual review of fluid mechanics*, 31(1):567–603, 1999.

[53] Sussman, M. and Puckett, E.G. A coupled level set and volume-of-fluid method for computing 3D and axisymmetric incompressible two-phase flows. *Journal of Computational Physics*, 162:301–337, 2000.

[54] DeBar, R. Fundamentals of the kraken code. *Lawrence Livermore Laboratory, UCIR-760*, 1974.

[55] Noh, William F and Woodward, Paul. Slic (simple line interface calculation). In *Proceedings of the Fifth International Conference on Numerical Methods in Fluid Dynamics June 28–July 2, 1976 Twente University, Enschede*, pages 330–340. Springer, 1976.

[56] Gueyffier, Denis, Li, Jie, Nadim, Ali, Scardovelli, Ruben, and Zaleski, Stéphane. Volume-of-fluid interface tracking with smoothed surface stress methods for three-dimensional flows. *Journal of Computational Physics*, 152(2):423–456, 1999.

[57] Rudman, Murray. Volume-tracking methods for interfacial flow calculations. *International journal for numerical methods in fluids*, 24(7):671–691, 1997.

[58] Youngs, David L. Time-dependent multi-material flow with large fluid distortion. *Numerical methods for fluid dynamics*, 24:273–285, 1982.

[59] Lakehal, D, Meier, M, and Fulgosi, M. Interface tracking towards the direct simulation of heat and mass transfer in multiphase flows. *International Journal of Heat and Fluid Flow*, 23(3):242–257, 2002.

[60] Ubbink, O. *Numerical Prediction of Two Fluid Systems With Sharp Interfaces*. PhD thesis, Imperial College of Science, Technology and Medicine, London, England, 1997.

[61] Butt, Hans-Jürgen, Graf, Karlheinz, and Kappl, Michael. *Physics and chemistry of interfaces*. John Wiley & Sons, 2006.

[62] Brackbill, J. U., Kothe, D. B., and Zemach, C. A continuum method for modeling surface tension. *Journal of Computational Physics*, 100: 335–354, 1992.

[63] Lakehal, Djamel. On the modelling of multiphase turbulent flows for environmental and hydrodynamic applications. *International Journal of Multiphase Flow*, 28(5):823–863, 2002.

[64] Wilcox, David C et al. *Turbulence modeling for CFD*, volume 2. DCW industries La Canada, CA, 1998.

[65] Pope, Stephen B. *Turbulent flows*. Cambridge university press, 2000.

[66] Versteeg, Henk Kaarle and Malalasekera, Weeratunge. *An introduction to computational fluid dynamics: the finite volume method*. Pearson Education, 2007.

[67] *ANSYS® FLUENT, Theory Guide, Release 16.0.*

[68] Yakhot, V., Orszag, S. A., Thangam, S., Gatski, T. B., and Speziale, C. G. Development of turbulence models for shear flows by a double expansion technique. *Physics of Fluids A: Fluid Dynamics (1989-1993)*, 4(7):1510–520, 1992.

[69] Menter, F. R. Two-equation eddy-viscosity turbulence models for engineering applications. *AIAA Journal*, 32(8):1598–1605, 1994.

[70] Wu, Kirkendall K.A. Fuller R.P. P.K. and Nejad, A.S. Breakup processes of liquid jets in subsonic crossflow. *Journal of Propulsion and Power*, 13(1):64–73, 1997.

[71] Wu, Kirkendall K.A. Fuller R.P. P.K. and Nejad, A.S. Spray structures of liquid jets atomized in subsonic crossflows. *Journal of Propulsion and Power*, 14(2):173–81, 1998.

[72] Mazallon, Dai Z. J. and Faeth, G.M. Primary breakup of nonturbulent round liquid jets in gas crossflows. *Atomization and Sprays*, 9(3): 291–311, 1999.

[73] Dawson, P. H. High speed gear windage. *GEC Review*, 43, pp. 164 -167, 1988.

[74] Bell, Stephanie. A beginner's guide to uncertainty of measurement. 2001.

[75] Kline, Stephen J and McClintock, FA. Describing uncertainties in single-sample experiments. *Mechanical engineering*, 75(1):3–8, 1953.